AIX-MARSEILLE UNIVERSITÉ
CHIANG MAI UNIVERSITÉ
ECOLE DOCTORALE Physique et Sciences de la Matière
FACULTÉ DES SCIENCES
LABORATOIRE D'ASTROPHYSIQUE DE MARSEILLE

Thèse présentée pour obtenir le grade universitaire de docteur

Discipline : Astronomie et Cosmologie

Anirut PHRIKSEE

Mass Estimation of Massive Galaxy Clusters using Weak Gravitational Lensing

Soutenue le 19/12/2019 devant le jury composé de :

Veronique BUAT	LAM	Présidente de Jury
Florence DURRET	IAP	Rapporteur
Jean-Paul KNEIB	EPFL	Rapporteur
Duangmanee WONGRATANAPHISAN	CMU	Examinateur
Siramas KOMONJINDA	CMU	Co-Directeur de thèse
Marceau LIMOUSIN	LAM	Directeur de thèse

Numéro national de thèse/suffixe local : 2019AIXM0544/085ED352

Résumé

Les amas de galaxies constituent les systèmes gravitationnellement liés les plus massifs de l'univers, et leur étude permet d'étudier la formation et l'évolution des grandes structures de l'Univers, ainsi que la distribution de la matière noire. Le phénomène de lentilles gravitationnelles faibles qui correspond à la déviation de la lumière par un objet massif comme un amas de galaxies permet d'estimer la distribution de masse dans les amas de galaxies.

Dans cette thèse, j'entreprend l'analyse en lentilles faibles de 279 amas de galaxies du relevé "COnstrain Dark Energy avec X-ray" (CODEX), à l'aide de données d'imagerie provenant des 4200 deg^2 du relevé DECam Legacy Survey (DECaLS). Cet échantillon est issus d'une sélection conjointe en rayons X et en richesse optique, dans un intervalle de richesse $20 \leq \lambda < 110$ et de décalage vers le rouge 0,1 $\leq$ z $\leq$ 0,2. Je sépare l'échantillon en trois intervalles de richesse, $\lambda =$ 20 - 30, 30 - 50 et 50 - 110. Je mesure l'excès de densité surfacique de masse cumulée et l'ajuste avec un profil NFW afin d'estimer la masse moyenne des amas dans chaque intervalle de richesse. De plus, j'étudie la relation d'échelle entre la masse (M_{200c}) et la richesse en supposant la relation $\langle M_{200\mathrm{c}}|\lambda\rangle \propto M_0\,(\lambda/40)^{F_\lambda}$. Je réalise un ajustement conjoint de toutes les mesures en lentille faible pour les amas individuels, et j'obtiens les valeurs de meilleur ajustement $M_0 = 3,24^{+0,29}_{-0,27} \times 10^{14}\mathrm{M}_\odot$ et $F_\lambda = 1,00^{+0.22}_{-0.22}$. Je trouve que la relation d'échelle résultante est en accord avec les estimations de masse obtenues pour les trois groupes de richesse, confirmant ainsi la validité de l'hypothèse du modèle en loi de puissance.

De plus, je compare la masse en lentille faible à la masse dynamique estimée à partir des dispersions de vitesse des galaxies membres mesurées par l'équipe SDSS-IV / SPIDERS, afin d'examiner l'hypothèse selon laquelle ces amas de galaxies sont à l'état d'équilibre dynamique. Je trouve un excellent accord entre notre relation d'échelle obtenue à partir des lentilles faibles et la relation obtenue avec les masses dynamiques, ce qui suggère que l'hypothèse d'équilibre dynamique est correcte en moyenne. De plus, ce travail confirme que l'analyse en lentille faible peut être effectuée avec les données DECaLS.

Mots clés : Astronomie, Cosmologie, Amas de galaxies, Lentilles gravitationnelles

Abstract

Galaxy clusters are the most massive gravitationally bound structures in the universe. Studying this class of objects provides important informations on the formation and evolution of the large-scale structures and on the dark matter distribution. Weak gravitational lensing, a phenomenon related to the deflection of light by a massive object like a galaxy cluster can be used to estimate the mass distribution in galaxy clusters.

In this work, I perform the weak lensing analysis of 279 galaxy clusters from the COnstrain Dark Energy with X-ray survey (CODEX), using imaging data from 4200 deg^2 of the DECam Legacy Survey (DECaLS) Data Release 3. The CODEX cluster sample is built from a joint X-ray and optical richness selection. I select clusters in the richness range $20 \leq \lambda < 110$ and in the redshift range $0.1 \leq z \leq 0.2$. I divide the cluster sample into three richness groups; $\lambda =$ 20 - 30, 30 - 50 and 50 - 110. I measure the stacked excess surface mass density and fit it with a NFW profile to extract the mean cluster mass in each group. Moreover, I study the scaling relation between the cluster mass (M_{200c}) and the richness by assuming the mass-richness relation follows $\langle M_{200c}|\lambda\rangle \propto M_0\,(\lambda/40)^{F_\lambda}$. I perform a joint fit of all the individual cluster weak lensing signal, and obtain the best-fit values, $M_0 = 3.24^{+0.29}_{-0.27} \times 10^{14}\mathrm{M}_\odot$, and $F_\lambda = 1.00^{+0.22}_{-0.22}$ for the richness scaling index. I find the resulting scaling relation to be in agreement with the mass estimates obtained for the three richness groups, thus confirming the validity of the power-law model assumption.

Furthermore, I compare the weak lensing mass with the dynamical mass estimated from cluster member velocity dispersions measured by the SDSS-IV/SPIDERS team, in order to test the assumption that galaxy clusters are, on average, in a dynamical equilibrium state. I find an excellent agreement between our weak lensing based scaling relation and the relation obtained with dynamical masses. This therefore suggests that the dynamical equilibrium assumption is correct on average. In addition, this work confirms that a weak lensing analysis can be performed with the DECaLS data.

Keywords: Astronomy, Cosmology, Galaxy clusters, Gravitational Lensing

Statement of originality

I hereby declare that the intellectual content of this thesis is the product of my own work. In this study, I perform the weak lensing analysis of the DECaLS Data Release 3 using the CODEX cluster catalog. By matching the DECaLS DR3 objects with the CFHT CS82, I can calibrate the ellipticity parameters for the DECaLS DR3 objects. This work is divided into two parts. First, the CODEX cluster catalog has been selected and separated into three groups related to the optical richness parameter in each galaxy cluster and measured the stacked excess surface mass density profile to study the weak lensing mass in each group. Another part, the scaling relation has been estimated by using the CODEX cluster sample. The result shows a good agreement between weak lensing mass and dynamical mass, which suggests that the dynamical equilibrium is suitable on average and the weak lensing analysis can be performed with the DECaLS data.

The thesis has been submitted to Chiang Mai University (Thailand) and Aix-Marseille University (France) as part of an international joint Dual Doctoral Degree. It contains no materials previously published or written by another person which have been accepted for the award of any other degree or diploma in any university or any other educational institution. Illustrations, citations, and all the assistance received in preparing this thesis have been acknowledged.

Anirut Phriksee

Acknowledgement

This thesis could not be successfully completed without fruitful supervision and contribution from many people. I would like to take this opportunity to extend my sincere gratitude and appreciation to all those who made the completion of my Ph.D. thesis possible.

First and foremost, I would like to thank my supervisors, Prof. Dr. Siramas Komonjinda and Dr. Marceau Limousin, for all supports, comments, guidance and giving me opportunities to study with double degree programs at Chiang Mai University (Thailand) and Aix-Marseille University (France). My sincere thanks also go to my co-advisors, Dr. Eric Jullo, Prof. Dr. Suwicha Wannawichian, and Dr. Utane Sawangwit, who provided me with guidance, ideas and supports during this study. They also gave me opportunities to share and discuss ideas with many people in this field as well as learn how to conduct the research, analyze the data to obtain the best possible solution, and finally publish the results.

I would like to thank all jury members, Prof. Dr. Veronique Buat, Prof. Dr. Florence Durret, Prof. Dr. Jean-Paul Kneib, Prof. Dr. Duangmanee Wongratanaphisan and Prof. Dr. Giovanni Covone, for giving me the honor to be the committees of my thesis examination, reviewing my manuscript, and also giving comments and suggestions to improve this work.

I would like to thank all staff members, students and professors at the Department of Physics and Materials Science, Chiang Mai University and Laboratory of Astrophysics of Marseille, Aix-Marseille University, for their assistances in providing facilities and materials for my Ph.D. study. Moreover, I would like to thank the Development and Promotion of Science and Technology Talents Project (DPST) and the Franco-Thai Scholarship program for their supports and funding this thesis project.

Last but not least, I would like to express my deepest gratitude to my family, Mr. Soontorn and Mrs. Somsri Phriksee, Mrs. Siriporn Sankla and Miss Sirirat Phriksee for the encouragement, kindness and supports for me after all this time.

Anirut Phriksee

Contents

List of Figures

List of Tables

1. Introduction

In this chapter, I present a brief overview of the universe and some of the observations which led to the current cosmological model. The expansion of the universe and the structure formation theory will be described in Section 1.1. In Section 1.2, I will discuss generalities about galaxy clusters, which constitute the largest gravitational bound systems in the universe. I will discuss the observational methods aimed at studying the physics of these structures, including the current and future surveys developed in order to explore the universe. In Section 1.3, I will explain the cosmological model of the universe and present the notion of distances in Cosmology. Finally, the main objectives of this thesis will be discussed in Section 3.6.

1.1. An overview of the universe

Looking at the night sky, we cannot imagine the size of the universe. There is a limitation of how far can we see the objects with the naked eyes. We can only see the light coming from the stars located in our galaxy, the Milky Way. If the night sky is clear enough, we can see nearby galaxies, like the Large and Small Magellanic Clouds. The actual size of the universe is an important question, as well as the methods aimed at measuring it. Currently, many observations and studies reveal that our universe began from the primordial singularity or “Big Bang" event, referring to the birth of the universe. The Big Bang Theory is one of many theories that describe the birth of the universe. This theory is partly validated by observations, for instance by the measured expansion of the universe. The most recent experiments estimate that the Big Bang happened about 13.8 billion years ago (see e.g., Planck Collaboration, Ade, Aghanim, et al. 2016a).

What happened right after Big Bang is still unclear due to the lack of observational data. However, within this model, the universe went through an expanding and cooling phase. About 380,000 years after the Big Bang, the temperature of the universe allowed electrons to combine with protons to form hydrogen atoms, an epoch often called the recombination epoch. This process allowed photons to travel freely and that we observe today in the Cosmic Microwave Background (CMB). In Figure 1.1, we see a map of the the CMB photons. This map shows the tiny fluctuations of CMB temperatures in order of $\delta T/T \approx 10^{-5}$, which suggests that our universe is homogeneous.

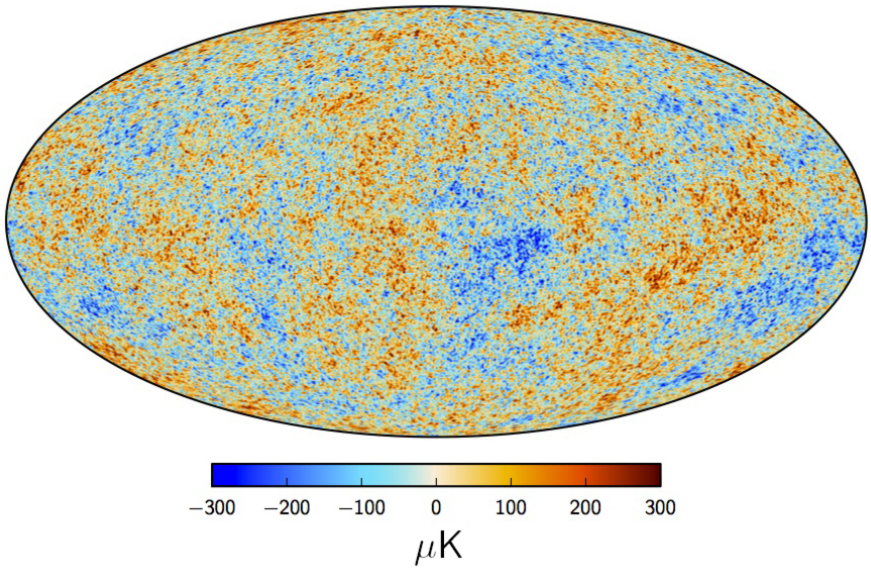

Figure 1.1. – The cosmic microwave background (CMB) intensity map at five arcmin resolution from the Planck mission. The color bar shows the CMB temperature in the unit of micro-kelvin (Credit : Mandolesi, Molinari, Gruppuso, et al. 2016).

1.1.1. The expansion of the universe

To understand the evolution of the universe, I first focus on its expansion. Lemaître 1927 published the first analysis of the expanding universe. He showed that the expansion of the universe could be measured using the spectra of distant galaxies. He derived the rate of the expansion of the universe from the velocities and photometric data of galaxies. Two years later, Hubble 1929 estimated the relationship between the distance (D) and recessional velocity of galaxies (V), which can be described by

$$V = H_0 D, \tag{1.1}$$

where H_0 is Hubble's constant. This equation is often called Hubble's law (In 2018, the IAU suggested to call it the Hubble-Lemaître's law). The index "0" refers to the Hubble constant today. The current study from the Planck mission provides the Hubble's constant to be about 67.74 ± 0.46 km Mpc^{-1} s^{-1} (Planck Collaboration, Ade, Aghanim, et al. 2016a). Moreover, the Hubble constant has the dimension of the inverse of the time. Thus, I can compute the Hubble time

(t_H) by

$$t_H \equiv \frac{1}{H_0} = \frac{1}{67.74\,\mathrm{km.s^{-1}.Mpc^{-1}}} \approx 4.57 \times 10^{17}\,s, \tag{1.2}$$

which corresponds to about 14 billion years, which might be the age of the universe if no acceleration or deceleration in the expansion is considered. In practice, we often rewrite the Hubble's constant in the form

$$H_0 = 100\,h\,\mathrm{km\ s^{-1}\,Mpc^{-1}}\,, \tag{1.3}$$

where h is the dimensionless parameter or Hubble parameter.

The universe can expand or contract depending on the compositions of the universe. For this reason, the Hubble's constant varies with time. If I assume that the universe is well described by the Friedmann-Lemaître-Robertson-Walker (FLRW) metric, therefore, the Hubble parameter can be defined by

$$H(t) = \frac{\dot{a}(t)}{a(t)}\,, \tag{1.4}$$

where $a(t)$ is called the scale factor of the universe at the considered time (t). The scale factor is also given by

$$a(t) = \frac{1}{1+z} = \frac{\lambda_{\mathrm{emit}}}{\lambda_0}, \tag{1.5}$$

where z is the redshift, λ_{emit} and λ_0 represent the wavelength of the light emitted at (t) and at the present time respectively. Note that the scale factor is set to be $a(t_0) = 1$ at the present time.

1.1.2. The chronology of the universe

After the Big Bang, atoms, molecules, stars, galaxies and the large-scale structures formed. The timeline of the universe can be roughly separated into three stages:

(1) The early universe - until about 300,000 years after the Big Bang. In this stage, particles are quickly moving and annihilating with other particles (antimatter). The temperature of the universe is adiabatically falling down until it makes possible the formation of electrically neutral atoms like hydrogen and helium. This phase is also called the photon decoupling phase; it released the free photons that we can observe today in the CMB.

(2) Star formation - From the time the light from the CMB scattered (the last scattering surface) to a few million years after the Big Bang. The universe was filled with neutral gas. The mean free path of photons is short due to the density of the neutral gas. Presently, we can not observe any information at that time

because the remaining photons are in the radio wavelength and are challenging to detect. This period is called the Dark Age Era.

Until about 500 million years after the Big Bang event, the temperature of the universe had fallen to a few hundred degrees. In that time, the universe was so hot and so dense that the gravitational effect is unable to pull these regions together. Eventually, these regions were starting to burn hydrogen gas into helium and some heavy elements. Moreover, their energy was ionizing the hydrogen atoms. It is called the reionization era.

(3) The large-scale structure formation - After about a billion years, the densest areas of the universe had collapsed. This process produced groups of stars, which formed galaxies. These galaxies continued to collide and merge with other galaxies until they form galaxy groups and galaxy clusters: the large-scale structures as we can observe today.

1.2. Galaxy cluster

Galaxy clusters, the last structures formed in the universe, are very exciting objects for astronomical and cosmological studies. First, they have a well-characterized mass function, whose structure indicates the significance of cosmological parameters. Second, numerical simulations predict the sub-halo mass function, characteristic density profiles, and triaxiality, which depend on the properties of the dark matter element, while astrophysical effects tend to mask them. Lastly, their gas to mass ratios indicate the cosmological content.

Typically, galaxy clusters consist of hundreds of galaxies; their diameters are between 1 – 5 Mpc and total masses are around 10^{14} – 10^{15} $M_{\odot}$. The composition of galaxy clusters can be separated into three main components: galaxies, intracluster medium (ICM) and dark matter. Galaxies constitute only a small fraction of the total mass, with less than 5-10% of the total mass. The ICM is a hot plasma with a temperature of 10^{7} – 10^{8} Kelvins which emits in X-ray, accounting for about 10-15% of the total mass. Therefore, the mass budget of a galaxy cluster is heavily dominated by dark matter (more than 80%), an elusive component which is sometimes called “missing mass" since we do not detect it directly. We witness this component indirectly, through its gravitational effects.

Galaxy clusters can be observed from radio to X-ray bands which tell us about the spatial distribution of their different components. In Figure 1.2, I show the comparison between the optical and X-ray images of galaxy cluster Abell 2029. The optical observation shows the light from the galaxies while the X-ray observation reveals the hot gas of the ICM.

Generally, the brightest cluster galaxy (BCG) is used to define the center of the mass distribution in galaxy clusters. The position of the cluster center can be shifted from the BCG position, for instance, if the cluster experiments a merger with another cluster. Consequently, investigations by different methods

are necessary to map the mass distribution in a galaxy cluster.

Besides, galaxy clusters appear in the CMB through the Sunyaev-Zel'dovich effect (SZE) in the radio domain (Planck Collaboration, Ade, Aghanim, et al. 2016b). This effect tells us about the cluster masses.

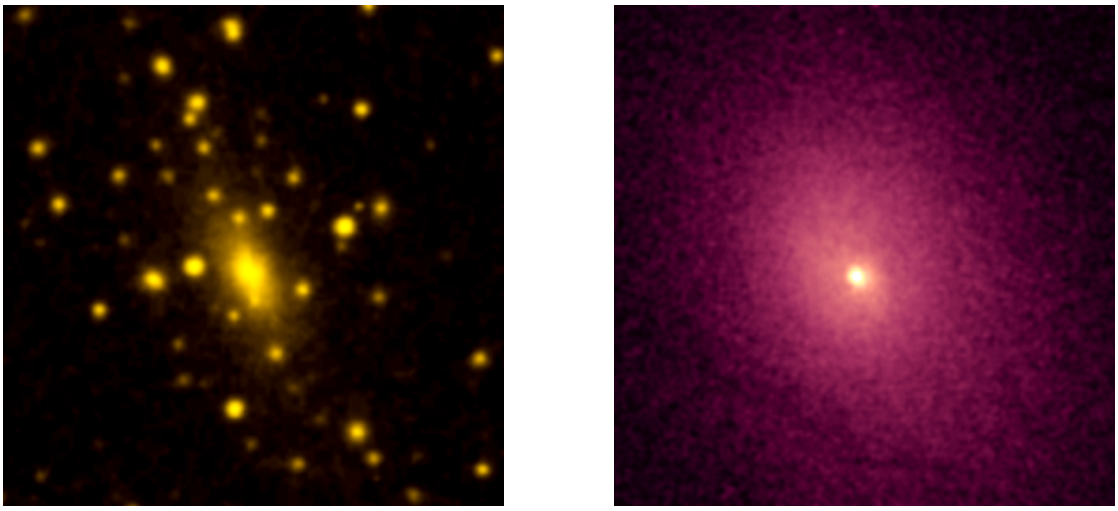

(a) Optical (b) X-ray

Figure 1.2. – Galaxy cluster Abell 2029 from optical and X-ray observation in the same scale of 4 arcmin on each side. (X-ray: NASA/CXC/UCI/A. Lewis et al., 2002, Optical: Pal.Obs. DSS)

1.2.1. X-ray observation

As described previously, galaxy clusters contain a hot plasma which has a temperature of about $10^7 - 10^8$ Kelvin heated by the gravitational field, and therefore emitting photons in the X-ray band via bremsstrahlung. The total amount of ICM is about 10 – 15% of the total mass of a cluster (Morandi, Limousin, Sayers, et al. 2012).

Galaxy clusters are important objects for X-ray astronomy because thermal processes in clusters can be observed and measured via the temperature profile and density (electron energy and density). If I assume that the ICM in galaxy clusters is in hydrostatic equilibrium and spherical symmetry and gases are in non-isothermal state, I can compute the total cluster mass by

$$M(r) = \frac{-kT_g(r)}{\mu m_p G}\left(\frac{d\ln n_e}{d\ln r} - \frac{d\ln T_g}{d\ln r}\right), \tag{1.6}$$

where k is the Boltzmann's constant, G is the Newton's gravitational constant, μ

is the mean molecular weight, m_p is the mass of the proton, T_g is the temperature distribution of gases and n_e the gas density (e.g. Rasia, Meneghetti, Martino, et al. 2012; Ettori, Donnarumma, Pointecouteau, et al. 2013). As a result, I can estimate the cluster mass via the X-ray observations.

The beginning of the study of galaxy clusters in the X-ray wavelength started in 1966 when the team from NASA's Goddard Space Flight Center used an X-ray telescope installed on a balloon to observe the X-ray emission emitted from the hot ICM of galaxy clusters: the Perseus cluster (Fritz, Davidsen, Meekins, et al. 1971) and the Coma cluster (Felten, Gould, Stein, et al. 1966). The next generation of X-ray surveys were X-ray space telescopes, for example the ROSAT-All-sky survey (RASS, 1990), the X-ray Multi-Mirror Mission (XMM-Newton, 1999) and the Chandra X-ray Observatory (1999). eROSITA, one of the new X-ray space telescopes, was recently launched in July 2019. The eROSITA telescope is estimated to be 25 times more sensitive than the ROSAT telescope. The scientific goals of this survey are to study the ICM, map the large-scale structures, observe black holes and active galactic nuclei (AGN), and detect X-ray astronomical sources.

1.2.2. Optical observation

There are many motivations to study galaxy clusters in the visible band. The principal objectives are to study the number density of galaxies, their luminosity distribution and velocity dispersion profiles. The color-magnitude relation of cluster galaxies is one method to study the evolution of galaxy populations in clusters. This relation displays a characteristic feature, that we can use in cluster finding algorithms, for instance the red-sequence Matched-filter Probabilistic Percolation (Rykoff, Rozo, Busha, et al. 2014).

Moreover, optical observations are used to infer gravitational lensing effect. Massive objects like galaxy clusters do locally bend space time, so that the light coming from distant background objects is distorted. Observing the deviation of light can be used to infer the mass of galaxy clusters. I will discuss this in Section 2.5.

The first study of galaxy clusters in optical began in 1958 when Abell and his collaborators observed galaxy clusters and built a cluster catalog. They reported 2712 galaxy clusters in the Northern hemisphere and then they extended their work to the Southern hemisphere, reaching 4073 clusters in the final catalog (George O. Abell 1958; G. O. Abell, Corwin, and Olowin 1989). Abell's catalog is frequently used to study the physical properties and evolution of galaxy clusters.

The two-degree-Field Galaxy Redshift Survey (2dFGRS), a spectroscopic survey aiming at measuring galaxy redshifts, is a more recent survey that used the 3.9m Anglo-Australian Telescope at the Anglo-Australian Observatory, and was conducted in the period 1997 - 2002. The 2dFGRS collected spectra of 245591 objects covering approximately 1500 square degrees. This survey also provided

the new prospective details of the distribution of nearby galaxies. Figure 1.3 shows the 2dFGRS data up to redshift ≈ 0.2. We can observe the large scale structures of the universe, in particular the “Sloan Great Wall".

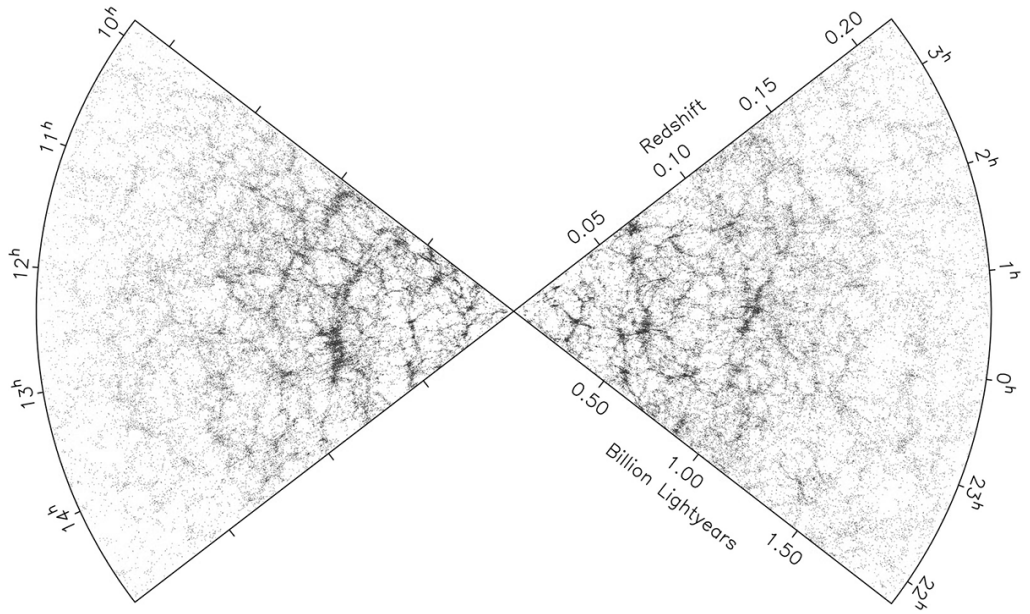

Figure 1.3. – The distribution of the nearby galaxies from the 2dFGRS data (Credits: 2dfGRS team).

1.3. Cosmological Framework

In this section, the structure of the universe will be described by using the Friedmann Lemaître Robertson Walker (FLRW) metric, which is the exact solution of Einstein’s general theory of relativity.

1.3.1. Einstein’s field equations

In early time - before the twentieth century, physics framework was based on Newtonian gravity, also called the classical mechanics, which describes how the gravitational force acts on an object. In 1915, Einstein published the theory of General Relativity that blends gravity into his previous work on special relativity. This theory redefines the physics framework of gravitational fields. He changed the object’s mass definition from its form in classical mechanics to a more general form, described by an energy-momentum tensor. He also defined the famous

Einstein's field equations

$$G_{\mu\nu} \equiv R_{\mu\nu} - \frac{1}{2}Rg_{\mu\nu} = \frac{8\pi G}{c^4}T_{\mu\nu}\,, \tag{1.7}$$

where $G_{\mu\nu}$ is the Einstein tensor, $R_{\mu\nu}$ is the Ricci curvature tensor, $g_{\mu\nu}$ is the metric tensor, $T_{\mu\nu}$ is the energy–momentum tensor or stress–energy tensor, that describes the density of energy and momentum in spacetime. R is the scalar curvature, G is the gravitational constant and c is the speed of light. Equation 1.7 consists of ten equations, that describe the gravitational field in terms of an equivalence between spacetime curvature, mass and energy at the specific point. In addition, the trajectory of the particles, i.e. the world line in the general relativity framework, can be accurately computed by using the geodesic equation.

1.3.2. The model of the universe

There are many models to describe the evolution, dynamics and physical properties of the universe. Presently, the Lambda-Cold Dark Matter cosmological model (ΛCDM), which is also called the standard cosmological model, is one of the most accurate models to describe our universe. This model consists of two main components; Lambda and cold dark matter. The cosmological constant (Λ) is related to the energy of the universe or dark energy that explains the accelerated expansion of the universe. The cold dark matter is the missing matter that one needs to account for in order to explain the observational data. The ΛCDM model is commonly used to describe the universe because it describes the existence and evolution of the large scale structure, and the accelerating expansion of the universe very well.

However, the cold dark matter framework is currently the preferred hypothesis to explain the observations which we have yet to detect dark matter particles directly. It is also encountering problems in describing structures especially at small scales (Del Popolo and Le Delliou 2017). Alternative models have been extensively studied to challenge the assumptions of the ΛCDM model, for instance, modified gravity e.g. $f(R)$ theories; De Felice and Tsujikawa 2010.

The fundamental principle behind the ΛCDM model is the cosmological principle, i.e. that the universe is isotropic and homogeneous on large scales. Isotropic means that the observer can detect the same properties of the universe in every direction. Therefore, homogeneous and isotropic properties are defined such that the universe looks similar in every place and direction from the observer point of view. It can not be true in our universe unless we consider at the large scale of the universe, for example, beyond 100 Mpc.

To describe the ΛCDM model, Einstein's field equation as shown in Equation 1.7 is first considered. In 1917 - two years after Einstein published the General Relativity, Einstein introduced the concept of the static universe by including the cosmological constant (Λ) which appears in the geometric part of the General

Relativity equation

$$R_{\mu\nu} - \frac{1}{2}Rg_{\mu\nu} + \Lambda g_{\mu\nu} = \frac{8\pi G}{c^4}T_{\mu\nu}\,. \tag{1.8}$$

However, after Hubble-Lemaître discovered that the universe was expanding, Einstein abandoned the static universe idea and proposed a new model, the Einstein-de Sitter universe, in which the cosmological constant is set to zero.

Between the 1920s - 1940s, four scientists - Friedmann, Lemaître, Robertson and Walker - derived and developed an exact solution of the Einstein's field equations to describe the physical properties and dynamics of the universe. To express this model, I start from the fundamental concept of General Relativity. The distance between two points in spherical coordinates can be written by

$$(dl)^2 = \left(\frac{dr}{\sqrt{1-Kr^2}}\right)^2 + (rd\theta)^2 + (r\sin\theta\, d\phi)^2. \tag{1.9}$$

where K is denoted the curvature space. Therefore, the distance of the world line between two events in comoving coordinates can be written by

$$(ds)^2 = (cdt)^2 - a^2(t)\left[\frac{dr^2}{1-kr^2} + r^2(d\theta + \sin^2\theta\, d\phi^2)\right], \tag{1.10}$$

where r is the radius in the comoving distance, $k = a^2(t)K$, and $a(t)$ is the scale factor. Equation 1.10 is called the Friedmann-Lemaître-Robertson-Walker (FLRW) metric. In addition, the curvature parameter (k) is referred to the geometry of the space which can be one of the following cases;

(1) Flat space or Euclidean space ($k = 0$), the summation of triangle's angles equals to 180°,

(2) Spherical geometry ($k = +1$), the summation of triangle's angles is more than 180°,

(3) Hyperbolic geometry ($k = -1$), the summation of triangle's angles is less than 180°.

Figure 1.4 shows the 2D illustration of the curvature of the space as red solid lines.

1.3.3. Cosmological parameters

If I assume that the universe is homogeneous and isotropic, we can use the Friedmann–Lemaître–Robertson–Walker (FLRW) metric to find an exact solution of Einstein's field equation. The energy-momentum tensor can be written in the form of an ideal fluid in thermodynamics equilibrium as

$$T_{\mu\nu} = \left(\rho + \frac{p}{c^2}\right) u_\mu u_\nu + p g_{\mu\nu}\,, \tag{1.11}$$

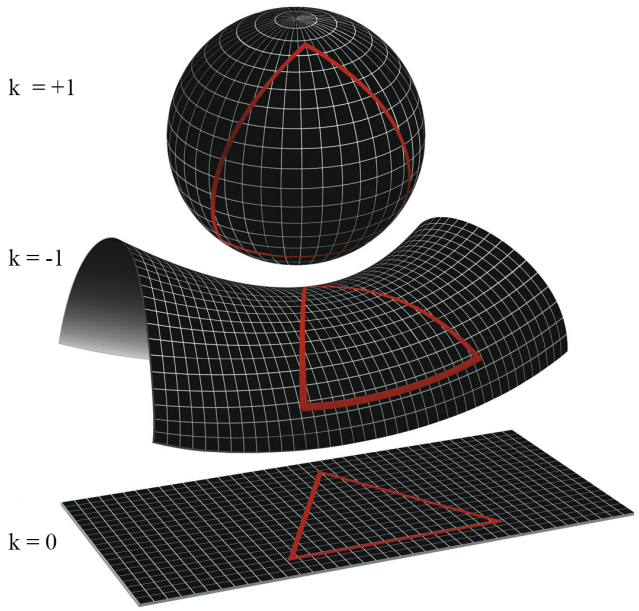

Figure 1.4. – An illustration of the curvature space (Credits: NASA / WMAP Science Team).

where ρ is the matter density, p is the pressure density, u_μ is the fluid's velocity, and $g_{\mu\nu}$ is the metric tensor. By substituting Equation 1.11 into Einstein's field equations, we can derive the relation of mass and scale of the universe as

$$H^2 = \left(\frac{\dot{a}}{a}\right)^2 = \frac{\Lambda c^2}{3} - \frac{kc^2}{a^2} + \frac{8\pi G\rho}{3}\,, \tag{1.12}$$

where H is the Hubble parameter, a is the scale factor and $\dot{a}$ is the temporal derivative of the scale factor that represents the change of the size of the universe. If we assume that the universe is flat and the cosmological constant equals to zero ($\Lambda = 0$), we can compute the critical density of the universe as

$$\rho_c(t) = \frac{3H^2(t)}{8\pi G}\,. \tag{1.13}$$

For instance, at the present time (t = 0), the critical density of the universe is

$$\rho_{c,0} = \frac{3H_0^2}{8\pi G} \approx \frac{3 \times (67.74\,\text{km/Mpc/s})^2}{8\pi \times (6.67 \times 10^{-11}\,\text{m}^3\,\text{kg}^{-1}\,\text{s}^{-2})} \approx 8.6 \times 10^{-27}\frac{\text{kg}}{\text{m}^3}\,, \tag{1.14}$$

or about 5 hydrogen atoms per cubic meter.

In the literature, we commonly use the dimensionless density parameter or cosmological parameter (Ω), defined by the ratio of each component to the critical

density of the universe as

$$\Omega_i \equiv \frac{\rho_i}{\rho_c} = \left(\frac{8\pi G}{3H^2}\right)\rho_i \,. \tag{1.15}$$

Moreover, it is useful to define the curvature energy density as

$$\rho_K \equiv -\frac{3}{8\pi G}\frac{kc^2}{a^2} \,. \tag{1.16}$$

By multiplying the Friedmann equation with (1 / H_0^2), I can rewrite the Friedmann equation at the present time as

$$1 = \frac{\Lambda c^2}{3H_0^2} - \frac{kc^2}{a^2H_0^2} + \frac{8\pi G\rho}{3H_0^2} = \Omega_\Lambda + \Omega_K + \Omega_M \,, \tag{1.17}$$

where $\Omega_\Lambda \equiv \Lambda c^2/3H_0^2$ is the cosmological constant (or Dark Energy density), $\Omega_K \equiv kc^2/a^2H_0^2$ is the spatial curvature density and $\Omega_M \equiv 8\pi G\rho/3H_0^2$. In addition, the density is also related to the scale factor which can be computed by the mass density $\rho_M \propto a^{-3}$, and the dark energy $\rho_\Lambda \propto a^{-3(1+w)}$. It should be noted that another term was dominating during the early ages of the universe, the radiation energy density $\rho_{rad} \propto a^{-4}$. For the simplify in these expressions and the small effect of the radiation energy today, I excluded it from the calculations.

Substituting the cosmological parameters into Equation 1.12, the Hubble parameter expression becomes

$$H^2(z) = H_0^2[\Omega_\Lambda + \Omega_K(1+z)^2 + \Omega_M(1+z)^3] \,. \tag{1.18}$$

Frequently and for convenience, I define the function $E(z)$ as

$$E(z) = \sqrt{\Omega_\Lambda + \Omega_K(1+z)^2 + \Omega_M(1+z)^3} \,. \tag{1.19}$$

Inserting E(z) into Friedmann's equation, I can find the ratio as

$$H(z) = \frac{\dot{a}(t)}{a(t)} = H_0E(z) \,. \tag{1.20}$$

1.4. Distance in Cosmology

To measure the distance in the universe, we must understand how the distances are defined in our cosmological framework. In this work, I use the comoving coordinates to measure the distances to the objects. It is different from the usual approach in weak gravitational lensing analysis, where distances are expressed in terms of angular diameter distances (e.g. Hogg 1999).

1.4.1. Comoving distance

If I measure two objects in the universe, I will find that these objects are moving with the Hubble flow, in other words, the expansion of the universe. To keep the distance between them “static", i.e. it does not change with time, I therefore divide the physical distance between these two points by the scale factor of the universe. Considering the Hubble distance D_H defined by

$$D_H \equiv \frac{c}{H_0}\,, \tag{1.21}$$

the radial comoving distance (D_C) along the line of sight is obtained by integrating the distance along the line of sight from the present ($z = 0$) to the objects redshift (z),

$$D_C = D_H \int_0^z \frac{dz'}{E(z')}. \tag{1.22}$$

Moreover, if I observe two events at the same redshift separated by an angle $\delta\theta$, I can compute the separated distance equals to $\delta\theta D_M$, where D_M is the transverse comoving distance. The transverse comoving distance also depends on the curvature of the spacetime. Its expression is

$$D_M = \begin{cases} \frac{D_H}{\sqrt{\Omega_K}} \sinh(D_C\sqrt{\Omega_K}/D_H) & (\Omega_K > 1)\,, \\ D_C & (\Omega_K = 1)\,, \\ \frac{D_H}{\sqrt{|\Omega_K|}} \sin(D_C\sqrt{|\Omega_K|}/D_H) & (\Omega_K < 1)\,. \end{cases} \tag{1.23}$$

1.4.2. Angular diameter distance

The angular diameter distance (D_A) is often used in gravitational lensing studies. It is related to the transverse distance D_M, that corresponds to an angular size (in unit of radians). The angular diameter distance at the redshift z can be written in corresponding to the transverse comoving distance as

$$D_A = \frac{D_M}{1+z}\,. \tag{1.24}$$

Note that we can compute the angular diameter distance between two redshifts in the case ($\Omega_K \geq 0$) by

$$D_A(z_1, z_2) = \frac{1}{1+z_2}\left[D_{M,z_2}\sqrt{1+\Omega_K\frac{D_{M,z_1}^2}{D_H^2}} - D_{M,z_1}\sqrt{1+\Omega_K\frac{D_{M,z_2}^2}{D_H^2}}\right]\,. \tag{1.25}$$

In addition, the luminosity distance ($D_{\rm L}$) is defined from the flux S and the luminosity L of an object, such that

$$D_{\rm L} \equiv \sqrt{\frac{L}{4\pi S}} \,. \tag{1.26}$$

We can use the Etherington's equation to find the relationship between the luminosity distance and the angular diameter distance (Etherington 1933), which is given by

$$D_{\rm L} = (1+z)^2 D_{\rm A} \,. \tag{1.27}$$

Figure 1.5 shows the comparisons between the luminosity, comoving and angular diameter distance as a function of redshift.

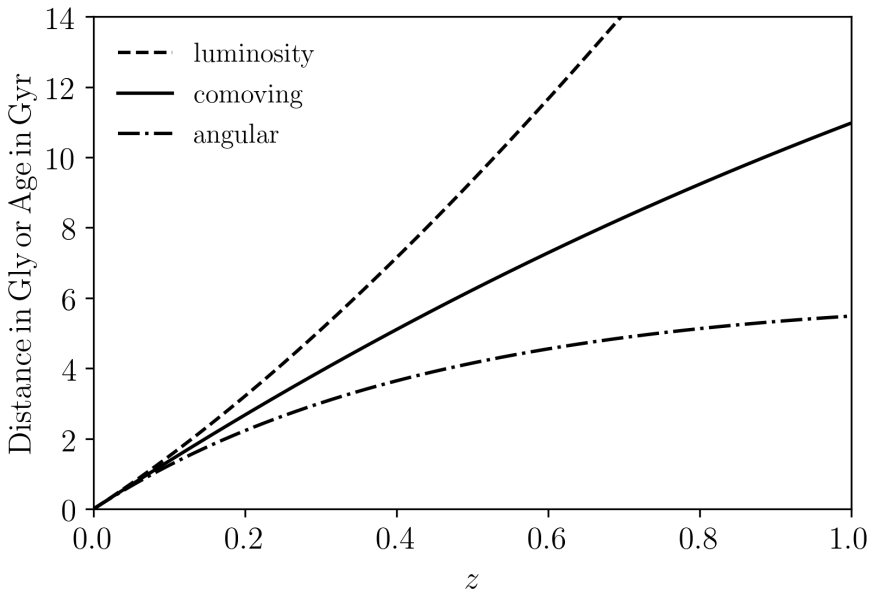

Figure 1.5. – A comparison of cosmological distances, assuming the flat ΛCDM model with the cosmological parameters; $\Omega_{\rm M} = 0.27$ and $\Omega_{\Lambda} = 0.73$.

2. Gravitational Lensing

In this chapter, I will first introduce the history of gravitational lensing. Then I will review the basics of gravitational lensing. Finally, I will focuss on weak gravitational lensing by galaxy clusters.

2.1. A brief history of gravitational lensing

Gravitational lensing is the phenomenon that occurs when background light is deflected by massive foreground objects. Gravitational lensing started in the early eighteenth century. In that time, the physical framework was based on classical Newtonian mechanics. Soldner, a German physicist, mathematician, and astronomer, published a paper in 1804 about the estimation of the deflection angle due to lensing of a star by the sun (Soldner 1804). He estimated the deflection angle to be

$$\hat{\alpha} = \frac{2Gm}{v^2 r} \approx \frac{2 \times (6.67 \times 10^{-11} \mathrm{m}^3.\mathrm{kg}^{-1}.\mathrm{s}^{-2}) \times (2 \times 10^{30} \mathrm{kg})}{(3 \times 10^8\,\mathrm{m/s})^2 (7 \times 10^8\,\mathrm{m})} \approx 0.87" \,. \tag{2.1}$$

This estimation was not confirmed because of the limitation of the instruments available at that time. In 1911, Einstein used the equivalence method to estimate the deflection angle as did Johann Soldner and he found the same result. In 1915, Einstein recomputed this estimation using the General Relativity, finding

$$\hat{\alpha} = \frac{4Gm}{c^2 r} \approx 1.75" \,, \tag{2.2}$$

which is twice the result from Soldner. This estimation and the theory was confirmed with an observation by Arthur Eddington and his team in 1919, during the solar eclipse (Dyson, Eddington, and Davidson 1920).

Zwicky 1937 studied that the deflection of light by galaxies and proposed that this phenomenon can be used to test for the general theory of gravity. He also mentioned that the gravitational lensing would allow us to observe the undetected distant galaxies via the magnification effect of the gravitational lensing.

In 1979, the first gravitational lensing system, the double image of the quasar QSO 0957+561, was discovered by Weymann, Chaffee, Carleton, et al. 1979. The fact that these two images were coming from the same source was confirmed by the similar spectra of each image and by the analysis of the flux ratio in optical

and radio bands.

An arc like feature was first discovered in galaxy clusters CL 2244-02 (Lynds and Petrosian 1986) and Abell 370 (Soucail, Mellier, Fort, et al. 1988). Spectroscopic observations showed that the redshift of this arc was larger than the redshift of the cluster, confirming the gravitational lensing hypothesis . Figure 2.1 shows an image of galaxy cluster Abell 370, featuring gravitationally lensed images, in particular the historical giant arc.

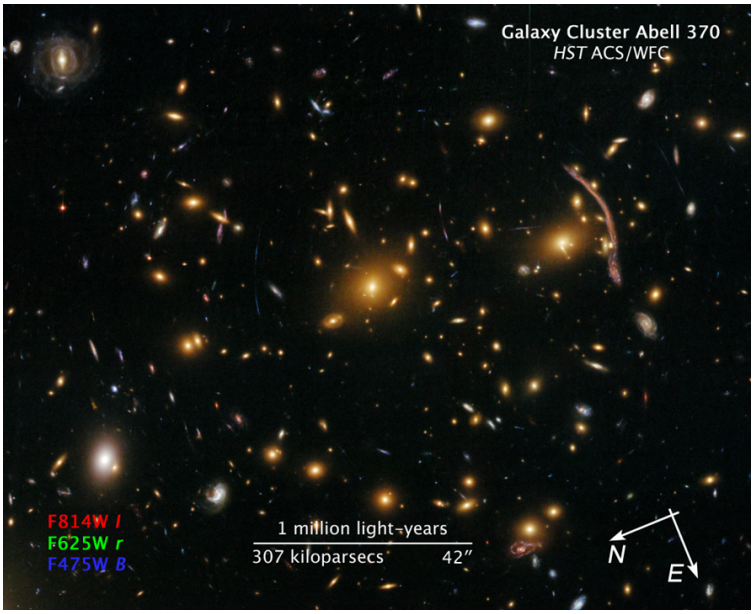

Figure 2.1. – Galaxy Cluster Abell 370, located at redshift z = 0.375 or approximately 6 billion light years from Earth. This image combines visible and near-infrared data from Hubble's Advanced Camera for Surveys (ACS). (Credit: NASA, ESA, J. Lotz and the HFF Team (STScI))

2.2. Simple lens model

In the previous chapter, I have presented the definition of space-time from General Relativity. Space-time around massive objects is curved, therefore the light from distant objects passing close to massive objects is deflected.

Figure 2.2 illustrates the curvature of space-time and the bending of the light coming from distant objects. There are two main regimes of gravitational lensing. In the non linear strong lensing regime, when the light travels through the cluster core where the mass density is very high (larger than the critical density), one can observe multiple images of the same background source as well as giant arcs. When the light pass outside the cluster core, one can be sensitive, statistically, to

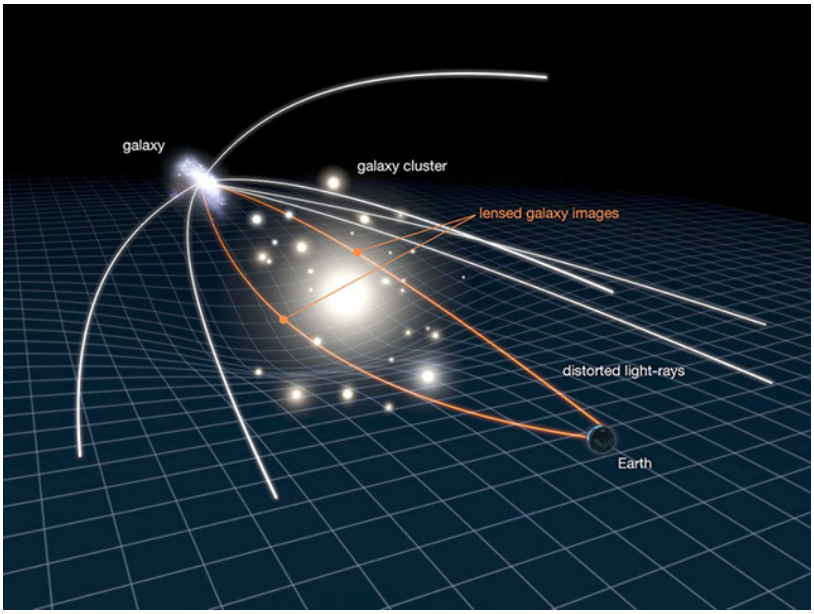

Figure 2.2. – Illustration of gravitational lensing phenomena by a galaxy cluster. The light rays coming from distant galaxies and traveling close to galaxy clusters are deflected. This effect distorts the light path and creates, for instance, multiple images, as well as elongation and magnification of the distant galaxy. (Credit: NASA/ESA)

weak distortions in the shape of the background galaxies. This is the linear weak lensing regime. In both cases, these observations provide informations about the mass distribution of the deflector.

To derive the basics of gravitational lensing, we first assume that the universe can be described by the Friedmann-Lemaitre-Robertson-Walker metric. I consider the case of the metric of spacetime, which is weakly perturbed by the Newtonian gravitational potential ($|\Phi| \ll c^2$). The line element can be written as

$$ds^2 = g_{\mu\nu} dx^\mu dx^\nu = c^2 dt^2 - d^2\vec{x}\,. \tag{2.3}$$

Therefore, the perturbed spacetime metric is given by

$$ds^2 = \left(1 + \frac{2\Phi}{c^2}\right) c^2 dt^2 - \left(1 - \frac{2\Phi}{c^2}\right) d^2\vec{x}\,. \tag{2.4}$$

2.2.1. Deflection angle

As illustrated in Figure 2.4, let's consider a light ray traveling close to a lens of mass M. It is deflected by an angle $\hat{\alpha}$. I can write the Newtonian potential of the

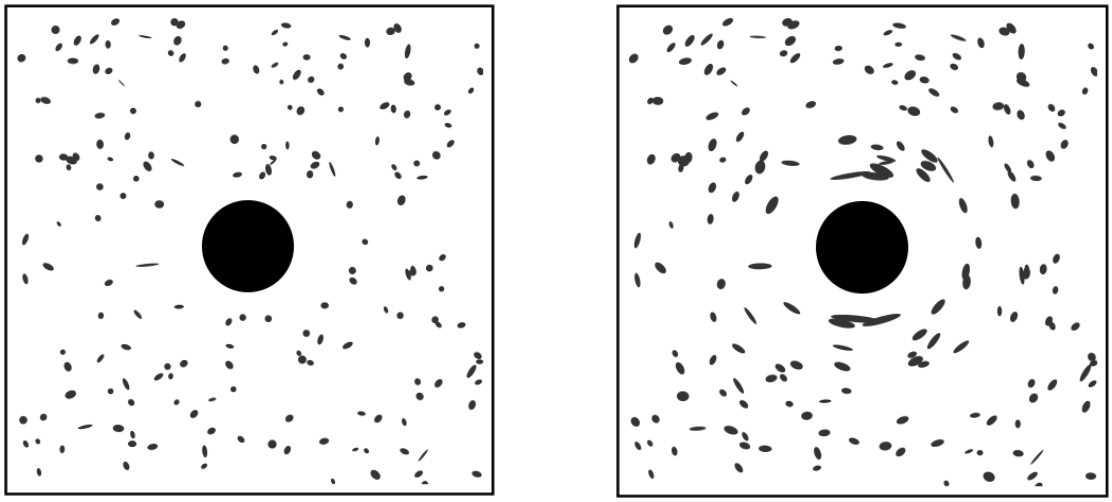

(a) unlensed (b) lensed

Figure 2.3. – Simulation of the gravitational lensing phenomena: (a) Unlensed images: the distant galaxies are randomly distributed in the field with an intrinsic shape. A deflector is located in the centre of the field. (b) Lensed images: we can appreciate how the shape of the galaxies has been gravitationnally distorted. (Credit: TallJimbo 2008/Wikimedia Commons.)

lens as

$$\Phi = -\frac{GM}{(b^2 + z^2)^{1/2}}\,; \tag{2.5}$$

where b is the impact parameter and z is the unperturbed light path. The gradient of the potential perpendicular to the light path is given by

$$\vec{\nabla}_\perp \Phi = \frac{GM\vec{b}}{(b^2 + z^2)^{3/2}}\,. \tag{2.6}$$

The deflected angle of the light path by the mass (M) is given by

$$\vec{\hat{\alpha}} = \frac{2}{c^2}\int \vec{\nabla}_\perp \Phi \, \mathrm{d}\lambda\,, \tag{2.7}$$

where λ is a curvature parameter related to the light path. Substituting Equation 2.6 into Equation 2.7, the deflection angle becomes

$$\vec{\hat{\alpha}}(b) = \frac{4GM}{c^2 b}\,. \tag{2.8}$$

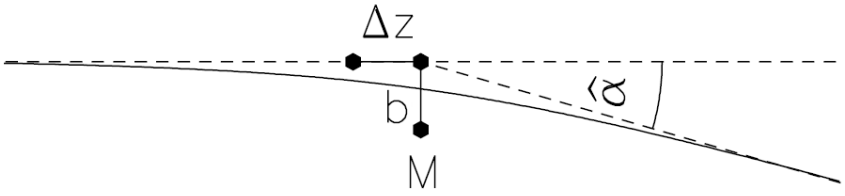

Figure 2.4. – Illustration of the deflection of a light ray by a point mass (M). The light (solid line) travels from left to right and is deflected with an angle α (Credit: Narayan 1995).

2.2.2. Thin gravitational lenses

Let's consider the optical configuration given in Figure 2.5. The observer (O) will detect the image (I) of the source (S) with a deflection angle equal to $\vec{\alpha}$. The lens is considered to be "thin", i.e. the lens thickness is small compared to the distances involved in the optical configuration.

The distances between the observer and the source, the observer and the lens, and the lens and source are called D_L, D_S and D_{LS} respectively. The position angles of the source and the image are called $\vec{\beta}$ and $\vec{\theta}$ respectively. It is noted that an addition of the distance, $D_S \neq D_L + D_{LS}$, if the spacetime is curved ($k \neq 0$).

Assuming that the angles $\hat{\alpha}$, β and θ are small, I derive

$$\vec{\theta} D_S = \vec{\beta} D_S + \vec{\hat{\alpha}} D_{LS} \,. \tag{2.9}$$

It is convenient to define the reduced deflection angle

$$\vec{\alpha} \equiv \frac{D_{LS}}{D_S} \vec{\hat{\alpha}}(\vec{\theta}) \,. \tag{2.10}$$

Substituting the reduced deflection angle into Equation 2.9 and rearranging it, I can write the lens equation as

$$\vec{\beta} = \vec{\theta} - \vec{\alpha}(\vec{\theta}) \,. \tag{2.11}$$

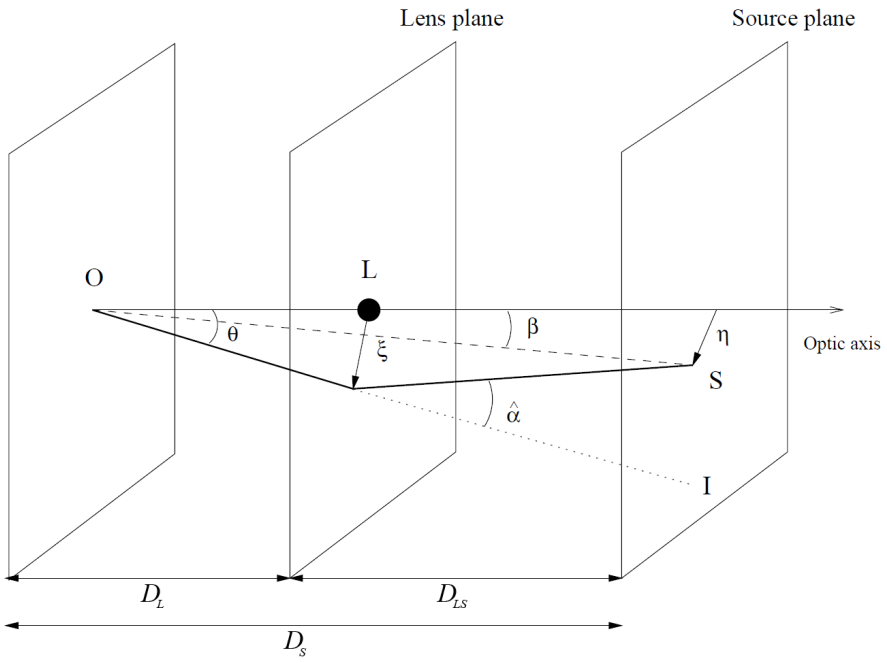

Figure 2.5. – Diagram of a thin gravitational lens. (Credit: Keiichi Umetsu 2010)

2.3. Gravitational lensing potential

The effective gravitational lensing potential (Ψ) can be computed by projecting the 3D Newtonian gravitational potential on the lens plane along the optical axis (z):

$$\Psi(\vec{\theta}) = \frac{2}{c^2}\frac{D_{LS}}{D_L D_S}\int \vec{\nabla}_\perp \Phi(D_L\vec{\theta}, z)\,\mathrm{d}z\,. \tag{2.12}$$

The deflection angle can be calculated from the gradient of the effective gravitational lensing potential as

$$\begin{aligned}\vec{\nabla}_\theta\Psi &= \frac{D_{LS}}{D_S}\left[\frac{2}{c^2}\int \vec{\nabla}_\perp\Phi\, dz\right]\,,\\ &= \frac{D_{LS}}{D_S}\vec{\hat{\alpha}}\,,\\ \vec{\nabla}_\theta\Psi &= \vec{\alpha}\,.\end{aligned} \tag{2.13}$$

Moreover, the Laplacian of the effective gravitational lensing potential is related to the surface mass density by

$$\begin{aligned}\nabla^2_\theta \Psi &= \frac{2}{c^2}\frac{D_L D_{LS}}{D_S}\int \nabla^2_\xi \Phi \, dz \,, \\ &= \frac{2}{c^2}\frac{D_L D_{LS}}{D_S} 4\pi G \Sigma(\vec{\theta}) \,, \\ &= 2\frac{\Sigma(\vec{\theta})}{\Sigma_c} \,, \\ \nabla^2_\theta \Psi &\equiv 2\kappa(\vec{\theta}) \,.\end{aligned} \tag{2.14}$$

where Σ_c is called the critical surface density given by

$$\Sigma_c = \frac{c^2}{4\pi G}\frac{D_S}{D_L D_{LS}} \,, \tag{2.15}$$

and κ is called the convergence defined by

$$\kappa(\vec{\theta}) = \frac{\Sigma(\vec{\theta})}{\Sigma_c} \,. \tag{2.16}$$

2.4. Lens mapping

A gravitational lens defines a transformation between a source plane and an image plane. The Jacobian (A) of this transformation is

$$A = \frac{\partial \vec{\beta}}{\partial \vec{\theta}} = \left(\delta_{ij} - \frac{\partial \alpha_i(\vec{\theta})}{\partial \theta_j}\right) = \left(\delta_{ij} - \frac{\partial^2 \Psi(\vec{\theta})}{\partial \theta_i \partial \theta_j}\right) \,. \tag{2.17}$$

where θ_i and θ_j are the components of the vector $\vec{\theta}$ on the lens plane. The second derivative of the gravitational lensing potential can be expressed by

$$\frac{\partial^2 \Psi(\vec{\theta})}{\partial \theta_i \partial \theta_j} = \Psi_{ij} \tag{2.18}$$

Substituting Equation 2.18 into the Laplacian of the gravitational lensing potential, I can find the convergence as

$$\kappa = \frac{1}{2}(\Psi_{11} + \Psi 22) \,. \tag{2.19}$$

The shear tensor is related to the gravitational lensing potential as

$$\gamma_1(\vec{\theta}) = \frac{1}{2}(\Psi_{11} - \Psi_{22}), \tag{2.20}$$

$$\gamma_2(\vec{\theta}) = \Psi_{12} = \Psi_{21}. \tag{2.21}$$

Therefore, by inserting the convergence and shear tensor into the Jacobian matrix, the Jacobian metric becomes

$$A = \begin{pmatrix} 1-\kappa-\gamma_1 & -\gamma_2 \\ -\gamma_2 & 1-\kappa+\gamma_2 \end{pmatrix}. \tag{2.22}$$

Rearranging the equation, I have

$$A = (1-\kappa)\begin{pmatrix} 1 & 0 \\ 0 & 1 \end{pmatrix} - \gamma \begin{pmatrix} \cos 2\phi & \sin 2\phi \\ \sin 2\phi & -\cos 2\phi \end{pmatrix}. \tag{2.23}$$

Figure 2.6 illustrates how a circular source is transformed by the convergence and the shear. The semi-major and minor axes of the elliptical image are given by

$$a = \frac{1}{1-\kappa-\gamma}, b = \frac{1}{1-\kappa+\gamma}. \tag{2.24}$$

Another important factor for the gravitational lensing phenomena is the image magnification. The magnification (μ) can be computed from the amplification matrix:

$$\mu \equiv \frac{1}{\det A} = \frac{1}{(1-\kappa)^2 - |\gamma|^2} \tag{2.25}$$

2.5. Weak gravitational lensing by galaxy clusters

In this section, I describe weak gravitational lensing generated by a galaxy cluster. The strength of the effect depends on the lens' mass distribution, the distances involved in the problem, and the alignment between the lens and the source. In the weak gravitational lensing analysis, we approximate the shape of a galaxy as an ellipse. This ellipticity can be expressed as

$$\gamma = \gamma_1 + i\gamma_2 = \frac{a-b}{a+b} e^{2i\phi} \tag{2.26}$$

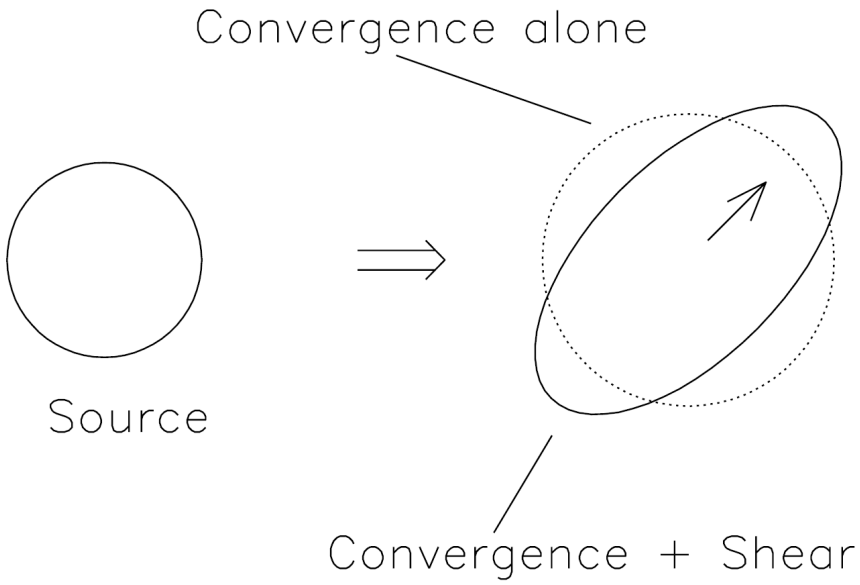

Figure 2.6. – Illustration of the effect of shear and convergence on a circular source. (Credit: Narayan and Bartelmann 1996)

where ϕ is the position angle, a and b are the semi-major and minor axes respectively. In practice, it is convenient to define the reduced shear (g):

$$g(\vec{\theta}) \equiv \frac{\gamma(\vec{\theta})}{1-\kappa(\vec{\theta})}\,. \tag{2.27}$$

The ellipticity of the lensed image (ϵ_I) is related to the ellipticity of the source (ϵ_S) by

$$\epsilon_I = \begin{cases} \frac{\epsilon_S+g}{1+g^*\epsilon_S} & \text{if } |g| \geq 1\,, \\ \frac{1+g\epsilon_S^*}{\epsilon_S^*+g^*} & \text{if } |g| < 1\,. \end{cases} \tag{2.28}$$

In the weak lensing regime, $\kappa \ll 1$ and $|g| \ll 1$, so that the relation between the ellipticities is given by

$$\epsilon_I \approx \epsilon_S + g \approx \epsilon_S + \gamma\,. \tag{2.29}$$

Assuming that the background galaxies are randomly distributed in shape, by averaging the above relation over many galaxies, we have ($\epsilon_S \approx 0$). Therefore the lensed ellipticities become

$$\epsilon_I \approx \gamma\,. \tag{2.30}$$

The shear or weak lensing signal is thus directly related to the mean ellipticity of the images.

The shear can be separated into two components: the tangential shear (γ_t) and cross shear ($\gamma_\times$). These quantities are defined by

$$\gamma_t = -\mathbf{Re}[\gamma e^{-2i\phi}] \text{ and } \gamma_\times = -\mathbf{Im}[\gamma e^{-2i\phi}]\,, \tag{2.31}$$

where ϕ is the position angle. where ϕ is an Using Equation 2.26, we can derive:

$$\gamma_t = -[\gamma_1 \cos(2\phi) + \gamma_2 \sin(2\phi)]\ , \gamma_\times = -\gamma_1 \sin(2\phi) + \gamma_2 \cos(2\phi)\,. \tag{2.32}$$

2.6. Mass profiles

Many mass models have been developped in order to describe the mass distribution in galaxy clusters, for example the Singular Isothermal Sphere (SIS), the Einasto (Merritt, Graham, Moore, et al. 2006) or the Navarro-Frenk-White profile (Navarro, Frenk, and White 1997). In this work, I use the Navarro-Frenk-White profile (hereafter NFW profile) which is widely used to describe mass distributions of galaxy clusters.

The total mass distribution will be described as follow:

$$\Delta\Sigma(R) = (1 - f_{\rm mis})\Delta\Sigma_{\rm 1h}^{\rm NFW}(R) + f_{\rm mis}\Delta\Sigma_{\rm mis}^{\rm NFW}(R) + \Delta\Sigma_{\rm 2h}(R)\,, \tag{2.33}$$

where $\Delta\Sigma_{\rm 1h}^{\rm NFW}$ is the excess surface mass density of the NFW profile, $\Delta\Sigma_{\rm mis}^{\rm NFW}$ is the miscentering profile, $\Delta\Sigma_{\rm 2h}$ is the excess surface mass profile of the second dark matter halo and $f_{\rm mis}$ is the miscentering factor. Figure 2.7 illustrates these different components that I will define below.

2.6.1. Navarro-Frenk-White profile

Numerical simulation is an important tool to probe the formation and evolution of the large-scale structures. Navarro, Frenk, and White 1997 (used N-body simulations in the cold dark matter framework to investigate the density profile of dark matter halos. They found that halos can be well described by an “universal" profile over several orders of magnitudes in mass, in particular at the galaxy cluster scale. The 3D mass density profile is given by:

$$\rho(r) = \frac{\delta_c \rho_c}{(r/r_s)(1 + r/r_s)^2}\,, \tag{2.34}$$

where r is the distance from the cluster center in three dimensions, r_s is the scale radius, and δ_c is the linear overdensity limit at which the halo collapses and is

defined as

$$\delta_c = \frac{200}{3} \frac{c^3}{[\ln(1+c) - c/(1+c)]} \,. \tag{2.35}$$

We usually define a dimensionless parameter called the concentration parameter, $c \equiv r_{200}/r_s$, where r_{200} is the radius inside which the mass density of the halo is equal to 200 times the critical density of the Universe, which can be written as

$$\rho_c = \frac{3}{800\pi} \frac{M_{200}}{r_{200}^3}, \tag{2.36}$$

where M_{200} is the cluster mass computed within this radius.

The surface mass density of the NFW profile is obtained by integrating the density profile along the line-of-sight (z),

$$\Sigma(R) = 2 \int_0^\infty \rho(R, z) d\mathrm{z} \,, \tag{2.37}$$

where R is the radius projected on the lens plane. In this case, I assume that galaxy cluster is spherically symmetric. Therefore the tangential shear experienced by background sources at redshift z_s by the cluster at redshift z_l is given by

$$\gamma_t(R) \equiv \frac{\overline{\Sigma}(< R) - \Sigma(R)}{\Sigma_{\rm cr}(z_l, z_s)} = \frac{\Delta\Sigma(R)}{\Sigma_{\rm cr}} \,, \tag{2.38}$$

where $\overline{\Sigma}(< R)$ is the average surface density inside that radius, and $\Sigma(R)$ is the average surface density at radius R. $\Delta\Sigma(R)$ is the excess surface mass density, and $\Sigma_{\rm cr}(z_l, z_s)$ is the critical surface mass density of the lens in comoving coordinates given by

$$\Sigma_{\rm cr}(z_l, z_s) = \frac{c^2}{4\pi G} \frac{D_A(z_s)}{D_A(z_l) D_A(z_l, z_s)} \frac{1}{(1+z_l)^2} \,, \tag{2.39}$$

where $D_A(z_l)$, $D_A(z_s)$ and $D_A(z_l, z_s)$ are the angular diameter distances to the lens, sources and between the lens and sources respectively.

The surface mass density of the NFW profile along the line of sight can be expressed by

$$\Sigma(x) = \frac{2\delta_c \rho_s r_s}{x^2 - 1} f(x) \,, \tag{2.40}$$

where $x = r/r_s$ is a dimensionless radial distance and

$$f(x) = \begin{cases} 1 - \frac{2}{\sqrt{x^2-1}} \operatorname{arctan}\sqrt{\frac{x-1}{1+x}} & (x > 1)\,, \\ 1 - \frac{2}{\sqrt{x^2-1}} \operatorname{arctanh}\sqrt{\frac{1-x}{1+x}} & (x < 1)\,, \\ 1/3 & (x = 1)\,. \end{cases} \tag{2.41}$$

The mean surface mass density of the NFW profile is given by

$$\overline{\Sigma}(x) = \frac{2}{x^2}\int_0^x x'\Sigma(x')dx'. \tag{2.42}$$

Integrating Equation 2.42 from 0 to x, we can compute the mean surface mass density as

$$\overline{\Sigma}(x) = \begin{cases} \frac{4}{x^2} r_s \delta_s \rho_c \left[\frac{2}{\sqrt{x^2-1}} \arctan\sqrt{\frac{x-1}{1+x}} + \ln\left(\frac{x}{2}\right)\right] & (x > 1), \\ \frac{4}{x^2} r_s \delta_s \rho_c \left[\frac{2}{\sqrt{1-x^2}} \operatorname{arctanh}\sqrt{\frac{1-x}{1+x}} + \ln\left(\frac{x}{2}\right)\right] & (x < 1), \\ 4 r_s \delta_s \rho_c \left[1 + \ln\left(\frac{1}{2}\right)\right] & (x = 1). \end{cases} \tag{2.43}$$

Therefore, the radial dependence of the excess surface mass density is

$$\Delta\Sigma(x) = \begin{cases} \frac{r_s \delta_c \rho_c}{\Sigma_c} h_>(x) & (x > 1), \\ \frac{r_s \delta_c \rho_c}{\Sigma_c} h_<(x) & (x < 1), \\ \frac{r_s \delta_c \rho_c}{\Sigma_c} \left[\frac{10}{3} + 4\ln\frac{1}{2}\right] & (x = 1), \end{cases} \tag{2.44}$$

where the $h_<(x)$ and $h_>(x)$ functions are given by

$$h_<(x) = \frac{8 \operatorname{arctanh}\sqrt{\frac{1-x}{1+x}}}{x^2\sqrt{1-x^2}} + \frac{4}{x^2}\ln\left(\frac{x}{2}\right) - \frac{2}{(x^2-1)} + \frac{4 \operatorname{arctanh}\sqrt{\frac{1-x}{1+x}}}{(x^2-1)(1-x^2)^{1/2}}, \tag{2.45}$$

$$h_>(x) = \frac{8 \arctan\sqrt{\frac{x-1}{1+x}}}{x^2\sqrt{1-x^2}} + \frac{4}{x^2}\ln\left(\frac{x}{2}\right) - \frac{2}{(x^2-1)} + \frac{4 \arctan\sqrt{\frac{x-1}{1+x}}}{(x^2-1)^{3/2}}. \tag{2.46}$$

2.6.2. The 2nd-halo term

Galaxy clusters exist at the node of the cosmic web, being fed with matter coming along filaments connecting galaxy clusters. Therefore, when studying a galaxy cluster mass profile up to large (typically more than 5 Mpc) cluster centric distance, one begins to be sensitive to the neighbouring clusters. This is accounted for by the 2nd-halo term, whose excess surface mass density is given by:

$$\Delta\Sigma_{\rm 2h}(R) = \overline{\Sigma}_{\rm 2h}(< R) - \Sigma_{\rm 2h}(R)\,. \tag{2.47}$$

The excess mass density at the projected radius (R) is given by

$$\Sigma_{\rm 2h}(R) = 2\rho_{c,0}\Omega_{m,0}\int_0^\infty \xi_{\rm 2h}\left(\sqrt{R^2+\chi^2}\right)\mathrm{d}\chi\,, \tag{2.48}$$

where $\xi_{\rm 2h}(r)$ is the galaxy-matter cross-correlation function, $\rho_{c,0}$ is the critical density, and $\Omega_{m,0}$ is the matter density of the universe at the present time. This function is obtained by multiplying the non-linear matter correlation function $\xi_{nl}(r)$ with the halo bias $b(M)$ given by

$$\xi_{\rm 2h}(r) = b(M)\,\xi_{nl}(r)\,\zeta(r)\,. \tag{2.49}$$

The scale dependence of the halo bias $\zeta(r)$ is given by

$$\zeta(r) = \frac{[1+1.17\xi_{\rm nl}(r)]^{1.49}}{[1+0.69\xi_{\rm nl}(r)]^{2.09}}\,, \tag{2.50}$$

which is more significant at the radius $R \leq 3\ h^{-1}$ Mpc as described in Tinker, Weinberg, Zheng, et al. 2005. In this study, we use the halo bias prescription derived from a cosmological simulation performed within a flat ΛCDM cosmology by Tinker, Robertson, Kravtsov, et al. 2010. The nonlinear matter correlation function is the Fourier transform of the nonlinear matter power spectrum $P_{\rm nl}$,

$$\xi_{\rm nl}(r) = \frac{1}{2\pi}\int k^2\,P_{\rm nl}(k)\,j_0(kr)\,\mathrm{d}k\,, \tag{2.51}$$

where $j_0(kr)$ is the zeroth order of the spherical Bessel function of the first kind. We use the revised halo fit model (Takahashi, Sato, Nishimichi, et al. 2012) and the Code for Anisotropies in the Microwave Background (CAMB) program (Lewis and Challinor 2011) to compute the nonlinear matter power spectrum.

2.6.3. Miscentering effect

The center of mass distribution in galaxy clusters can be shifted from the BCG, due to physical processes in cluster cores. The miscentering profile is given by the projected excess surface mass density of the NFW profile which can be written as follows:

$$\Delta\Sigma^{\rm NFW}_{\rm mis}(R|P(R_{\rm mis})) = \int_0^\infty \Sigma(R|R_{\rm mis})\,P(R_{\rm mis})\,\mathrm{d}R_{\rm mis}\,, \tag{2.52}$$

where $P(R_{\rm mis})$ is the miscentering distribution. It is typically a Gaussian distribution function with the miscentering radius ($R_{\rm mis}$) and parameter ($\sigma_{\rm mis}$):

$$P(R_{\rm mis}) = \frac{R_{\rm mis}}{\sigma^2_{\rm mis}} \exp\left[-\frac{1}{2}\left(\frac{R_{\rm mis}}{\sigma_{\rm mis}}\right)^2\right] . \tag{2.53}$$

Accordingly, the excess surface mass density of miscentering term of the NFW profile is

$$\Sigma(R|R_{\rm mis}) = \frac{1}{2\pi}\int_0^{2\pi} \Sigma(r)\, {\rm d}\theta\,, \tag{2.54}$$

where $r = \sqrt{R^2 + R^2_{\rm mis} - 2RR_{\rm mis}\cos(\theta)}$ is the projected radius at the coordinates (R, θ) related to the miscentering radius (see e.g. Yang, Mo, van den Bosch, et al. 2006; George, Leauthaud, Bundy, et al. 2012; T. McClintock, Varga, Gruen, et al. 2019).

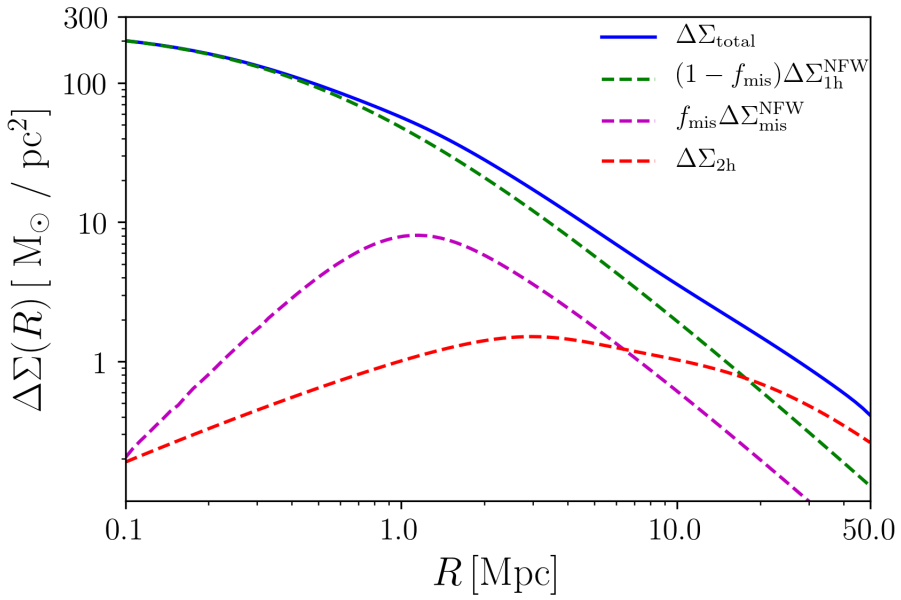

Figure 2.7. – Theoretical profile of the mass distribution in galaxy clusters. The blue solid line shows the theoretical profile defined in Equation 2.33, using $f_{\rm mis} = 0.25$, $\sigma_{\rm mis} = 0.4$ (see e.g. T. McClintock, Varga, Gruen, et al. 2019) and $M_{\rm 200c} = 3.0 \times 10^{14} {\rm M}_\odot$. The dotted lines show the contributions of each component to the profile, as indicated in the plot.

2.6.4. The Concentration-Mass relation

The NFW profile is described by two parameters; the concentration (c) and the total mass (M_{200}). Results from numerical simulations show that the concentration and the total mass (c-M) are related. The c-M relation has also been tested observationally (e.g. N. Okabe, M. Takada, K. Umetsu, et al. 2010). The relation between the concentration and the total mass is an important tool to test the cosmological model and the physical processes in galaxy clusters.

Many studies based on different datasets (both simulated and observational) have been carried out to characterize this relation. For example, Duffy, Schaye, Kay, et al. 2008 studied the c-M relation of the NFW profile using N-body simulations performed in the Wilkinson Microwave Anisotropy Probe year 5 (WMAP5) cosmology, and found an additional dependency between halo masses and redshift, best modeled by a power-law. The results show that the concentration decreases as a function of the total mass and redshift. Later, Dutton and Macciò 2014 studied the c-M relation in the Planck cosmology, finding a relation higher than in the WMAP5 cosmology. They provided the following expression for the concentration mass relation, defined as a power-law

$$\log_{10} c(M) = a + b \log_{10}(M/[10^{12} h^{-1} M_{\odot}]), \tag{2.55}$$

where a and b are given by

$$a = 0.520 + (0.905 - 0.520) \exp(-0.617 z^{1.21}), \tag{2.56}$$

$$b = -0.101 + 0.026 z. \tag{2.57}$$

In my analysis, since the signal-to-noise ratio of our measurement is low, I use this relation to reduce the number of free parameters in our model. This c-M relation is derived from a complete set of simulated clusters which might differ from our sample, especially at low mass where I might miss some clusters. Nonetheless, the previous study from Cibirka, Cypriano, Brimioulle, et al. 2017 on the CODEX clusters shows an excellent agreement with the simulation from Dutton and Macciò 2014.

3. Data Preparation

3.1. DECaLS Data Release 3

In this work, I use the Dark Energy Camera Legacy Survey (DECaLS) catalogs [1] for the weak lensing analysis. This survey is a part of the Dark Energy Spectroscopic Instrument (DESI) Legacy Imaging Survey (Dey, D. J. Schlegel, D. Lang, et al. 2019). It provides the optical imaging for spectroscopic targeting of 2/3 of the DESI footprint. DECaLS uses the Dark Energy Camera (DECam) installed on the Blanco 4 meters telescope, located at the Cerro Tololo Inter-American Observatory in Chile. DECam was constructed in 2008 - 2011 and mounted on the Blanco telescope in September 2012. It consists of sixty-two charge-coupled device (CCD) detectors, arranged in a hexagonal pattern on the focal plane of DECam. Data Release 3 (DR3, PI: D. Schlegel and A. Dey) [2] has been used for

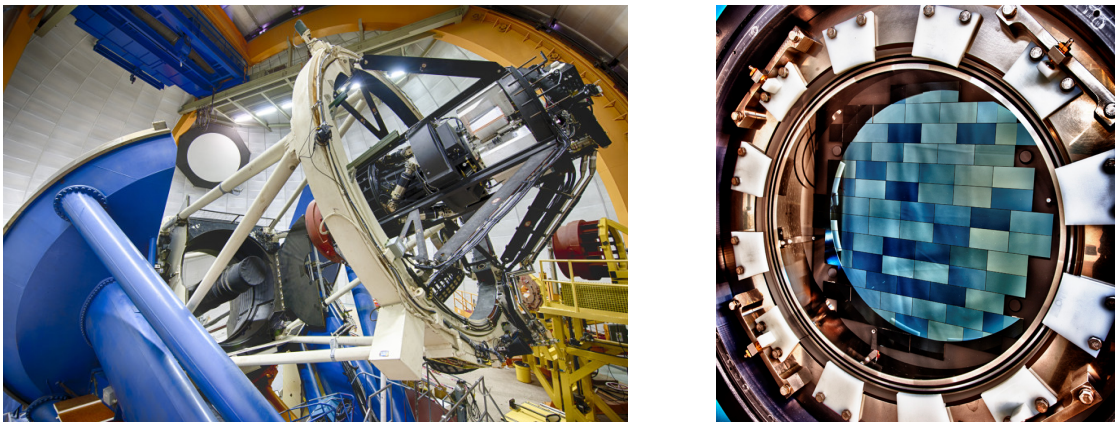

(a) (b)

Figure 3.1. – (a) The DECam is mounted on the Blanco 4-meter telescope. (b) The focal plane of the DECam with 62 CCDs (Credit: R. Hahn, Fermilab)

this analysis. It includes images observed between August 2014 and March 2016, as well as images from the Dark Energy Survey conducted between September 2012 and March 2016. I note that only DECaLS data were used for this study.

1. http://www.legacysurvey.org
2. DECam programs ID: 2013A-0741 and 2014B-0404

The DECaLS DR3 imaging data covers 4300 deg^2 in g-band, 4600 deg^2 in r-band and 8100 deg^2 in z-band.

In total, 4200 deg^2 have been observed in all three optical bands. Figure 3.2 shows the depth of DECaLS DR3 objects observed in three optical bands; g, r and z. The magnitude is about 1.5 to 2.0 magnitudes deeper than the SDSS in r-band (Dey, D. J. Schlegel, D. Lang, et al. 2019). Forced photometry is performed with the Tractor tool (Dustin Lang, Hogg, and David J. Schlegel 2014). In the DECaLS DR3 catalog, the objects from the Tractor catalog are classified into five morphological models: Point sources (PSF), Simple galaxies (SIMP), DeVaucouleurs (DEV), Exponential (EXP), and Composite model (COMP).

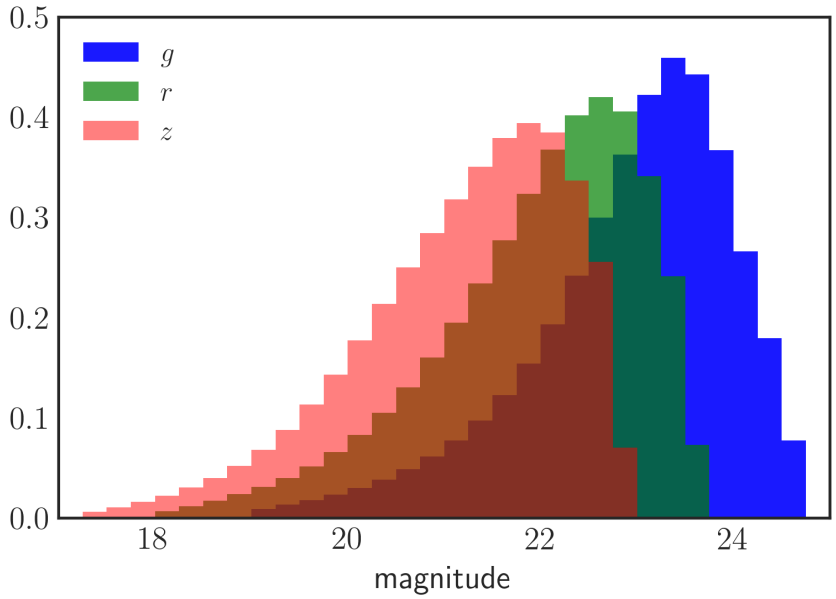

Figure 3.2. – The depth of the DECaLS DR3 objects in three bands; g, r, and z.

Sky-subtracted images are stacked in five different ways: one stack per band, one “flat" Spectral Energy Distribution (SED) stack of all bands, one “red" SED stack of all bands ($g - r = 1$ mag and $r - z = 1$ mag). Sources above 6σ detection limit in any stack are kept as candidates. Thumbnail images around each candidate are extracted. PSF (delta function) and SIMP models convolved by a PSF model are adjusted on the multi-band, multi-exposure image of each candidate. PSF models for individual exposures are determined with the tool PSFEx (Bertin 2011). A source is retained if its penalized χ^2 is increased by 25; sources below this threshold are removed. The source is classified as the better of PSF or SIMP unless adjusting a DEV or EXP profile further improves the χ^2 by 9 (approximately 3σ improvement). A source is updated as COMP (composite between DEV and EXP model) if the penalized χ^2 with this model improves by another 9. These selections imply that any extended source classification

corresponds to at least a 5.8σ detection, and a 6.5σ detection for the COMP model.

3.2. DECaLS Shear catalog

For a gravitational lensing analysis, the ellipticity is a complex number, that depends on the major (a) and minor (b) axes of the morphological model

$$\varepsilon = \frac{a-b}{a+b}\exp(2i\phi) = \varepsilon_1 + i\varepsilon_2\,, \tag{3.1}$$

where ϕ is the position angle relative to the reference frame within a range of $0°$ to $180°$. The ellipticity parameter of the DECaLS DR3 catalog is defined by

$$\varepsilon \equiv \sqrt{1-(b/a)^2}\,. \tag{3.2}$$

Ellipticity parameters ε_1 and ε_2 of the DECaLS DR3 objects were computed for the SIMP, DEV, EXP and COMP models. However, I must calibrate these parameters because they might be affected by systematic errors, for example the imperfect instrument and the atmospheric convolution. Therefore, I model potential measurement bias with a multiplicative (m) and an additive bias (c) (e.g., Catherine Heymans, Van Waerbeke, Lance Miller, et al. 2012; L. Miller, C. Heymans, Kitching, et al. 2013). The additive bias is known to occur from residuals in the anisotropic PSF correction and depends on galaxy sizes. The multiplicative bias occurs from shear measurement, which can be produced by many effects, such as measurement method, blending, and crowding (see e.g., Euclid Collaboration, Martinet, Schrabback, et al. 2019).

To calibrate the DECaLS DR3 shear catalog, I cross-match the DECaLS objects with the Canada France Hawaii Telescope (CFHT) Stripe 82 objects and compute the correction parameters. The CFHT Stripe 82 (CS82) is a survey covering ≈ 170 square degrees of the Sloan Digital Sky Survey (SDSS) Stripe 82 in the equatorial region of the South Galactic Cap. Imaging data are of high quality. They have been taken in excellent seeing conditions between 0.4 - 0.8 arcsec with an average of 0.59 arcsec. The completeness magnitude is $i_{AB} \sim 24$. This imaging survey was primarily designed for lensing analysis (see e.g. Shan, Jean-Paul Kneib, Comparat, et al. 2014; Liu, Pan, Li, et al. 2015).

For each morphological model of the DECaLS DR3 catalog, I calibrate their ellipticity parameters with the CS82 one using the following relation

$$\varepsilon_i^{\rm obs} = (1+m_i)\,\varepsilon_i^{\rm true} + c_i\,; i = 1,2 \tag{3.3}$$

where $\varepsilon^{\rm obs}$ is the observed shape and $\varepsilon^{\rm true}$ is the true shape of the source. For the

multiplicative bias, I assume the following dependency

$$1 + m = \frac{a_0 \exp(-a_1 \times r_g \times magz)}{\log_{10} magz}, \tag{3.4}$$

where r_g is a radius of the objects, $magz$ is the magnitude of the object in the z band, a_0 and a_1 are the results from the fitting with the CS82 data.

I find that many sources are rejected because Tractor is not specific to shape measurement. Moreover, the result in calibrating with the CS82 gave high correction values as shown in Table 3.1. I measured the stacked shear profile of all CODEX cluster sample and found that the shear signal is increasing around 10 - 20 % when I excluded the SIMP objects from the measurement as shown in Figure 3.4. For this reason, I excluded the SIMP objects (45% of the sample) from my lensing analysis.

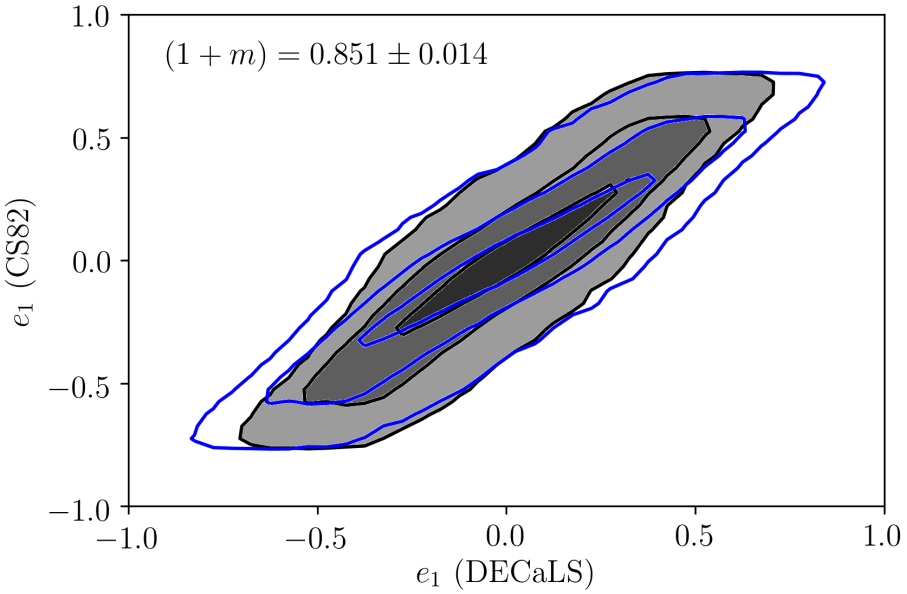

Figure 3.3. – A comparison of the ellipticity 1 (ε_1) between the CS82 objects and the EXP objects for DECaLS DR3 shear catalog before (black solid lines) and after correction (blue solid lines) with the CS82 data. The contour lines indicate the 1σ, 2σ and 3σ respectively.

In addition, the data from DECaLS DR3 catalog were tested with the Obiwan simulations [3]. In these simulations, ELG galaxies simulated with Sersic profiles are pasted into real DECam images. Next, the Tractor tool is re-run to build new catalogs. After matching the simulated positions and the Tractor positions within a five arcsec radius, I obtained about 100,000 galaxies for the calibration. From

3. https://obiwan.readthedocs.io

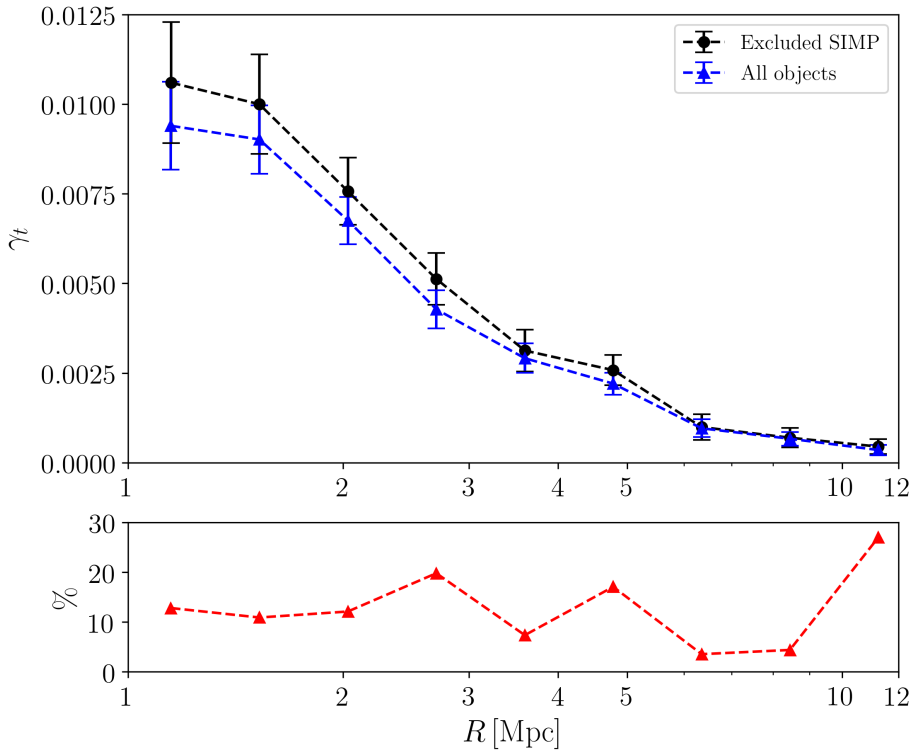

Figure 3.4. – The top figure shows the stacked shear profile of all CODEX cluster sample with all objects and excluded the SIMP object in the measurement and the bottom figure shows the increasing percentage of shear signal when I excluded the SIMP object.

the fitting, I obtained best fit values for the EXP objects, a_0 = 1.33320, a_1 = 0.00656. For the c_2 component, I obtained b_0 = 0.31341, b_1 = -0.02914, b_2 = 0.00067, with the cut in magnitude $magz < 21.3$.

Table 3.1. – The calibration parameters of the DECaLS DR3 shear catalog with the CS82 catalog and Obiwan simulation. This catalog contains 55,866,067 objects.

Type	Number of objects	1 + m (CS82)	1 + m (Obiwan)	c_2 (CS82)	c_2 (Obiwan)
SIMP	25462647	0.697 ± 0.099	-	0.002 ± 0.002	-
EXP	24923051	0.851 ± 0.014	0.896 ± 0.045	0.002 ± 0.002	0.000 ± 0.001
DEV	5404940	0.771 ± 0.078	-	0.004 ± 0.003	-
COMP	75429	0.773 ± 0.108	-	0.007 ± 0.004	-

3.3. Photometric Redshift

Photometric redshifts are commonly used to estimate distances. When an object is moving away from the observer, I can compute its redshift from the differences between the emitting and observed wavelength of that object by, $z = (\lambda_{\rm obs} - \lambda_{\rm emit})/\lambda_{\rm emit}$. It is difficult to measure spectroscopic redshifts in large sky surveys like DECaLS, due to a large number of objects, the depth, and the limitation of the spectroscopic instruments. Therefore, photometric redshifts are often the only remaining solution to estimate object distances.

The GAlaxy redshifts and Physical PARameters tool (GAZPAR) has been used to estimate the redshifts of DECaLS DR3 objects. This technique uses Spectral Energy Distribution (SED) templates and photometric information in three band magnitudes (g, r and z) for each object.

Figure 3.4 shows the photometric redshift between the GAZPAR and the COSMOS 2015 catalogs for DECaLS DR3 objects. I found that the limited number of filters and imaging depth in the DECaLS data provide highly inaccurate photometric redshifts, especially for faint objects, the ones useful for lensing.

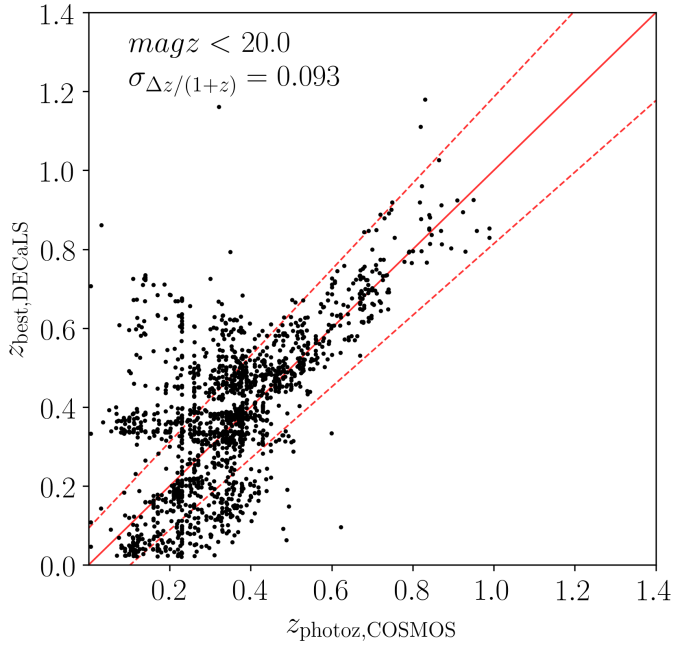
$magz < 20.0$
$\sigma_{\Delta z/(1+z)} = 0.093$
$z_{\mathrm{best,DECaLS}}$
$z_{\mathrm{photoz,COSMOS}}$
0.0
0.2
0.4
0.6
0.8
1.0
1.2
1.4

(a)

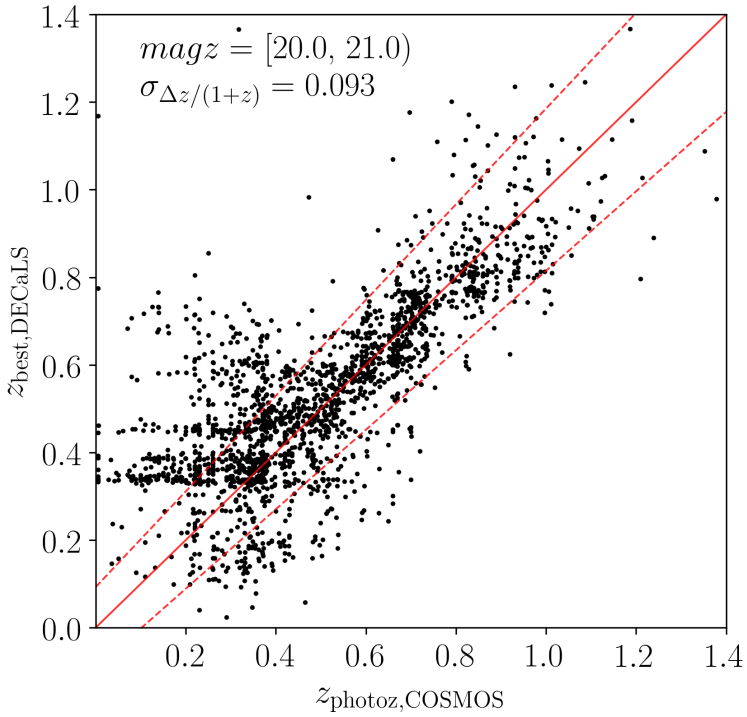
$magz = [20.0, 21.0)$
$\sigma_{\Delta z/(1+z)} = 0.093$
$z_{\mathrm{best,DECaLS}}$
$z_{\mathrm{photoz,COSMOS}}$
0.0
0.2
0.4
0.6
0.8
1.0
1.2
1.4

(b)

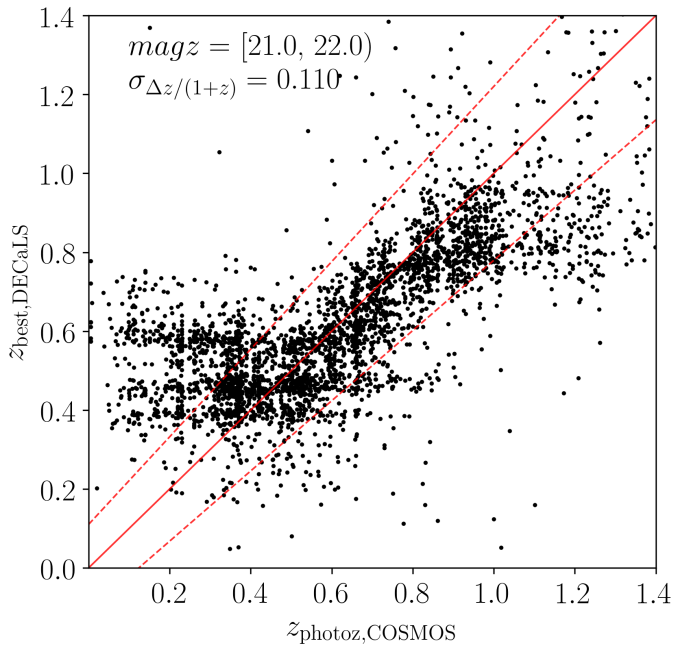

(c)

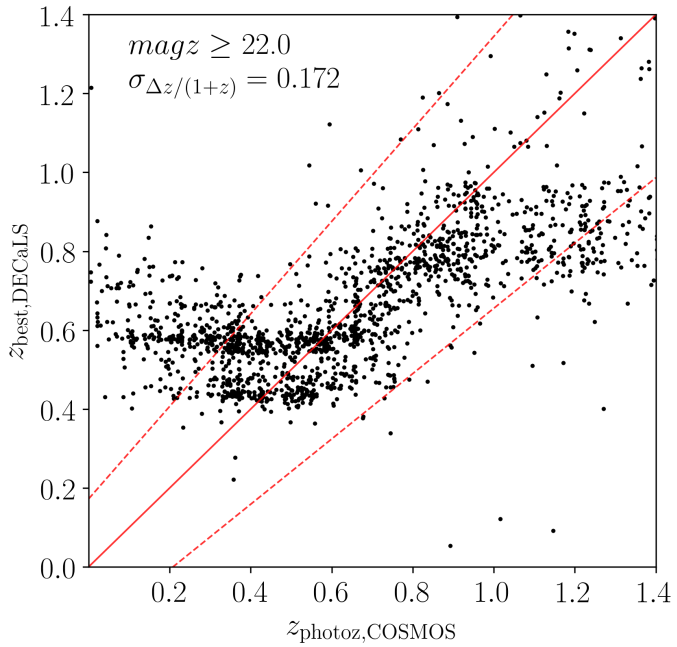

(d)

Figure 3.4. – (a) - (d) Comparisons between the photometric redshifts from the COSMOS 2015 ($z_{\mathrm{photoz,COSMOS}}$) and DECaLS DR3 ($z_{\mathrm{best,DECaLS}}$) catalogs in different z-band magnitude bins ($magz$). Red solid lines show $\Delta z/(1+z) = 0$ and red dashed lines show $\Delta z/(1+z) = \pm\sigma_{\Delta z/(1+z)}$ in each magnitude bin

3.3.1. Color-Color selection

Color - color selection is a useful method to study galaxy evolution. We can use the properties of the color-color diagram to separate or classify galaxies by cutting excessively blue or red galaxies on the color-color diagram (see e.g., Oguri, Bayliss, Dahle, et al. 2012). For this analysis, I use the magnitude of three bands: g, r and z of the DECaLS DR3 shear objects and crossmatch them with the COSMOS 2015 catalog in order to investigate the distribution of DECaLS objects in each point of $g - r$ and $r - z$ color space, using the photometric redshift from the COSMOS 2015.

I plot the distribution of the DECaLS objects in color-color space and examine the distribution of these objects with three groups, z = 0.0 - 0.2, 0.2 - 0.4 and 0.4 - 0.6, using the photometric redshift from the COSMOS 2015 as shown in Figure 3.4. I found that we cannot extract the red-sequence in the color-color diagram for the DECaLS objects due to the high contamination in each redshift bin. Therefore, I did not apply the color-color selection in this analysis because it might affect the amplitude of the shear profile and remove useful galaxies for the weak lensing analysis. I did not find any color-color selections on the color-color diagram to yield a higher signal-to-noise in the lensing measurement than the case of no removal of the foreground galaxies. For this reason, I did not apply the color-color selection for this analysis.

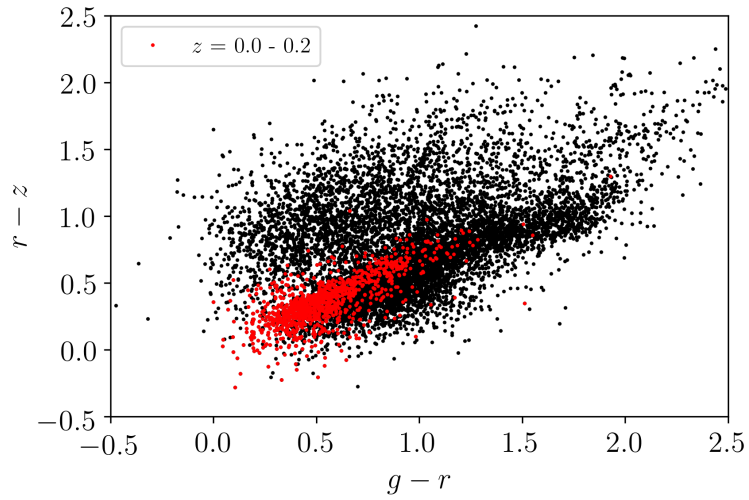
$z = 0.0$ - 0.2
$r - z$
$g - r$
2.5
2.0
1.5
1.0
0.5
0.0
−0.5
−0.5
0.0
0.5
1.0
1.5
2.0
2.5

(e)

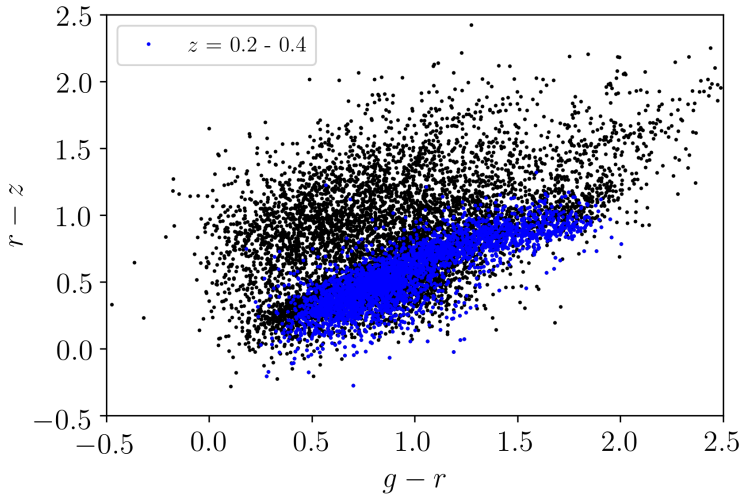
$z = 0.2$ - 0.4
$r - z$
$g - r$
2.5
2.0
1.5
1.0
0.5
0.0
−0.5
−0.5
0.0
0.5
1.0
1.5
2.0
2.5

(f)

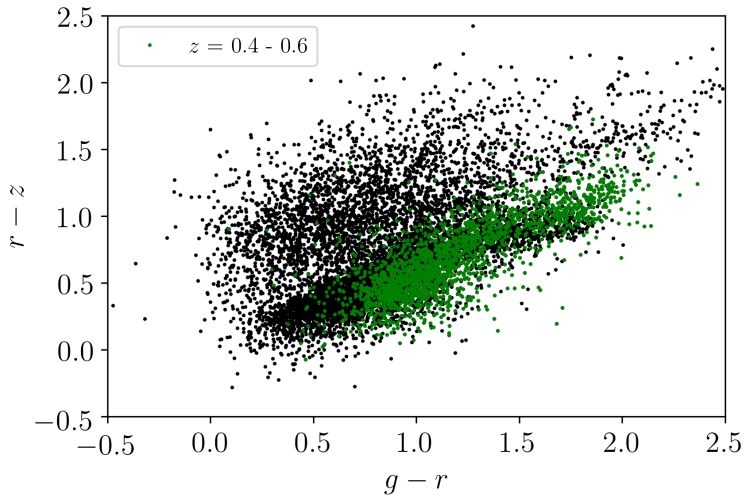

(g)

Figure 3.4. – (a) - (c) The color-color diagram for $g - r$ and $r - z$ of the DECaLS DR3 shear catalog using the photometric redshift from the COSMOS 2015 catalog with the three different redshift bins; z = 0.0 - 0.2, 0.2 - 0.4 and 0.4 - 0.6 respectively.

3.4. Redshift distribution

In the previous section, I have shown the DECaLS DR3 photometric redshift estimation with the GAZPAR tool. The results show a large scatter for faint DECaLS sources when compared with the COSMOS 2015 catalog. For this reason, I did not use the photometric redshift of the DECaLS DR3 objects in this work. I estimate the distance to the DECaLS objects by using the redshift distribution of the DECaLS DR3 shear catalog, following the procedure below. I first consider the following relation between the tangential shear and the excess surface mass density

$$\Delta\Sigma(R) = \gamma_t(R) \left\langle \Sigma_{\rm cr}^{-1}(z_l) \right\rangle^{-1} . \tag{3.5}$$

In practice, I can compute an effective critical surface density (T. McClintock, Varga, Gruen, et al. 2019; Nobuhiro Okabe, Futamase, Kajisawa, et al. 2014) by integrating over the source distribution,

$$\left\langle \Sigma_{\rm cr}^{-1}(z_l) \right\rangle = \frac{\int P(z_{\rm s})\, \Sigma_{\rm cr}^{-1}(z_l, z_s)\, {\rm d}z_s}{\int P(z_{\rm s})\, {\rm d}z_s} , \tag{3.6}$$

where $P(z_{\rm s})$ is the probability distribution function of source galaxies. I estimate the probability distribution function of the DECaLS shear catalog by assuming

that the sources of the DECaLS shear catalog are well fitted with the redshift probability distribution function given by

$$P(z_s) \propto A \left(\frac{z_s}{z_0}\right)^{B-1} \exp\left[-\frac{1}{2}\left(\frac{z_s}{z_0}\right)^2\right], \tag{3.7}$$

where A, B and z_0 are free parameters. I cross-match the DECaLS DR3 shear catalog with the COSMOS 2015 catalog by setting the maximum separation of both catalog to one arcsec. Next, I compute the redshift probability distribution from the photometric redshift of the matched COSMOS 2015 objects. I fit the photometric redshift probability distribution with Equation 3.7 and obtain the best fit values, $A = 2.261 \pm 0.172$, $B = 1.801 \pm 0.173$ and $z_0 = 0.432 \pm 0.035$ as show in Figure 3.5. By inserting the fitting parameters into the probability distribution,

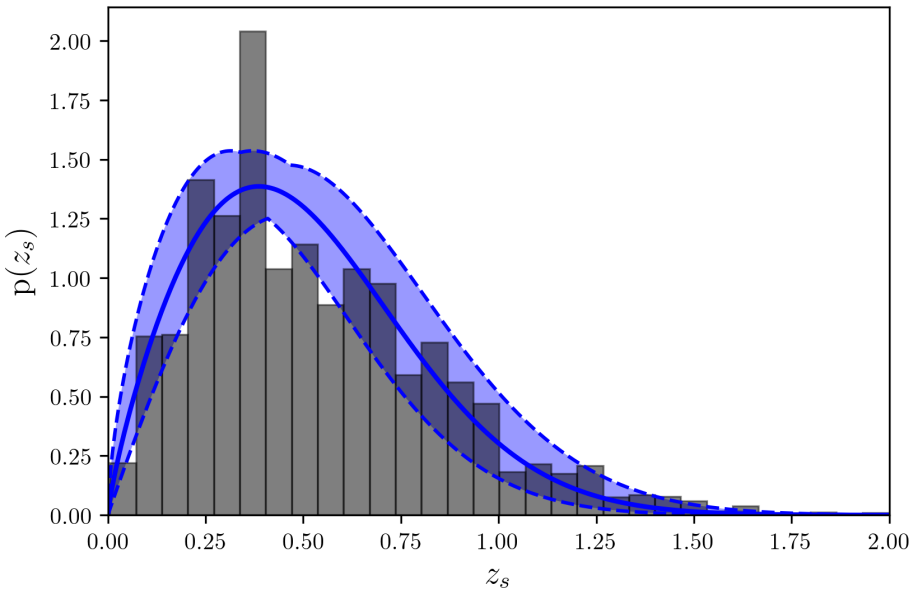

Figure 3.5. – The photometric redshift distribution of the DECaLS DR3 shear catalog obtained by matching it with the COSMOS 2015 catalog (blue solid line) and its 1σ uncertainty (blue shaded area).

I therefore can compute the effective critical density instead of computing the photometric redshift for all sources. Figure 3.6 shows the effective critical excess surface mass density from the cluster redshift $z_{\rm cluster} = 0.1$ to 0.2.

3.4.1. Amplitude correction

In order to estimate the effective critical surface density as described in the previous section, I consider all objects or galaxies along the line-of-sight. Some

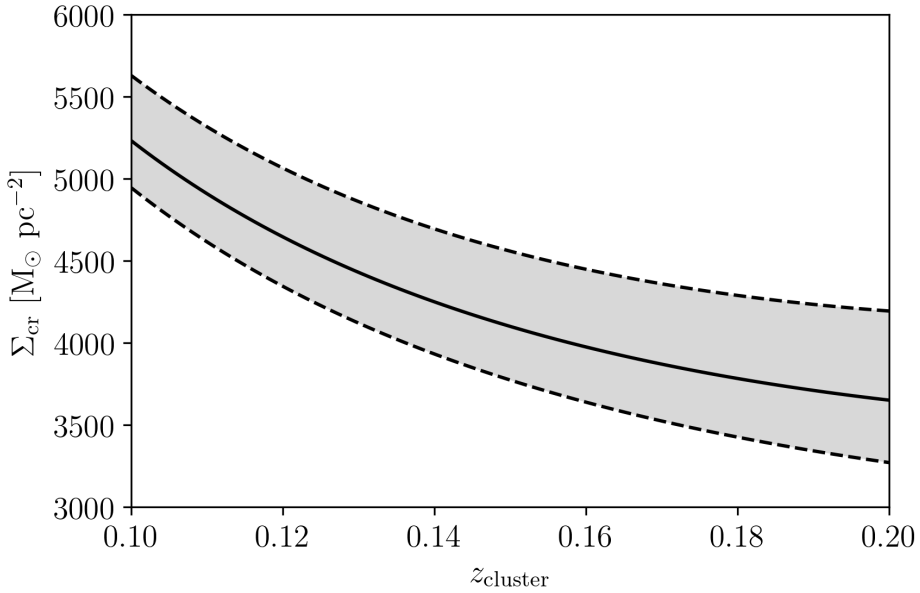

Figure 3.6. – The effective critical surface density of the DECaLS DR3 shear catalog estimated by Equation 3.7. The black solid line is the mean effective critical surface density and the dotted lines show the 1σ confident level (shaded areas).

will dilute the weak lensing signal; for example the foreground galaxies which did not produce the lensing signal. Given the limited color information in our galaxy catalog, I do not remove the foreground galaxies from the shear measurement.

To demonstrate the impact of the contamination by foreground galaxies, I use the redshift probability distribution function from cross-matching the DECaLS DR3 shear catalog with the COSMOS 2015 catalog in the previous section. I therefore compare the integrated lensing critical surface densities $\Sigma_{\rm cr}$ defined in Equation 3.6, when I include all galaxies $(z_{\rm source} > 0)$, and when I remove foreground galaxies located in front of a cluster at redshift $z_{\rm cluster}$. Figure 3.7 shows the amplitude correction (A) defined as

$$\mathrm{A}\ (\%) = \frac{\Sigma_{\rm cr}(z_{\rm source} > 0) - \Sigma_{\rm cr}(z_{\rm source} > z_{\rm cluster})}{\Sigma_{\rm cr}(z_{\rm source} > 0)} \times 100\%\,. \tag{3.8}$$

3.5. CODEX cluster catalog

The gravitational lensing phenomenon is related to the curvature of spacetime induced by foreground objects, such as galaxies or galaxy clusters. In the previous

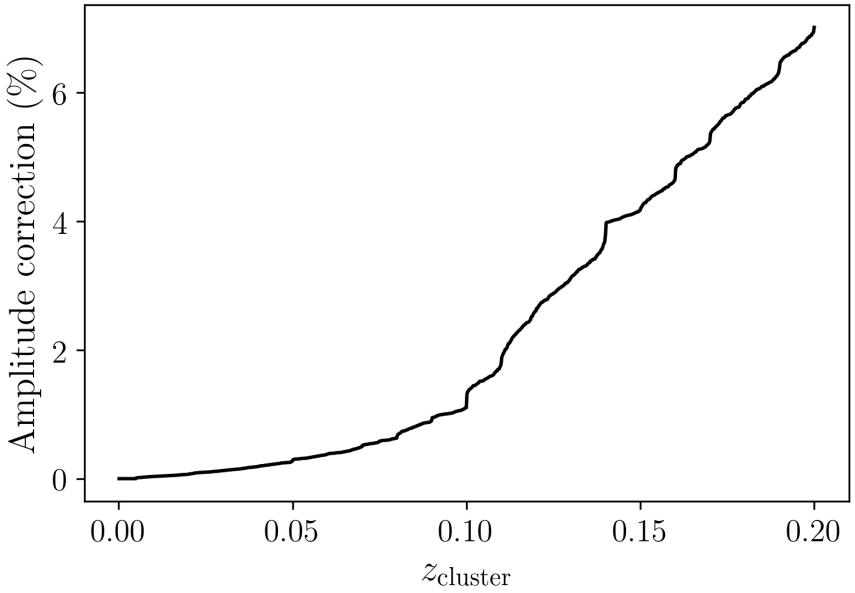

Figure 3.7. – Amplitude correction to apply on $\Delta\Sigma$ to correct the contamination by foreground galaxies.

section, I discussed the DECaLS DR3 shear catalog. I use this catalog as the sample of background galaxies affected by the weak gravitational lensing produced by foreground galaxy clusters. In this work, I use the COnstrain Dark Energy with X-ray (CODEX) galaxy clusters catalog as the sample of foreground objects.

The CODEX cluster catalog was built by identifying X-ray sources in the ROSAT All-Sky Survey data (Voges, Aschenbach, Boller, et al. 1999) using the redMaPPer algorithm (Rykoff, Rozo, Busha, et al. 2014). The CODEX cluster catalog contains cluster redshift, richness (λ_{SDSS}), and position of the optical center determined by the redMaPPer algorithm. Cluster richness is evaluated at two positions, the X-ray and the optical positions. The set of redMaPPer parameters identified at the optical center are annotated with the OPT suffix ($z_{\lambda,\mathrm{OPT}}$, λ_{OPT}, etc.).

A dedicated SDSS-IV SPectroscopic IDentification of eRosita Source (SPIDERS; Dawson, J.-P. Kneib, Percival, et al. 2016; Blanton, Bershady, Abolfathi, et al. 2017) survey was carried out in the period 2014-2018 to get the redshift of CODEX cluster member galaxies. These observations allowed to confirm a high fraction of clusters at $z < 0.4$ (Clerc, Merloni, Zhang, et al. 2016). In addition in DES, Klein, Grandis, J. Mohr, et al. 2018 found that the redMaPPer cluster sample in the redshift range considered in this work ($0.1 < z < 0.2$), and with richness $\lambda > 20$ is 99% clean.

Figure 3.8 shows the comparison between CODEX cluster richness estimates using X-ray and optical centers for clusters located within the DECaLS DR3 footprint. Moreover, I find that the differences between the two sets of richness

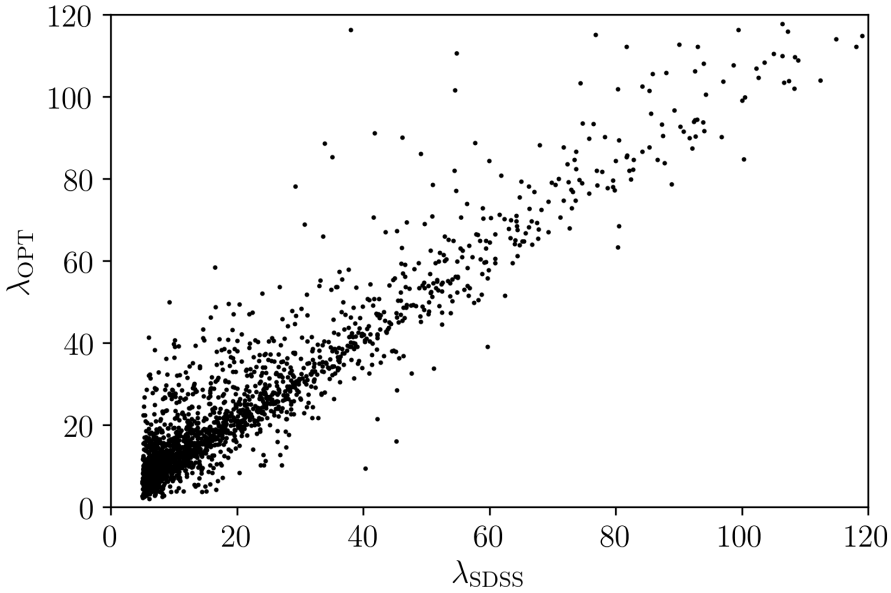

Figure 3.8. – A comparison of the SDSS richness computed by the redMaPPer algorithm ($\lambda_{\rm SDSS}$) and the updated optical richness ($\lambda_{\rm OPT}$) of all CODEX clusters in the DECaLS DR3 survey footprint

parameters show a scatter of about 20% at richness $\lambda_{\rm OPT} = 20$. This relative scatter tends to decrease with richness ($\sim 5\%$ at $\lambda_{\rm OPT} = 120$). In the following, I use redMaPPer parameters with the OPT suffix for the lensing analysis, because it yields higher signal-to-noise measurements. In addition, Clerc, Merloni, Zhang, et al. 2016 highlighted that clusters at redshift $z_{\rm OPT} < 0.1$ are systematically larger than the redshift obtained in spectroscopy with the SPIDERS data. For this reason, I choose clusters at redshift $0.1 \leq z \leq 0.2$, and optical richness $20 \leq \lambda_{\rm OPT} \leq 110$. I reject low richness clusters because they might be contaminated by projected structures along the line-of-sight. I cross-match the CODEX clusters with the DECaLS DR3 data and select the galaxy clusters located in the DECaLS DR3 survey footprint. The final subsample of CODEX clusters for our weak lensing analysis contains 279 clusters.

In addition, I plot the sky coverage and the number density of the DECaLS DR3 shear catalog overlapped with our weak lensing sample of CODEX clusters in Figure 3.9.

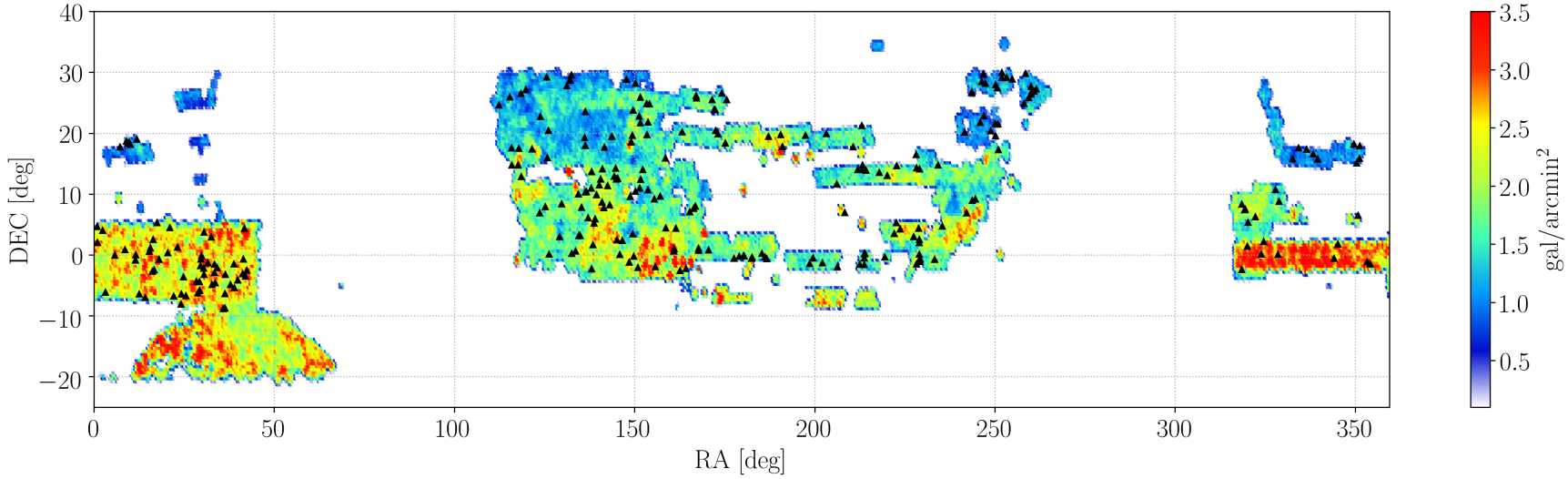

Figure 3.9. – Sky coverages of the DECaLS DR3 shear catalog and the CODEX cluster sample (black triangle) in Equatorial coordinates. The color bars show the number density of background galaxies per square arcmin.

3.6. The objectives of this study

To understand the physical properties and evolution of the universe, galaxy clusters are privileged objects of investigation. In this study, I use wide-field optical observations from the Dark Energy Survey Camera (DECam) to study the weak gravitational lensing effect produced by galaxy clusters. I use the 3^{rd} public release of the photometric catalogs provided by the DECam Legacy Survey (DECaLS), which covers about 4000 deg^2. In addition to photometric information, these catalogs contain galaxy shape (ellipticity) parameters e_1 and e_2. However, these parameters must be calibrated before they can be used in weak lensing analyses. I use the Canada-France-Hawaii Telescope Stripe 82 Survey (CS82) to calibrate the DECaLS shape parameters. Moreover, I estimate photometric redshift distributions, so that I can compute the excess surface mass density profile.

The objective of this study is to compute the mass-richness scaling relation for the CODEX clusters. A scaling relation is an empirical relationship between two observable quantities, the cluster richness and its total mass in the case of the mass-richness relation. The scaling relation is beneficial because it allows a quick determination of masses of a large number of galaxy clusters in future surveys, such as Euclid.

The main scientific objectives of this study are separated into the following topics:

(1) Estimate the total mass of CODEX clusters with weak lensing measurements derived from DECaLS DR3

(2) Study the scaling relation between cluster masses and their richness

(3) Compare the weak lensing mass and the dynamical mass in order to test the hypothesis that galaxy clusters are in the hydrostatic equilibrium state

4. Data Analysis

In order to study the weak-lensing signal produced by the CODEX galaxy clusters, I use the excess surface mass density estimator. This estimator indicates the over-density or under-density of the mass distribution around an object. In our case, I study the over-dense mass distribution around galaxy clusters; in other words, the mass distribution is radially decreasing from the cluster centres. There are many models to describe the mass distribution, or often called the mass profile of galaxy clusters. In this analysis, I use the NFW profile to model the density profile of the CODEX clusters. For consistency with previous measurements, I adopt a concordance ΛCDM model with the cosmological values : Ω_m = 0.3, Ω_Λ = 0.7, σ_8 = 0.8, n_s = 0.965 and a Hubble constant H_0 = 100 h km s^{-1} Mpc^{-1} with h = 0.7. In the following, errors are quoted at the 68% confidence level (1σ).

4.1. Stacking galaxy clusters

The weak lensing analysis of galaxy clusters requires high quality and deep imaging data. The DECaLS DR3 data is not sufficient to measure the weak lensing signal (shear signal) of individual clusters due to the low number density of the sources due to the limited depth of the imaging data, and the shape measurement algorithm. Indeed, as discussed above, I am only able to calibrate the shape of EXP, DEV and COMP type sources, leaving aside a large fraction (>50%) of sources. I therefore apply the stacking technique to enhance the weak lensing signal. The stacking technique is a method, in which I group the galaxy clusters according to an observed property (e.g., optical richness or X-ray luminosity), and measure the averaged lensing signal produced by that group of clusters. The stacked excess surface mass density can be written in terms of the summation of the tangential shear over N background galaxies i, which are found within an annular region centered at radius R for each cluster. The corresponding expression is

$$\Delta\Sigma(R) = C(R)\frac{\sum_{\mathrm{i}=1}^{N} w_{\mathrm{i}}\gamma_{\mathrm{t,i}}(R)\left\langle\Sigma_{\mathrm{cr}}^{-1}\right\rangle^{-1}}{\sum_{\mathrm{i}=1}^{N}(1+m)w_{\mathrm{i}}}, \tag{4.1}$$

where $C(R)$ is a boost factor discussed below, and w is a weight that derives from the shape measurement error and minimizes the variance of the shear estimator.

Furthermore, I examine the stacked excess surface mass density of the CODEX cluster samples. The lack of sources and the high contamination by cluster member galaxies in the inner region (ex., R < 1 Mpc) generate a very noisy signal. I therefore exclude that region to avoid any bias. Conversely to gain more signal, I extend our measurements to large radius. For this reason, I append a large-scale two halo term in our theoretical profile,

$$\Delta\Sigma(R) = \Delta\Sigma_{\rm 1h}^{\rm NFW}(R) + \Delta\Sigma_{\rm 2h}(R)\,. \tag{4.2}$$

It is well defined and agrees with the weak lensing signal at radius $1 < R < 30$ Mpc.

4.1.1. Optical richness

To understand the properties of the large-scale structure, and in particular galaxy clusters, I can consider empirical scaling relations between cluster mass and some physical parameters. The optical richness is related to the number of galaxies in a galaxy cluster. There are many definitions of optical richness. For instance, Rykoff, Rozo, Busha, et al. 2014 defines the optical richness in terms of the summation of the membership probabilities (P) over all galaxies in an aperture around the cluster centre,

$$\lambda = \sum P\theta_L\theta_R \tag{4.3}$$

where θ_L and θ_R are the luminosity and radius-dependent weights described by Rozo, Rykoff, Becker, et al. 2015. For the lensing analysis, I group the galaxy clusters according to their updated optical richness parameter λ_{OPT}. In Figure 4.1, I plot the distribution of CODEX cluster samples between the cluster redshift and the optical richness. In addition, I measure the stacked mass profile of CODEX cluster samples by separating them into three richness groups; λ_{OPT} = 20 - 30, 30 - 50 and 50 - 110.

4.1.2. Correction factor

As mentioned above, a correction factor $C(R)$ is included in the stacking procedure. This parameter accounts for the contamination in our background galaxy sample by galaxies that might be associated with the clusters (see e.g. Fischer, McKay, Sheldon, et al. 2000; Simet, Tom McClintock, Mandelbaum, et al. 2017). This effect will dilute the amplitude of the shear signal, especially in the inner region of a galaxy cluster. To test this effect, I stack CODEX clusters in the radial range $0.1 \leq R <$ 30 Mpc. For background galaxies with index i, around N lenses with index j, and background galaxies with index k, around $N_{\rm rand}$ random

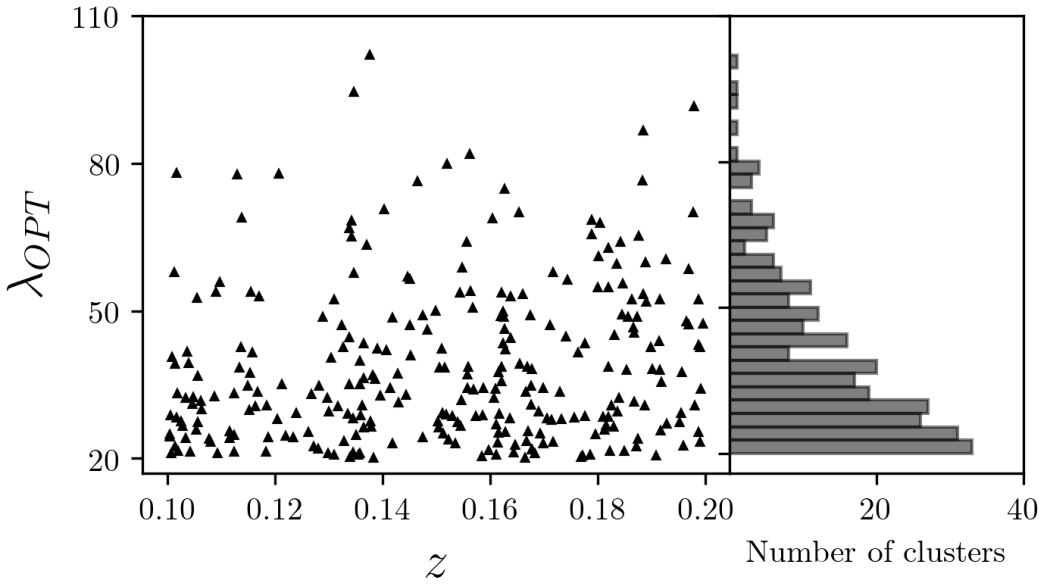

Figure 4.1. – The 2D distribution of CODEX cluster optical richness and redshift for our weak lensing analysis.

points with index l, the correction factor is given by

$$C(R) = \frac{N_{\rm rand}}{N} \frac{\sum_{\rm i,j} w_{\rm i,\,j}}{\sum_{\rm k,\,l} w_{\rm k,\,l}}. \tag{4.4}$$

Compared to previous works, I adapt the method to estimate the correction factor by drawing 10 random positions in a 1.5 degrees aperture from the cluster centers, instead of drawing random points in the full survey footprint. This is justified by the fact that cluster density is very low, and our survey footprint is very irregular. I found that the variation of the boost factor profile is less than 5% within the size of the aperture.

Figure 4.2 shows the results for the correction factor of stacked CODEX clusters; it goes up to $\approx$ 4% in the inner region. Nevertheless, in the outer region (ex. $R >$ 1 Mpc), the correction factor is less than 1%. In my lensing analysis, I measure the mass density profile of the CODEX clusters in the radial range $1.0 \leq R < 30.0$ Mpc. Consequently, our measurements are very little affected by the dilution due to contaminating cluster member galaxies in our background galaxy sample.

4.2. Error estimation

In this section, I discuss statistical noise in the weak lensing measurement. Many effects contribute to the statistical noise in the cluster mass estimates,

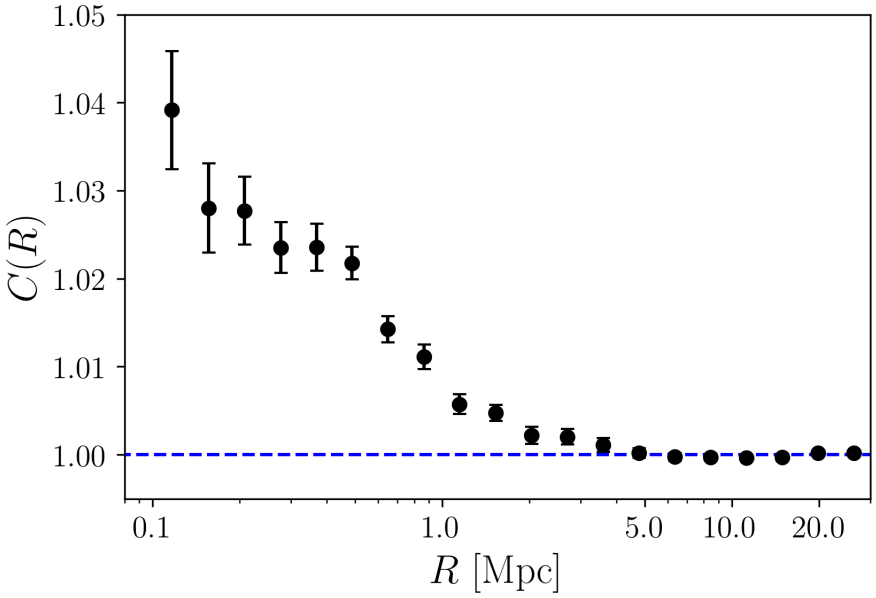

Figure 4.2. – The cluster member galaxy correction factor for CODEX clusters as a function of cluster radius in the range $0.1 \leq R < 30$ Mpc.

for example, the intrinsic shape of source galaxies, the number of lens-source pairs and the fluctuations of the large-scale structure along the line-of-sight (e.g. Shirasaki, Masahiro Takada, Miyatake, et al. 2017). To estimate the statistical errors in stacked cluster measurements, I use the following Jackknife technique : (i) Randomly draw ten positions within a 1.5 degrees aperture from true cluster positions (ii) Employ the delete-1 Jackknife technique in each realization by removing one cluster from the stacked profile and average the lensing profiles for true and random clusters (iii) Repeat the measurement for each Jackknife configuration. The covariance matrix of stacked clusters for the Jackknife is given by

$$\mathbf{C} \equiv C_{ij} = \frac{N_{\rm JK}-1}{N_{\rm JK}} \sum_{m=1}^{N_{\rm JK}} \left(\Delta\Sigma_i^m - \overline{\Delta\Sigma}_i\right)\left(\Delta\Sigma_j^m - \overline{\Delta\Sigma}_j\right) . \tag{4.5}$$

where i and j indicate the radial bins, $\Delta\Sigma^m$ is the excess surface mass density for each of the m-th Jackknife realization. The covariance matrix is used to calculate the log-likelihood function of the theoretical profile given the measurements. In equation above, the average excess surface mass density of the Jackknife configuration is defined by

$$\overline{\Delta\Sigma} \equiv \frac{1}{N_{\rm JK}} \sum_{m=1}^{N_{\rm JK}} \left(\overline{\Delta\Sigma}^m_{\rm true} - \overline{\Delta\Sigma}^m_{\rm random}\right) , \tag{4.6}$$

where $\overline{\Delta\Sigma}_{\text{true}}$ is the mean excess surface mass density of true cluster positions, and $\overline{\Delta\Sigma}_{\text{random}}$ is the mean excess surface mass density around random positions in each Jackknife configuration. Notwithstanding, the covariance matrix of the Jackknife is underestimated due to the noise level. I therefore multiply the inverse covariance matrix ($\mathbf{C}^{-1}$) by the Hartlap factor (H) ,

$$H = \frac{N_{\text{JK}} - p - 2}{N_{\text{JK}} - 1}\,, \tag{4.7}$$

where N_{JK} is the number of Jackknife configurations and p is the number of measured radial bins (Hartlap, Simon, and Schneider 2007).

Instead of showing the covariance matrix in each richness group, I rather show the Pearson correlation coefficient matrix in Figure 4.2. I derive the correlation coefficient matrix (R) from the covariance matrix (C), such that

$$R_{ij} = \frac{C_{ij}}{\sqrt{C_{ii} * C_{jj}}}\,. \tag{4.8}$$

The values of the correlation coefficient are between -1 and +1, where -1 corresponds to a negative correlation, 0 is no correlation, and +1 is a positive correlation. Overall, I observe no particular cross-correlation between the radial bins of the measurements in any group of clusters.

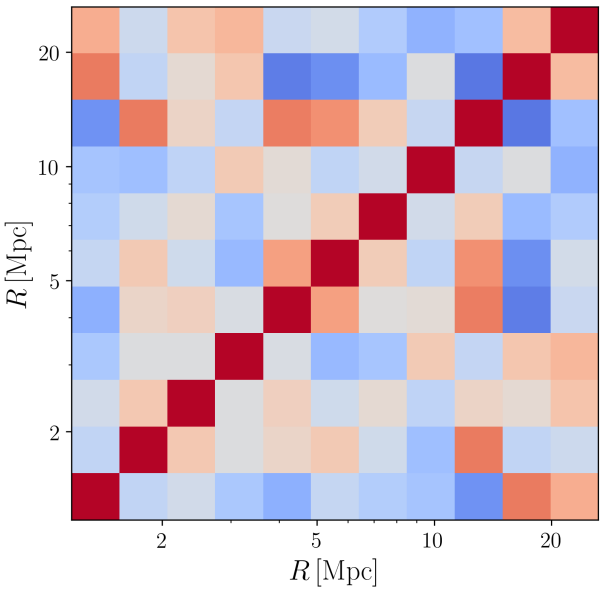

(a)

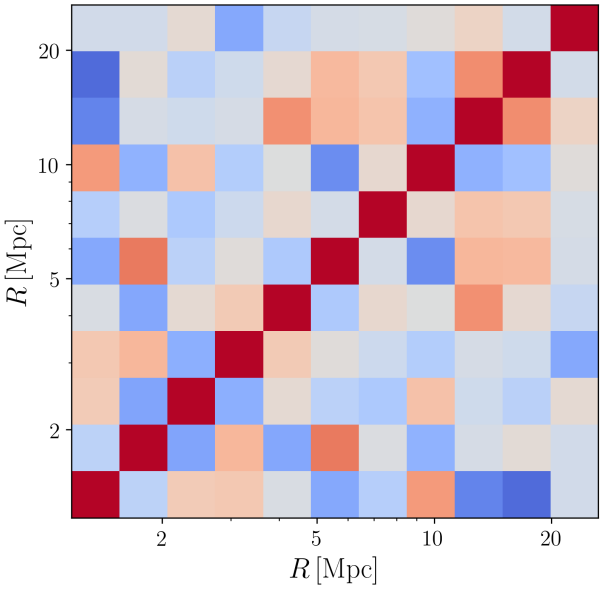

(b)

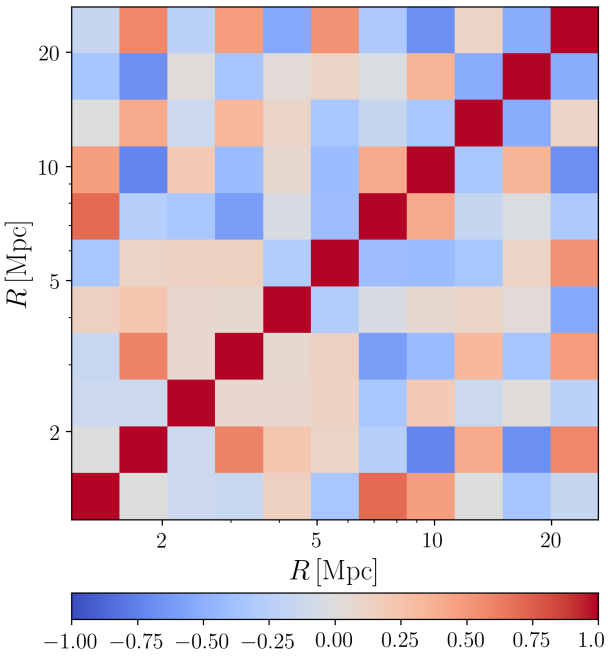

(c)

Figure 4.2. – (a) - (c) The correlation coefficient matrix for the 3 richness groups of stacked galaxy clusters estimated with the Jackknife method.

4.3. Fitting

In this section, I discuss my procedure to fit the measured mass profile in each group. First, I consider the measured excess surface mass density profile of the stacked galaxy clusters, which can be written as a two-dimensional matrix

$$\mathbf{\Delta\Sigma} = \begin{bmatrix} \Delta\Sigma_1(R_1) & \Delta\Sigma_2(R_1) & \cdots & \Delta\Sigma_m(R_1) \\ \Delta\Sigma_1(R_2) & \Delta\Sigma_2(R_2) & \cdots & \Delta\Sigma_m(R_2) \\ \vdots & \vdots & \ddots & \vdots \\ \Delta\Sigma_1(R_n) & \Delta\Sigma_2(R_n) & \cdots & \Delta\Sigma_m(R_n) \end{bmatrix}, \tag{4.9}$$

where the rows correspond to n radial bins, and the columns represent measurements for m galaxy clusters. Then, I use the Markov Chain Monte Carlo method to find the best-fit and the error on each parameter of the theoretical model.

The Markov Chain Monte Carlo (MCMC) method is a resampling technique based on probability distributions. I use the emcee package written in Python (Foreman-Mackey, Hogg, Dustin Lang, et al. 2013) to find the posterior distributions for each parameter. I set the number of walkers, burn-in(s) and production samples to 48, 1000 and 10000 respectively. The log-likelihood function of the

measurements ($\Delta\Sigma^{\rm obs}$) is given by

$$\ln\mathcal{L}(\Delta\Sigma^{\rm obs}|\Delta\Sigma^{\rm model}) \propto -\frac{1}{2}\mathbf{D}^{\rm T}\mathbf{C}^{-1}\mathbf{D} \tag{4.10}$$

where $\mathbf{C}$ is the covariance matrix estimated with the Jackknife technique described in Section 4.2, and $\mathbf{D} = (\mathbf{\Delta\Sigma}^{\rm obs} - \mathbf{\Delta\Sigma}^{\rm model})$ is the difference between the observed and the modeled excess surface mass density, which can be written in the form of a two-dimensional matrix,

$$\boldsymbol{D} = \begin{bmatrix} \Delta\Sigma_1^{\rm obs}(R_1) - \Delta\Sigma_1^{\rm model}(R_1) & \cdots & \Delta\Sigma_m^{\rm obs}(R_1) - \Delta\Sigma_m^{\rm model}(R_1) \\ \Delta\Sigma_1^{\rm obs}(R_2) - \Delta\Sigma_1^{\rm model}(R_2) & \cdots & \Delta\Sigma_m^{\rm obs}(R_2) - \Delta\Sigma_m^{\rm model}(R_2) \\ \vdots & \ddots & \vdots \\ \Delta\Sigma_1^{\rm obs}(R_n) - \Delta\Sigma_1^{\rm model}(R_n) & \cdots & \Delta\Sigma_m^{\rm obs}(R_n) - \Delta\Sigma_m^{\rm model}(R_n) \end{bmatrix} . \tag{4.11}$$

similar to the one described above in Equation 4.9.

4.4. Testing the non-lensing mode in the data

In this section, I make a systematic test on the ellipticity parameters of the DECaLS DR3 shear catalog. Generally, I can separate the shear component into the tangential shear (γ_t) and cross shear component ($\gamma_\times$). In theory, gravitational lensing does not produce a cross shear component. For this reason, I can measure the cross shear or non-lensing mode to reveal systematic errors in the measurement, and quantify possible biases in the shape measurement procedure. I recall the cross shear ($\gamma_\times$) can be computed from the imaginary part of the ellipticity measurements,

$$\gamma_\times = -\mathbf{Im}[\gamma e^{-2i\phi}] = -\gamma_1 \sin(2\phi) + \gamma_2 \cos(2\phi) \, . \tag{4.12}$$

where ϕ is an angle between the reference frame and the source. I split our CODEX cluster sample in richness bins as λ = 20 - 30, 30 - 50 and 50 - 110, and compute the cross shear in the radial range $1.0 \leq R < 30.0$ Mpc. I show the cross shear component of the DECaLS DR3 shear catalog for the CODEX clusters sample in Figure 4.3. It is almost statistically consistent with zero at all radius.

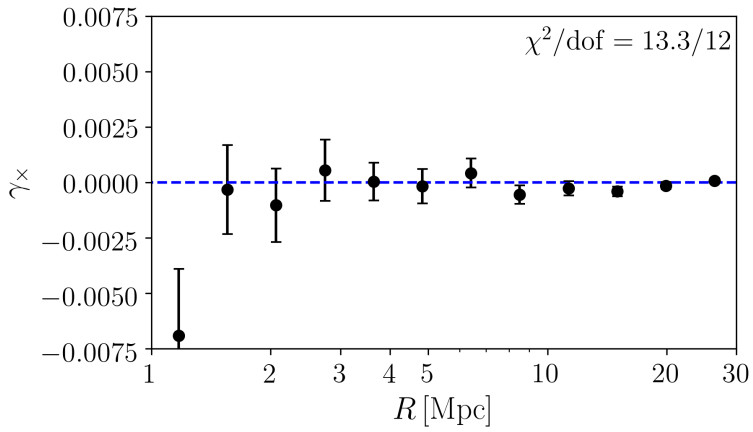

(d) λ = [20, 30)

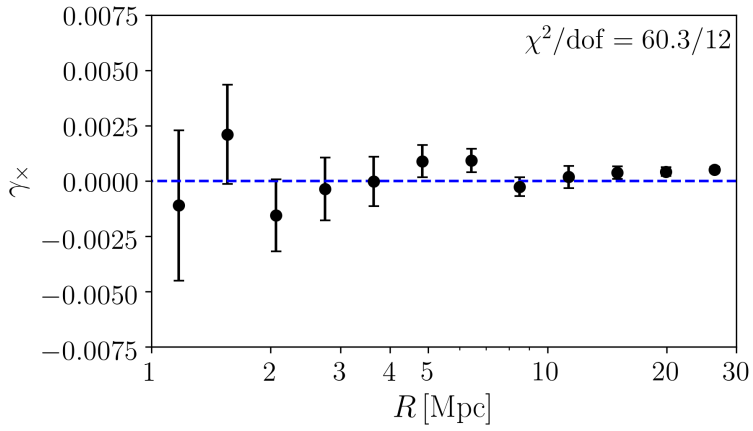

(e) λ = [30, 50)

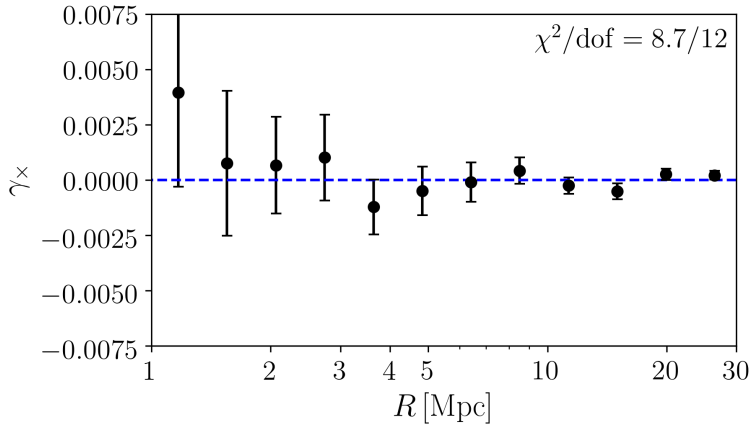

(f) λ = [50, 110)

Figure 4.3. – (a) - (c) The cross shear profiles of stacked galaxy clusters in three richness groups. The degree of freedom is equal to 12 for 12 radial bins.

5. Results

In this chapter, I show the results for the weak lensing analysis of the CODEX cluster sample using the DECaLS DR3 shear catalog. For this analysis, I follow two different approaches and compare the results. This gives me more confidence in the robustness of my conclusions. In the first approach, I stack galaxy clusters into three richness groups. In each group, I fit the stacked profile with the theoretical model defined, and estimate the cluster mass. The relation between the group richness and mean cluster mass gives me an idea about the scaling relation between these two quantities. For the second approach, I start by assuming a mass-richness scaling relation with some free parameters. Given a set of parameter values, I compute a mass and a lensing density profile for each cluster given their richness. I compare this profile to the the weak lensing signal for each cluster to estimate the best fit parameter values.

5.1. CODEX cluster sample

In this first analysis approach, I separate the CODEX clusters into three richness groups and stack their excess surface mass density profile ($\Delta\Sigma$); λ = 20 - 30, 30 - 50 and 50 - 110. I first measure the tangential shear profile of each CODEX cluster in the radial range 1.0 $\leq R <$ 30 Mpc (12 bins), avoiding the effect of miscentering and the lack of sources in the inner radial bins. After that, I compute the effective critical surface density for each richness group. I stack the clusters in their respective richness group, using Equation 4.1 to compute the average excess surface mass profile. For the theoretical model defined in Equation 4.2, I consider the two halo term, which contains three free parameters: the concentration (c), the cluster mass (M_{200c}), and the halo bias ($b(M, z)$). However, I can not set them as a free parameter due to the low S/N and fluctuations at a large radius. I therefore constraint the relationship between the $c - M_{200c}$ relation using the expression by Duffy, Schaye, Kay, et al. 2008 and the halo bias from Tinker, Robertson, Kravtsov, et al. 2010. Thus, I only have one free parameter to fit, the cluster mass (M_{200c}).

From the fitting procedure, I use a MCMC method and I set the a flat prior for the cluster mass M_{200c} = [13.0, 15.0]. I obtain the mean cluster mass for each group. Nevertheless, I find high fluctuations at large radius (e.g., $R > 5$ Mpc). To check for consistency, I recompute the cluster masses by measuring the stacked profile in the inner region $1.0 \leq R < 5.5$ Mpc, and fit with only the first halo term,

i.e. the NFW profile. The results of the fit are shown in Table 5.1 and Figure 5.1. I note that the differences on the cluster masses between the two regions (inner and all radius) reach up to about 15 - 25 %. I guess this is due to the high uncertainties at large radius; However, the results remain in agreement within the 2σ confidence level.

Table 5.1. – The results from the mass measurements of the CODEX clusters in three richness bins.

Richness Group	$N_{cluster}$	z_{mean}	$\lambda_{opt,\,mean}$	M_{200c}^{1h} (10^{14} $M_\odot$)	χ^2_{1h} / dof	M_{200c}^{1h+2h} (10^{14} $M_\odot$)	χ^2_{1h+2h} / dof
[20, 30)	109	0.148	24.83 ± 2.98	$2.19^{+0.39}_{-0.37}$	1.17 / 4	$1.91^{+0.27}_{-0.27}$	6.91 / 10
[30, 50)	110	0.152	38.90 ± 5.86	$2.98^{+0.44}_{-0.42}$	3.70 / 4	$2.37^{+0.32}_{-0.32}$	9.58 / 10
[50, 110)	60	0.158	63.86 ± 11.65	$5.91^{+0.82}_{-0.79}$	7.15 / 4	$5.02^{+0.52}_{-0.50}$	13.52 / 10

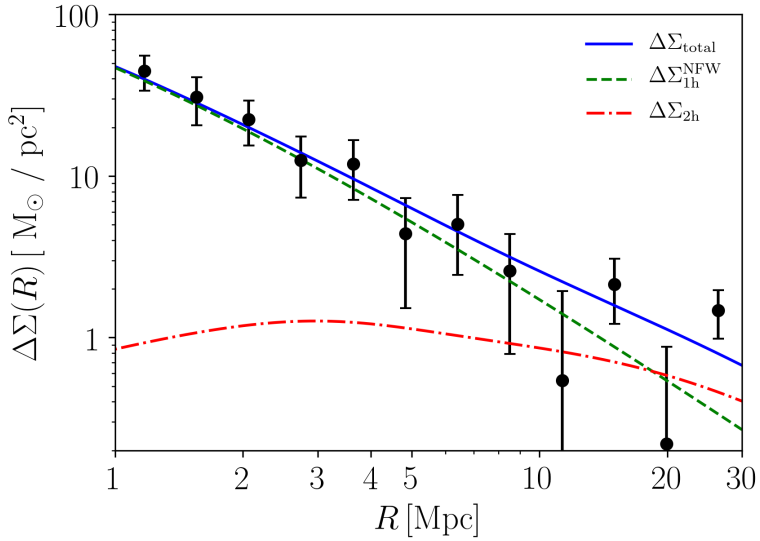

(a) λ = [20, 30)

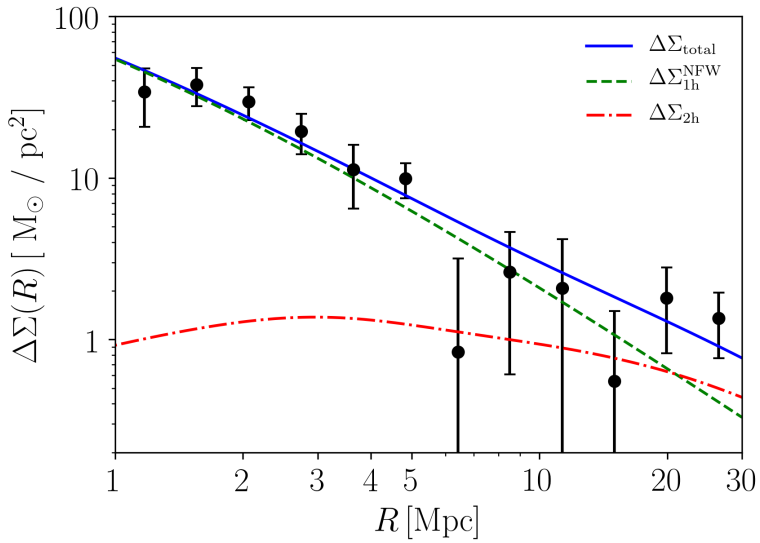

(b) λ = [30, 50)

Figure 5.1. – (a) - (b) The excess surface mass density profiles of CODEX clusters. The blue line shows the theoretical mass profile defined in Equation 4.2 with the first halo term in green and second halo term in red dashed line.

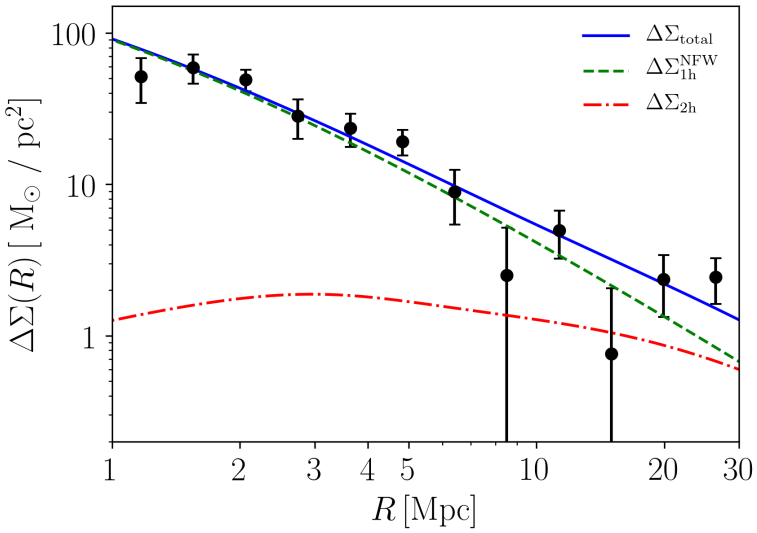

(c) λ = [50, 110)

Figure 5.1. – (c) The excess surface mass density profiles of CODEX clusters. The blue line shows the theoretical mass profile defined in Equation 4.2 with the first halo term in green and second halo term in red dashed line. (cont.)

5.2. Scaling relation

A scaling relation is proportionality relation between two parameters, for example, an observable quantity and a hidden property estimated with a model. In this work, I focus on the relationship between the richness parameter (λ) and the cluster mass (M_{200c}). In the previous section, I showed that the excess surface mass density profile presented large fluctuations at large radius in our measurement. I therefore restricted the measurements to the inner region (1.0 $\leq R <$ 5.5 Mpc) and constrained the $c - M_{200c}$ relation using the expression from Dutton 2011.

To determine the scaling relation, I assume that the mass-richness relation of CODEX clusters is well defined by a power-law relation given by

$$\langle M_{200c}|\lambda\rangle = M_0 \left(\frac{\lambda}{\lambda_0}\right)^{F_\lambda}, \tag{5.1}$$

where M_0 is the mean cluster mass at the richness $\lambda = 40$, and F_λ is the richness scaling index. In this relation, I exclude the evolution term, because my CODEX cluster sample lies in a narrow redshift range, and therefore does not bring any constrain on the redshift evolution of this relation. I use the same MCMC method as above, and set the priors on the mass-richness relation parameters to $\log_{10} M_0$

= [13.0, 15.0] and F_λ = [-10.0, 10.0]. I also set the initial parameters to $\log_{10}M_0$ = 14.0 and F_λ = 0.1. In Figure 5.2, I plot the posterior distribution functions of the mass-richness relation parameters. From the posterior distribution functions,

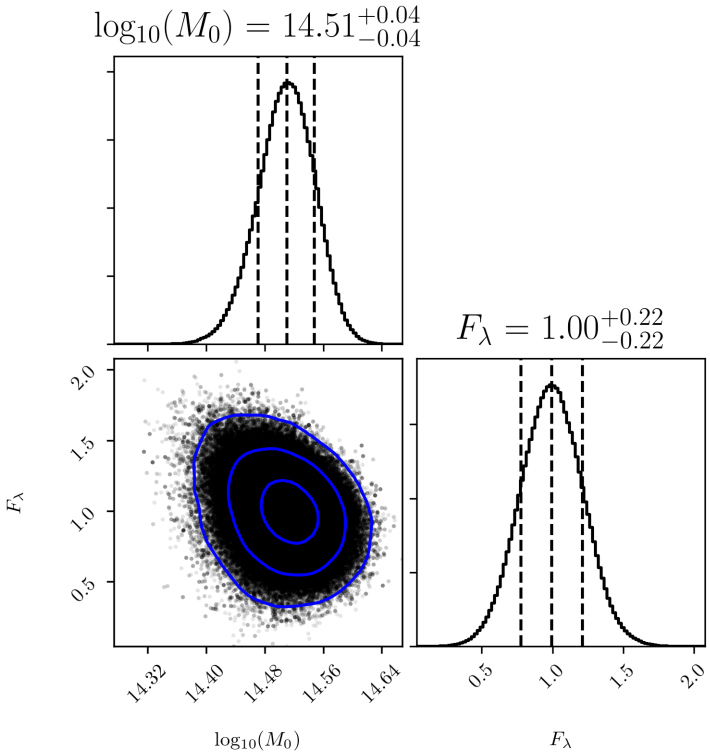

Figure 5.2. – Posterior distribution functions of the mass-richness relation parameters for CODEX cluster sample. Vertical dashed lines show the 68% confidence levels, and contour lines (blue solid lines) indicate 1σ, 2σ and 3σ confidence levels respectively.

I can estimate the mean cluster mass of the CODEX cluster sample

$$M_0 = 3.24^{+0.29}_{-0.27} \times 10^{14}\,\mathrm{M}_\odot\,, \tag{5.2}$$

and the richness scaling index,

$$F_\lambda = 1.00^{+0.22}_{-0.22}\,. \tag{5.3}$$

The small error on F_λ indicates that the cluster mass and richness are strongly correlated, and well described by a power-law relation, given the data. In addition, I also test with the full radial range ($1.0 \leq R < 30$ Mpc) and obtain the following best fit values for the mean cluster mass $M_0 = 2.79^{+0.24}_{-0.22} \times 10^{14}\,\mathrm{M}_\odot$, and for the richness scaling index, $F_\lambda = 0.98^{+0.20}_{-0.20}$. These values are in agreement with the estimates obtained with measurements in the inner region (at the 2σ uncertainty

limit). In addition in Figure 5.3, I compare the mass-richness relation with the stacked galaxy clusters in three richness groups. The results agree with each other, thus leading to the conclusion that our power-law assumption for the scaling relation is correct.

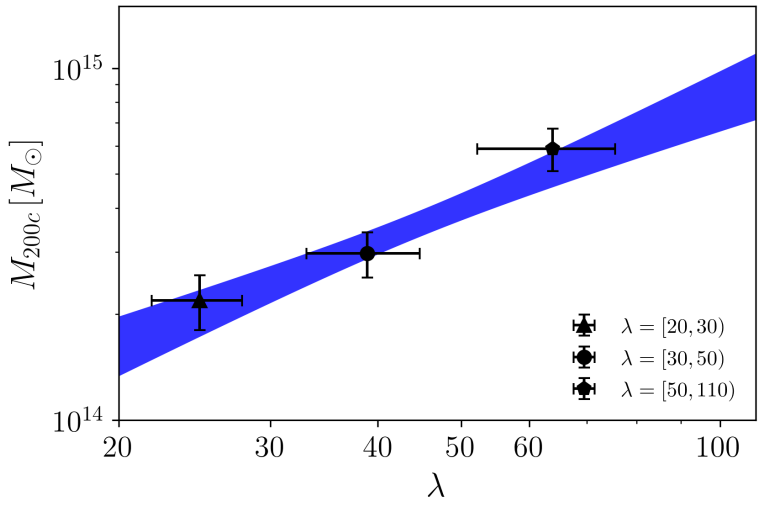

Figure 5.3. – The computed scaling relation of the CODEX clusters (blue shaded line) compared with measurements obtained with the stacked galaxy clusters in three richness groups.

5.3. Dynamical mass and weak lensing mass

As introduced in the first chapter, there are many ways to estimate the mass of galaxy clusters. In this work, I compare the weak lensing and dynamical masses in order to understand the physics of galaxy clusters. The dynamical analysis is based on the assumption that the cluster are in an equilibrium state. Then, the distribution of cluster member redshifts is related to the cluster mass. The comparisons between the weak lensing and dynamical masses will help to validate the equilibrium state assumption of the dynamical analysis. However, in this work, I can not extract the weak lensing mass of individual clusters, because of the limiting depth of the survey, and the limited number of background sources per cluster. Therefore, I compare the weak lensing and dynamical masses through the scaling relations derived with each respective method.

At the same time, I was doing my weak lensing analysis, Capasso, J. J. Mohr, Saro, et al. 2019 was performing a dynamical analysis with the same CODEX cluster sample. They use spectroscopy from the SPIDERS program to derive cluster dynamical masses. Assuming the clusters observed by the SPIDERS

program in spectroscopy produce a random subsample of the parent CODEX cluster sample used in our analysis, the scaling relations estimated with each technique can be compared. In their analysis, they measured the dynamical mass for a sample of 428 galaxy clusters up to redshift z $\sim$ 0.66. They model the scaling relation as $\lambda \propto A_\lambda \, M_{200c}^{B_\lambda} \, (1+z)^{\gamma_\lambda}$, and they find $A_\lambda = 38.6^{+3.1}_{-4.1}$, $B_\lambda = 0.99^{+0.06}_{-0.07}$ and $\gamma_\lambda = -1.13^{+0.32}_{-0.34}$. In Figure 5.4, I show both the weak-lensing and the dynamically-based mass-richness relations for the CODEX clusters. In both analysis, I set the mean cluster redshift to $\overline{z} = 0.15$. The width of the shaded areas corresponds to the 1σ confidence level. I find an excellent agreement between both mass-richness relations. Therefore, it suggests that the dynamical equilibrium state assumption associated with the dynamical mass measurement is suitable on average.

Moreover, I calculate the mass ratio ($\beta; M_{\rm dyn}/M_{\rm wl}$) between the dynamical masses ($M_{\rm dyn}$) and the weak lensing masses ($M_{\rm wl}$) (e.g. G. P. Smith, Mazzotta, N. Okabe, et al. 2016), using the results from the scaling relation performed by Capasso, J. J. Mohr, Saro, et al. 2019. I obtain a mass ratio $\beta = 0.99 \pm 0.03$, in statistical agreement with $\beta_X = 0.95 \pm 0.05$ estimated for the Local Cluster Substructure Survey (LoCuSS) at the redshift $0.15 < z < 0.3$ by G. P. Smith, Mazzotta, N. Okabe, et al. 2016.

5.3.1. Comparison with the redMaPPer clusters

The redMaPPer and CODEX cluster catalogs have different selection functions. Therefore, the clusters in each sample can have different properties. Here, I compare the scaling relation of the redMaPPer and CODEX cluster samples. I use the results from the DES Year 1 redMaPPer cluster sample analysis reported in T. McClintock, Varga, Gruen, et al. 2019. In this paper, they study the mass-richness relation for redMaPPer galaxy clusters in the redshift range $0.2 \leq z \leq 0.65$, and with richness values $\lambda \geq 20$. They obtain a richness scaling index $F_\lambda = 1.356 \pm 0.051$ (stat) and a redshift scaling index $G_z = -0.30 \pm 0.30$ (stat).

As described above, I find that the richness scaling index reported in T. McClintock, Varga, Gruen, et al. 2019 is smaller for the CODEX clusters than for the redMaPPer clusters. It suggests that, at low richness, CODEX clusters are more massive than redMaPPer clusters. I explain this difference by the higher purity of the CODEX clusters, which have been confirmed with X-ray observations or the CODEX clusters provide higher mass than the redMaPPer clusters at low richness.

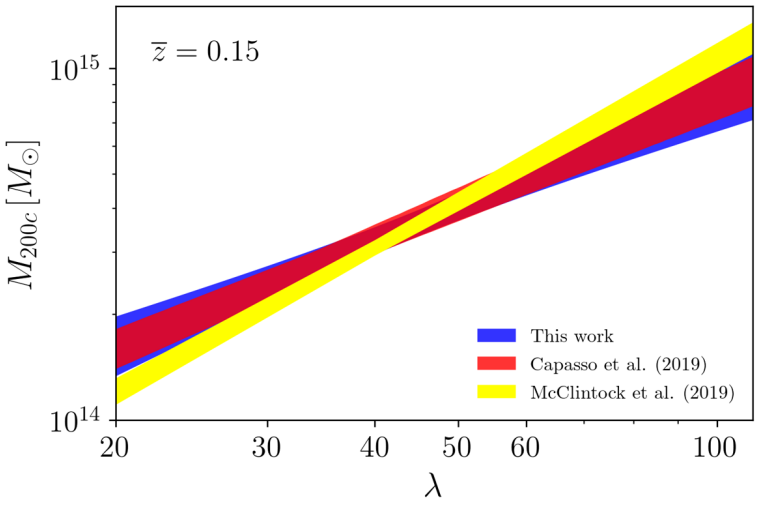

Figure 5.4. – The mass-richness relation of CODEX clusters estimated by the weak lensing and the dynamical analysis compared to the redMaPPer clusters from T. McClintock, Varga, Gruen, et al. 2019.

6. Conclusions

6.1. Conclusions and Summary of Results

In this section, I summarise how I performed the weak lensing analysis of the CODEX cluster sample using the data reduction by the DECaLS DR3. In the first chapter, I introduced an overview of the cosmological framework that I used in this work. I started from the current model of the universe, namely the ΛCDM model, discussed a solution of Einstein's field equations, and also the cosmological parameters that used to describe the evolution of the universe. I introduced galaxy clusters and discussed how they fit in the topic of the formation and evolution of the large scale structures of the Universe.

In Chapter 2, I introduced the basics of gravitational lensing. In particular, I focussed on the weak lensing regime and explained how the weak lensing signal can be extracted from the ellipticity measurement of background galaxies. I discussed how these observations can be used in order to measure the mass distribution of galaxy clusters, which is the main aim of this work. In addition, I exposed how the mass distribution of galaxy clusters can be described, presenting the NFW mass model. I described the theoretical profile consisting of two components: the first component distributed by the main dark matter halo of a galaxy clusters and the second component distributed by the sub halos near the galaxy cluster. For the measurement, I excluded the inner region at the radius $R < 1$ Mpc to avoid the miscentering effect and the low number density of background galaxies.

In Chapter 3, I discussed in detail the weak lensing analysis. There are many procedures in order to extract and enhance the weak lensing signal with the limitation of the photometry and density of the DECaLS DR3. The raw data from the observation was firstly performed with the Tractor tool by combining the three band filters together. This method is called the forced photometry that measured observed objects on the CCDs with the different models: PSF, SIMP, DEV, EXP, and COMP model. These objects are classified by the Tractor tool and measured the shape in each object by using the definition of ellipticity parameters.

To check the consistency of the shape measurement, I calibrated the ellipticity of the DECaLS DR3 shear catalog with the CFHT CS82 data and also compared them with the simulation. The results show the high uncertainty from the SIMP object in calibrating with the CFHT CS82. I therefore exclude this object for the DECaLS DR3 shear catalog. I have also measured the shear profile when I included and excluded SIMP objects in the analysis. The results show that the shear signal increases around 10 – 20 % when I excluded SIMP objects in the

measurement. Accordingly, SIMP objects are discarded for this analysis.

I computed the photometric redshifts for these galaxies which are estimated by the GAZPAR webservice. The results of the photometric redshift indicate a larger scatter at the high magnitude z which are useful objects for the weak lensing analysis because they are mostly background galaxies and affected by the weak gravitational lensing effect. I attempted to set the criteria by selecting the DECaLS DR3 objects, for instance, by cutting the DECaLS DR3 objects at the magnitude $magz > 21.0$ and I found that the shear profile is inaccurate and has higher fluctuation than the no removal case that might be from the low density of the weak lensing sources. Furthermore, I studied the color-color diagram for the DECaLS DR3 objects by matching them with the COSMOS 2015 and set the criteria to remove the foreground galaxies by the excessive blue or red galaxies. This method can not help to improve the shear signal because it removed the background galaxies and provided larger error bars from the measurements. Therefore, I used an alternative method to estimate the distance of the DECaLS objects by computing the photometric redshift distribution of the DECaLS DR3 shear catalog and estimating the effective critical surface mass density to measure the excess surface mass density profile. I used the probability distribution function estimated from the latest COSMOS photometric redshifts release (Laigle, McCracken, Ilbert, et al. 2016).

CODEX clusters used in this work have been selected on the DECaLS DR3 footprint. I removed the CODEX clusters at the redshift $z < 0.1$ to avoid the result of inaccurate redshift measurements which highlighted by Clerc, Merloni, Zhang, et al. 2016, and the higher redshift (ex., $z > 0.2$) due to the high contamination rate of foreground galaxies. The low optical richness is also removed due to the large scatter compared to the SDSS richness. The final sample for this analysis contains 279 CODEX clusters within the redshift ranges $0.1 \leq z \leq 0.2$ and the optical richness $20 \leq \lambda < 110$.

In Chapter 4, I discussed the stacking technique that I used to recover and enhance the weak lensing signal because of the low S/N in each cluster. The correction factor is also included in the measurement for correcting the amplitude of the mass profile. However, by testing with all CODEX cluster sample, I found that the correction factor is less than 1 % at the radius $R > 1$ Mpc, where I performed the weak lensing analysis.

There are many effects contributed to the statistical noises for the weak lensing measurement. I used Jackknife method to estimate the statistical errors or the covariance matrix of the stacked clusters. This method is a resampling technique to estimate variance and bias estimation from the resamples of the data itself. Moreover, I measured all CODEX cluster sample to find the mass-richness. In this case, the covariance matrix is estimated by the variation of the shear measurement in each radius bin. To find the best fitting parameters with the theoretical profile, I used the MCMC technique to find the posterior distribution function of the free parameters by setting the number of walkers, burn-in(s) and production samples

to 48, 1000 and 10000 which I can acquire a constant result value at the second decimal place with these setting conditions.

I presented my results in two parts in Chapter 5. For the first part, I divided the CODEX cluster samples into three richness groups; λ = 20 - 30, 30 - 50 and 50 - 110. In each group, I measured the tangential shear profile and computed the effective critical surface density in order to estimate the excess surface mass density, by separating the measurements into 12 bins within the radial ranges 1.0 $\leq R <$ 30.0 Mpc. Then, I fit the measured mass profile using a theoretical NFW profile to estimate the mean cluster mass in each bin. I found that the cluster mass is increasing with richness. However, there is high fluctuations at large radius, which might affect our measurement. I therefore re-measured the stacked clusters in each richness group by focusing on the inner region, 1.0 $\leq R <$ 5.5 Mpc (6 bins), using the first halo term only in the fit. The results for both regions are consistent within the 2σ confidence level and the cluster mass is increasing related to the mean optical richness in each group.

In the second part, I studied the scaling relations between cluster mass and richness. To do this, I fit all CODEX cluster sample together and modelled the mass-richness relation with a power-law by

$$\langle M_{200c}|\lambda\rangle = M_0 \left(\frac{\lambda}{\lambda_0}\right)^{F_\lambda} . \tag{6.1}$$

I restricted the measurement of the mass profile to the inner region ($1.0 \leq R < 5.5$ Mpc) due to the high fluctuation of the signal at the large scale radius. I obtained the mean cluster mass at the richness $\lambda = 40$,

$$M_0 = 3.24^{+0.29}_{-0.27} \times 10^{14}\,\mathrm{M}_\odot\,, \tag{6.2}$$

and the richness scaling index,

$$F_\lambda = 1.00^{+0.22}_{-0.22}\,. \tag{6.3}$$

I compared the results between the stacked clusters and scaling relations, and found that both analyses are in a good agreement with each other.

Finally, I compared my weak lensing analysis with the dynamical-based analysis obtained by Capasso, J. J. Mohr, Saro, et al. 2019. With the limitation of this analysis, I can only compare the results via the scaling relation. The results are in a good agreement between both methods which might suggest that the dynamical equilibrium assumption in galaxy clusters is suitable on average. In addition, I also compared the results of the mass-richness relation for the CODEX clusters with the redMaPPer clusters and found that the richness scaling index of the CODEX clusters is lower than the redMaPPer clusters. It might suggest that the CODEX clusters are more massive than the redMaPPer clusters, or the CODEX clusters are less contamination because they have the X-ray confirmation,

especially at the low richness.

6.2. Future works

In this section, I discuss the future works by separating them into two parts. Firstly, I would like to start with the DECaLS data which has few issues that we can be improved for the weak lensing analysis of massive galaxy clusters.

- Shape measurement: The DECaLS data is performed with the Tractor tool. Many sources are discarded because Tractor is not specific to shape measurement. I suggest the improvement of measurement and classification method of the DECaLS objects for the weak lensing analysis, for example, using the dedicated weak lensing tools to classify the objects. Moreover, we need to study the effect of the shape measurement because in this work the shapes of the DECaLS object are measured by combining with three-band filters which might be different from measuring them as an individual band filter. Moreover, galaxy ellipticity parameters of the DECaLS DR3 shear catalog have been calibrated by the CS82 data. Full-field simulations of the DECaLS surveys are needed to calibrate them.

- Photometric redshift: In this work, I computed the redshift distribution for the DECaLS DR3 Shear catalog instead of using the photometric redshift. However, the difference in the source distribution in each observed area can affect the cluster mass estimation. To use the photometric redshift for the mass measurement, I suggest improving the method to estimate them, for example, using machine learning, cutting the high magnitude (faint objects), or using the probability of the photometric redshift in each bin and objects to weight the measurement.

- High cluster redshift: I show that the contamination rate by foreground galaxies is rapidly increasing at the redshift 0.3 – 0.4 and prevent us to study the high cluster redshift. Therefore, we should find a method to exclude the foreground object. A better photometric redshift estimation is one of the methods that can help to remove the foreground object. Moreover, to build a better weak-lensing catalog, the advent of upcoming spectroscopic surveys and the high number of galaxy cluster catalog overlapping with the latest version of the DECaLS data should improve the weak lensing measurement.

Another part, I would like to discuss the future work which explains how I can connect this study with many important topics based on the upcoming data and instruments for the weak lensing analysis, for instance, the Euclid mission.

- Weak lensing and Dynamical analysis: The cross-study between both methods is very interesting in order to understand the physical properties and test the dynamic assumption in galaxy clusters with the same sample. In this work, with the limit from the data catalog, I can not cross-study the CODEX clusters with the same samples and the spectroscopic information in each galaxy cluster,

which are needed. The SPIDERS cluster catalog will be helpful for the future analysis because this catalog provide the spectroscopic data in an individual cluster. However, the high quality and in-depth imaging data for the weak lensing analysis are also needed.

- Theoretical mass profiles: If we have high accuracy in the mass measurement, we can test the various theoretical mass profiles, for example, Einasto profile, modified gravity and etc. Furthermore, we can also study the evolution of the NFW profile as the concentration-mass relation, and the halo mass-bias relation for the second dark matter halo.

- Cosmological study: The selection function is related to the cluster mass and cosmological parameters. We can use the relation between the mass-richness parameters, and the mass function of galaxy clusters to constrain the cosmological parameters such as the matter density and σ_8.

Bibliography

[ACO89] G. O. Abell, H. G. Corwin Jr., and R. P. Olowin. “A catalog of rich clusters of galaxies”. In: *ApJS* 70 (May 1989), pp. 1–138. DOI: 10.1086/191333 (cit. on p. 17).

[Abe58] George O. Abell. “The Distribution of Rich Clusters of Galaxies.” In: *ApJS* 3 (May 1958), p. 211. DOI: 10.1086/190036 (cit. on p. 17).

[Ber11] E. Bertin. “Automated Morphometry with SExtractor and PSFEx”. In: *Astronomical Data Analysis Software and Systems XX*. Ed. by I. N. Evans, A. Accomazzi, D. J. Mink, et al. Vol. 442. Astronomical Society of the Pacific Conference Series. July 2011, p. 435 (cit. on p. 41).

[Bla+17] M. R. Blanton, M. A. Bershady, B. Abolfathi, et al. “Sloan Digital Sky Survey IV: Mapping the Milky Way, Nearby Galaxies, and the Distant Universe”. In: *AJ* 154, 28 (July 2017), p. 28. DOI: 10.3847/1538-3881/aa7567. arXiv: 1703.00052 (cit. on pp. 54, 104).

[Cap+19] R. Capasso, J. J. Mohr, A. Saro, et al. “Mass Calibration of the CODEX Cluster Sample using SPIDERS Spectroscopy - I. The Richness-Mass Relation”. In: *MNRAS* (Mar. 2019), p. 901. DOI: 10.1093/mnras/stz931. arXiv: 1812.06094 [astro-ph.CO] (cit. on pp. 73, 74, 78, 106).

[Cib+17] N. Cibirka, E. S. Cypriano, F. Brimioulle, et al. “CODEX weak lensing: concentration of galaxy clusters at z = 0.5”. In: *MNRAS* 468 (June 2017), pp. 1092–1116. DOI: 10.1093/mnras/stx484. arXiv: 1612.06871 (cit. on pp. 39, 102).

[Cle+16] N. Clerc, A. Merloni, Y. -Y. Zhang, et al. “SPIDERS: the spectroscopic follow-up of X-ray selected clusters of galaxies in SDSS-IV”. In: *MNRAS* 463 (Dec. 2016), pp. 4490–4515. DOI: 10.1093/mnras/stw2214. arXiv: 1608.08963 [astro-ph.CO] (cit. on pp. 54, 55, 77, 104).

[Daw+16] K. S. Dawson, J.-P. Kneib, W. J. Percival, et al. “The SDSS-IV Extended Baryon Oscillation Spectroscopic Survey: Overview and Early Data”. In: *AJ* 151, 44 (Feb. 2016), p. 44. DOI: 10.3847/0004-6256/151/2/44. arXiv: 1508.04473 (cit. on pp. 54, 104).

[DT10] Antonio De Felice and Shinji Tsujikawa. “f(R) Theories”. In: *Living Reviews in Relativity* 13.1, 3 (June 2010), p. 3. DOI: 10.12942/lrr-2010-3. arXiv: 1002.4928 [gr-qc] (cit. on p. 19).

[DL17] Antonino Del Popolo and Morgan Le Delliou. “Small Scale Problems of the ΛCDM Model: A Short Review”. In: *Galaxies* 5.1 (Feb. 2017), p. 17. DOI: 10.3390/galaxies5010017. arXiv: 1606.07790 [astro-ph.CO] (cit. on p. 19).

[Dey+19] A. Dey, D. J. Schlegel, D. Lang, et al. “Overview of the DESI Legacy Imaging Surveys”. In: *AJ* 157, 168 (May 2019), p. 168. DOI: 10.3847/1538-3881/ab089d. arXiv: 1804.08657 [astro-ph.IM] (cit. on pp. 40, 41, 103).

[Duf+08] Alan R. Duffy, Joop Schaye, Scott T. Kay, et al. “Dark matter halo concentrations in the Wilkinson Microwave Anisotropy Probe year 5 cosmology”. In: *MNRAS* 390 (Oct. 2008), pp. L64–L68. DOI: 10.1111/j.1745-3933.2008.00537.x. arXiv: 0804.2486 [Astrophysics] (cit. on pp. 39, 67).

[DM14] A. A. Dutton and A. V. Macciò. “Cold dark matter haloes in the Planck era: evolution of structural parameters for Einasto and NFW profiles”. In: *MNRAS* 441 (July 2014), pp. 3359–3374. DOI: 10.1093/mnras/stu742. arXiv: 1402.7073 (cit. on pp. 39, 102).

[DED20] F. W. Dyson, A. S. Eddington, and C. Davidson. “A Determination of the Deflection of Light by the Sun’s Gravitational Field, from Observations Made at the Total Eclipse of May 29, 1919”. In: *Philosophical Transactions of the Royal Society of London Series A* 220 (1920), pp. 291–333. DOI: 10.1098/rsta.1920.0009 (cit. on p. 25).

[Eth33] I. M. H. Etherington. “LX. On the definition of distance in general relativity”. In: *Philosophical Magazine* 15.100 (1933), pp. 761–773 (cit. on p. 24).

[Ett+13] Stefano Ettori, Annamaria Donnarumma, Etienne Pointecouteau, et al. “Mass Profiles of Galaxy Clusters from X-ray Analysis”. In: *Space Sci. Rev.* 177.1-4 (Aug. 2013), pp. 119–154. DOI: 10.1007/s11214-013-9976-7. arXiv: 1303.3530 [astro-ph.CO] (cit. on p. 17).

[Euc+19] Euclid Collaboration, N. Martinet, T. Schrabback, et al. “Euclid Preparation IV. Impact of undetected galaxies on weak lensing shear measurements”. In: *arXiv e-prints*, arXiv:1902.00044 (Jan. 2019), arXiv:1902.00044. arXiv: 1902.00044 [astro-ph.CO] (cit. on p. 42).

[Fel+66] J. E. Felten, R. J. Gould, W. A. Stein, et al. “X-Rays from the Coma Cluster of Galaxies”. In: *ApJ* 146 (Dec. 1966), pp. 955–958. DOI: 10.1086/148972 (cit. on p. 17).

[Fis+00] P. Fischer, T. A. McKay, E. Sheldon, et al. "Weak Lensing with Sloan Digital Sky Survey Commissioning Data: The Galaxy-Mass Correlation Function to 1 H^{-1} Mpc". In: *AJ* 120 (Sept. 2000), pp. 1198–1208. DOI: 10.1086/301540. eprint: astro-ph/9912119 (cit. on p. 59).

[For+13] Daniel Foreman-Mackey, David W. Hogg, Dustin Lang, et al. "emcee: The MCMC Hammer". In: *Publications of the Astronomical Society of the Pacific* 125 (Mar. 2013), p. 306. DOI: 10.1086/670067. arXiv: 1202.3665 [astro-ph.IM] (cit. on p. 64).

[Fri+71] Gilbert Fritz, Arthur Davidsen, John F. Meekins, et al. "Discovery of an X-Ray Source in Perseus". In: *ApJ* 164 (Mar. 1971), p. L81. DOI: 10.1086/180697 (cit. on p. 17).

[Geo+12] Matthew R. George, Alexie Leauthaud, Kevin Bundy, et al. "Galaxies in X-Ray Groups. II. A Weak Lensing Study of Halo Centering". In: *ApJ* 757.1, 2 (Sept. 2012), p. 2. DOI: 10.1088/0004-637X/757/1/2. arXiv: 1205.4262 [astro-ph.CO] (cit. on p. 38).

[HSS07] J. Hartlap, P. Simon, and P. Schneider. "Why your model parameter confidences might be too optimistic. Unbiased estimation of the inverse covariance matrix". In: *Astronomy and Astrophysics* 464.1 (Mar. 2007), pp. 399–404. DOI: 10.1051/0004-6361:20066170. arXiv: astro-ph/0608064 [astro-ph] (cit. on p. 62).

[Hey+12] Catherine Heymans, Ludovic Van Waerbeke, Lance Miller, et al. "CFHTLenS: the Canada-France-Hawaii Telescope Lensing Survey". In: *MNRAS* 427 (Nov. 2012), pp. 146–166. DOI: 10.1111/j.1365-2966.2012.21952.x. arXiv: 1210.0032 [astro-ph.CO] (cit. on p. 42).

[Hog99] David W. Hogg. "Distance measures in cosmology". In: *arXiv e-prints*, astro-ph/9905116 (May 1999), astro–ph/9905116. arXiv: astro-ph/9905116 [astro-ph] (cit. on p. 22).

[Hub29] E. Hubble. "A Relation between Distance and Radial Velocity among Extra-Galactic Nebulae". In: *Proceedings of the National Academy of Science* 15 (Mar. 1929), pp. 168–173. DOI: 10.1073/pnas.15.3.168 (cit. on p. 13).

[Kle+18] Matthias Klein, Sebastian Grandis, Joseph Mohr, et al. "A New RASS Galaxy Cluster Catalog with Low Contamination Extending to $z = 1$ in the DES Overlap Region". In: *arXiv e-prints*, arXiv:1812.09956 (Dec. 2018), arXiv:1812.09956. arXiv: 1812.09956 [astro-ph.CO] (cit. on pp. 54, 104).

[Lai+16] C. Laigle, H. J. McCracken, O. Ilbert, et al. “The COSMOS2015 Catalog: Exploring the 1 < z < 6 Universe with Half a Million Galaxies”. In: *The Astrophysical Journal Supplement Series* 224, 24 (June 2016), p. 24. DOI: 10.3847/0067-0049/224/2/24. arXiv: 1604.02350 [astro-ph.GA] (cit. on p. 77).

[LHS14] Dustin Lang, David W. Hogg, and David J. Schlegel. “WISE photometry for 400 million SDSS sources”. In: *arXiv e-prints*, arXiv:1410.7397 (Oct. 2014), arXiv:1410.7397. arXiv: 1410.7397 [astro-ph.IM] (cit. on p. 41).

[Lem27] G. Lemaître. “Un Univers homogène de masse constante et de rayon croissant rendant compte de la vitesse radiale des nébuleuses extra-galactiques”. In: *Annales de la Société Scientifique de Bruxelles* 47 (1927), pp. 49–59 (cit. on p. 13).

[LC11] A. Lewis and A. Challinor. *CAMB: Code for Anisotropies in the Microwave Background*. Astrophysics Source Code Library. Feb. 2011. ascl: 1102.026 (cit. on p. 37).

[Liu+15] Xiangkun Liu, Chuzhong Pan, Ran Li, et al. “Cosmological constraints from weak lensing peak statistics with Canada-France-Hawaii Telescope Stripe 82 Survey”. In: *MNRAS* 450 (July 2015), pp. 2888–2902. DOI: 10.1093/mnras/stv784. arXiv: 1412.3683 [astro-ph.CO] (cit. on pp. 42, 103).

[LP86] R. Lynds and V. Petrosian. “Giant Luminous Arcs in Galaxy Clusters”. In: *BAAS*. Vol. 18. Sept. 1986, p. 1014 (cit. on p. 26).

[Man+16] Nazzareno Mandolesi, Diego Molinari, Alessandro Gruppuso, et al. “The Planck legacy - Reinforcing the case for a standard model of cosmology: ΛCDM”. In: *arXiv e-prints*, arXiv:1605.01533 (May 2016), arXiv:1605.01533. arXiv: 1605.01533 [astro-ph.CO] (cit. on p. 13).

[McC+19] T. McClintock, T. N. Varga, D. Gruen, et al. “Dark Energy Survey Year 1 results: weak lensing mass calibration of redMaPPer galaxy clusters”. In: *MNRAS* 482 (Jan. 2019), pp. 1352–1378. DOI: 10.1093/mnras/sty2711. arXiv: 1805.00039 [astro-ph.CO] (cit. on pp. 38, 51, 74, 75).

[Mer+06] D. Merritt, A. W. Graham, B. Moore, et al. “Empirical Models for Dark Matter Halos. I. Nonparametric Construction of Density Profiles and Comparison with Parametric Models”. In: *AJ* 132 (Dec. 2006), pp. 2685–2700. DOI: 10.1086/508988. eprint: astro-ph/0509417 (cit. on p. 34).

[Mil+13] L. Miller, C. Heymans, T. D. Kitching, et al. “Bayesian galaxy shape measurement for weak lensing surveys - III. Application to the Canada-France-Hawaii Telescope Lensing Survey”. In: *MNRAS* 429 (Mar. 2013), pp. 2858–2880. DOI: 10.1093/mnras/sts454. arXiv: 1210.8201 [astro-ph.CO] (cit. on p. 42).

[Mor+12] Andrea Morandi, Marceau Limousin, Jack Sayers, et al. “X-ray, lensing and Sunyaev-Zel’dovich triaxial analysis of Abell 1835 out to R_{200}”. In: *MNRAS* 425 (Sept. 2012), pp. 2069–2082. DOI: 10.1111/j.1365-2966.2012.21196.x. arXiv: 1111.6189 [astro-ph.CO] (cit. on p. 16).

[NB96] Ramesh Narayan and Matthias Bartelmann. “Lectures on Gravitational Lensing”. In: *arXiv e-prints*, astro-ph/9606001 (June 1996), astro–ph/9606001. arXiv: astro-ph/9606001 [astro-ph] (cit. on p. 33).

[NFW97] J. F. Navarro, C. S. Frenk, and S. D. M. White. “A Universal Density Profile from Hierarchical Clustering”. In: *ApJ* 490 (Dec. 1997), pp. 493–508. DOI: 10.1086/304888. eprint: astro-ph/9611107 (cit. on pp. 34, 101).

[Ogu+12] Masamune Oguri, Matthew B. Bayliss, Hâkon Dahle, et al. “Combined strong and weak lensing analysis of 28 clusters from the Sloan Giant Arcs Survey”. In: *MNRAS* 420.4 (Mar. 2012), pp. 3213–3239. DOI: 10.1111/j.1365-2966.2011.20248.x. arXiv: 1109.2594 [astro-ph.CO] (cit. on p. 49).

[Oka+10] N. Okabe, M. Takada, K. Umetsu, et al. “LoCuSS: Subaru Weak Lensing Study of 30 Galaxy Clusters”. In: *PASJ* 62 (June 2010), pp. 811–870. DOI: 10.1093/pasj/62.3.811. arXiv: 0903.1103 (cit. on pp. 39, 102).

[Oka+14] Nobuhiro Okabe, Toshifumi Futamase, Masaru Kajisawa, et al. “Subaru Weak-lensing Survey of Dark Matter Subhalos in the Coma Cluster: Subhalo Mass Function and Statistical Properties”. In: *ApJ* 784, 90 (Apr. 2014), p. 90. DOI: 10.1088/0004-637X/784/2/90. arXiv: 1304.2399 [astro-ph.CO] (cit. on p. 51).

[Pla+16a] Planck Collaboration, P. A. R. Ade, N. Aghanim, et al. “Planck 2015 results. XIII. Cosmological parameters”. In: *A&A* 594, A13 (Sept. 2016), A13. DOI: 10.1051/0004-6361/201525830 (cit. on pp. 12, 13).

[Pla+16b] Planck Collaboration, P. A. R. Ade, N. Aghanim, et al. “Planck 2015 results. XXIV. Cosmology from Sunyaev-Zeldovich cluster counts”. In: *A&A* 594, A24 (Sept. 2016), A24. DOI: 10.1051/0004-6361/201525833. arXiv: 1502.01597 [astro-ph.CO] (cit. on p. 16).

[Ras+12] E. Rasia, M. Meneghetti, R. Martino, et al. “Lensing and x-ray mass estimates of clusters (simulations)”. In: *New Journal of Physics* 14.5, 055018 (May 2012), p. 055018. DOI: 10.1088/1367-2630/14/5/055018. arXiv: 1201.1569 [astro-ph.CO] (cit. on p. 17).

[Roz+15] E. Rozo, E. S. Rykoff, M. Becker, et al. “redMaPPer – IV. Photometric membership identification of red cluster galaxies with 1 percent precision”. In: *MNRAS* 453.1 (Aug. 2015), pp. 38–52. ISSN: 0035-8711. DOI: 10.1093/mnras/stv1560. eprint: http://oup.prod.sis.lan/mnras/article-pdf/453/1/38/4910636/stv1560.pdf. URL: https://doi.org/10.1093/mnras/stv1560 (cit. on p. 59).

[Ryk+14] E. S. Rykoff, E. Rozo, M. T. Busha, et al. “redMaPPer. I. Algorithm and SDSS DR8 Catalog”. In: *ApJ* 785, 104 (Apr. 2014), p. 104. DOI: 10.1088/0004-637X/785/2/104. arXiv: 1303.3562 [astro-ph.CO] (cit. on pp. 17, 54, 59, 104).

[Sha+14] Huan Yuan Shan, Jean-Paul Kneib, Johan Comparat, et al. “Weak lensing mass map and peak statistics in Canada-France-Hawaii Telescope Stripe 82 survey”. In: *MNRAS* 442 (Aug. 2014), pp. 2534–2542. DOI: 10.1093/mnras/stu1040. arXiv: 1311.1319 [astro-ph.CO] (cit. on pp. 42, 103).

[Shi+17] Masato Shirasaki, Masahiro Takada, Hironao Miyatake, et al. “Robust covariance estimation of galaxy-galaxy weak lensing: validation and limitation of jackknife covariance”. In: *MNRAS* 470 (Sept. 2017), pp. 3476–3496. DOI: 10.1093/mnras/stx1477. arXiv: 1607.08679 [astro-ph.CO] (cit. on p. 61).

[Sim+17] Melanie Simet, Tom McClintock, Rachel Mandelbaum, et al. “Weak lensing measurement of the mass-richness relation of SDSS redMaPPer clusters”. In: *MNRAS* 466 (Apr. 2017), pp. 3103–3118. DOI: 10.1093/mnras/stw3250. arXiv: 1603.06953 [astro-ph.CO] (cit. on p. 59).

[Smi+16] G. P. Smith, P. Mazzotta, N. Okabe, et al. “LoCuSS: Testing hydrostatic equilibrium in galaxy clusters”. In: *MNRAS* 456 (Feb. 2016), pp. L74–L78. DOI: 10.1093/mnrasl/slv175. arXiv: 1511.01919 [astro-ph.CO] (cit. on p. 74).

[Smi+03] R. E. Smith, J. A. Peacock, A. Jenkins, et al. “Stable clustering, the halo model and non-linear cosmological power spectra”. In: *MNRAS* 341.4 (June 2003), pp. 1311–1332. DOI: 10.1046/j.1365-8711.2003.06503.x. arXiv: astro-ph/0207664 [astro-ph] (cit. on p. 90).

[Sol04] J Soldner. “Ueber die Ablenkung eines Lichtstrals von seiner geradlinigen Bewegung”. In: *Berliner Astronomisches Jahrbuch* (1804), pp. 161–172 (cit. on p. 25).

[Sou+88] G. Soucail, Y. Mellier, B. Fort, et al. “The giant arc in A 370 : spectroscopic evidence for gravitational lensing from a source at Z=0.724.” In: *A&A* 191 (Feb. 1988), pp. L19–L21 (cit. on p. 26).

[Tak+12] Ryuichi Takahashi, Masanori Sato, Takahiro Nishimichi, et al. “Revising the Halofit Model for the Nonlinear Matter Power Spectrum”. In: *ApJ* 761, 152 (Dec. 2012), p. 152. DOI: 10.1088/0004-637X/761/2/152. arXiv: 1208.2701 [astro-ph.CO] (cit. on pp. 37, 90, 91).

[Tin+10] Jeremy L. Tinker, Brant E. Robertson, Andrey V. Kravtsov, et al. “The Large-scale Bias of Dark Matter Halos: Numerical Calibration and Model Tests”. In: *ApJ* 724 (Dec. 2010), pp. 878–886. DOI: 10.1088/0004-637X/724/2/878. arXiv: 1001.3162 [astro-ph.CO] (cit. on pp. 37, 67, 89).

[Tin+05] Jeremy L. Tinker, David H. Weinberg, Zheng Zheng, et al. “On the Mass-to-Light Ratio of Large-Scale Structure”. In: *ApJ* 631 (Sept. 2005), pp. 41–58. DOI: 10.1086/432084. arXiv: astro-ph/0411777 [astro-ph] (cit. on p. 37).

[Ume10] Keiichi Umetsu. “Cluster Weak Gravitational Lensing”. In: *arXiv e-prints*, arXiv:1002.3952 (Feb. 2010), arXiv:1002.3952. arXiv: 1002.3952 [astro-ph.CO] (cit. on p. 30).

[Vog+99] W. Voges, B. Aschenbach, T. Boller, et al. “The ROSAT all-sky survey bright source catalogue”. In: *A&A* 349 (Sept. 1999), pp. 389–405. eprint: astro-ph/9909315 (cit. on pp. 54, 104).

[Wey+79] R. J. Weymann, F. H. Chaffee Jr., N. P. Carleton, et al. “Multiple-mirror telescope observations of the twin QSOs 0957+561 A, B”. In: *ApJ* 233 (Oct. 1979), pp. L43–L46. DOI: 10.1086/183073 (cit. on p. 25).

[Yan+06] X. Yang, H. J. Mo, F. C. van den Bosch, et al. “Weak lensing by galaxies in groups and clusters - I. Theoretical expectations”. In: *MNRAS* 373 (Dec. 2006), pp. 1159–1172. DOI: 10.1111/j.1365-2966.2006.11091.x. eprint: astro-ph/0607552 (cit. on p. 38).

[Zwi37] F. Zwicky. “On the Masses of Nebulae and of Clusters of Nebulae”. In: *ApJ* 86 (Oct. 1937), p. 217. DOI: 10.1086/143864 (cit. on p. 25).

APPENDIX

A. Halo bias

There are some biases in tracing the underlying matter distribution of the large-scale structures like a galaxy cluster. In this work, I re-scale the second dark matter halo by using the halo bias from Tinker, Robertson, Kravtsov, et al. 2010. In this paper, the authors calibrated the fitting functions for the large-scale bias with cosmological simulations of the flat ΛCDM model. Let's consider the dark matter halos in the large-scale structures, I can define the bias in tracing the dark matter halos by

$$b^2(k) = \frac{P_{\rm h}(k)}{P_{\rm lin}(k)}\,, \tag{.1}$$

where $P_{\rm h}(k)$ is the halo spectrum and $P_{\rm lin}(k)$ is the linear matter power spectrum. Tinker, Robertson, Kravtsov, et al. 2010 rewrite the fitting function in the form,

$$b(\nu) = 1 - A\frac{\nu_a}{\nu_a + \delta_c^a} + B\nu^b + C\nu^c \tag{.2}$$

where A, a, B, b, C and c are the best-fit parameters as described in Table 2 in Tinker, Robertson, Kravtsov, et al. 2010, and $\nu = \delta_c/\sigma(M)$; where $\delta_c = 1.686$ is the critical density for collapse and $\sigma(M)$ is the linear matter variance. The mass fluctuations of a sphere of radius R is given by

$$\sigma^2(R) = \frac{1}{2\pi^2}\int P_{\rm lin}(k,z)\hat{W}^2(k,R)k^2dk\,, \tag{.3}$$

where $P_{\rm lin}(k,z)$ is the linear power spectrum at redshift z and $\hat{W}^2(k,R)$ is the top-hat function. Figure .1 shows the large-scale bias of the dark matter halos from Tinker, Robertson, Kravtsov, et al. 2010.

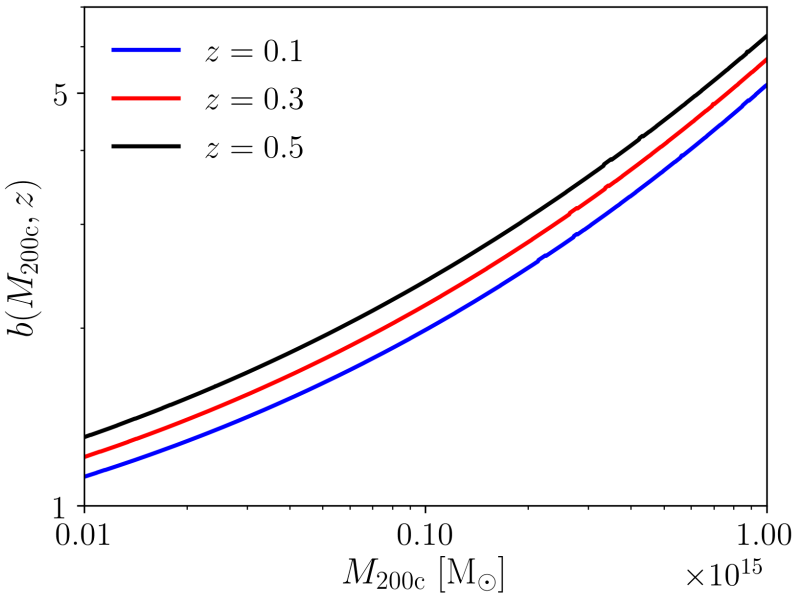

Figure .1. – Large-scale bias of the dark matter halos with the mass ranging between 10^{13} and $10^{15} M_\odot$ for the redshift $z = 0.1$, 0.3 and 0.5.

B. Non-Linear Matter Power Spectrum

As I described in Section 2.6.2, the second dark matter halo term ($\Delta\Sigma_{2h}$) is computed by using the non-linear matter power spectrum. In this section, I explain the functional form of the revised halofit model for the non-linear power spectrum by Takahashi, Sato, Nishimichi, et al. 2012, which revisited the halo fitting formula or the halofit model of R. E. Smith, Peacock, Jenkins, et al. 2003. It has been used in this analysis and also with the Code for Anisotropies in the Microwave Background (CAMB) program. The non-linear power spectrum (P_{nl}) is given by

$$P_{nl}(k) = \frac{(2\pi)^2}{k^3}\Delta^2_{nl}(k) \tag{.4}$$

where Δ^2_{nl} is the non-linear term which can be written as the summation of two terms,

$$\Delta^2_{nl}(k) = \Delta^2_{Q}(k) + \Delta^2_{H}(k)\,. \tag{.5}$$

The first term, $\Delta^2_{Q}(k)$, is given by

$$\Delta^2_{Q}(k) = \Delta^2_{L}(k)\left[\frac{1+\Delta^2_{L}(k)^{\beta_n}}{1+\alpha_n\Delta^2_{L}(k)}\right]e^{-f(y)}\,, \tag{.6}$$

where $y \equiv k/k_\sigma$ is the dimensionless parameter, $f(y) = (y/4) + (y^2/8)$, $\Delta^2_{\rm L} = k^3 P_{\rm lin}(k)/(2\pi)^2$, and $P_{\rm lin}(k)$ is the linear power spectrum. The second term, $\Delta^2_{\rm H}(k)$, is given by

$$\Delta^2_{\rm H}(k) = \frac{\Delta^{2\prime}_{\rm H}(k)}{1 + \mu_n y^{-1} + \nu_n y^{-2}}\,, \tag{.7}$$

with

$$\Delta^{2\prime}_{\rm H}(k) = \frac{a_n y^{3f_1(\Omega)}}{1 + b_n y^{f_2(\Omega)} + [c_n f_3(\Omega) y]^{3-\gamma_n}}\,. \tag{.8}$$

where $f_1(\Omega) = \Omega^{-0.0307}$, $f_2(\Omega) = \Omega^{-0.0585}$, $f_3(\Omega) = \Omega^{0.0743}$, and Ω is the matter density parameter at the redshift z. The parameters $a_n, b_n, c_n, \gamma_n, \alpha_n, \beta_n, \mu_n$, and ν vary as a function of spectral properties, for example, the best-fit parameters are in Equation (A6) - (A13) in Takahashi, Sato, Nishimichi, et al. 2012. Figure .2 shows the non-linear power spectrum prescribed by Takahashi, Sato, Nishimichi, et al. 2012 from the CAMB program

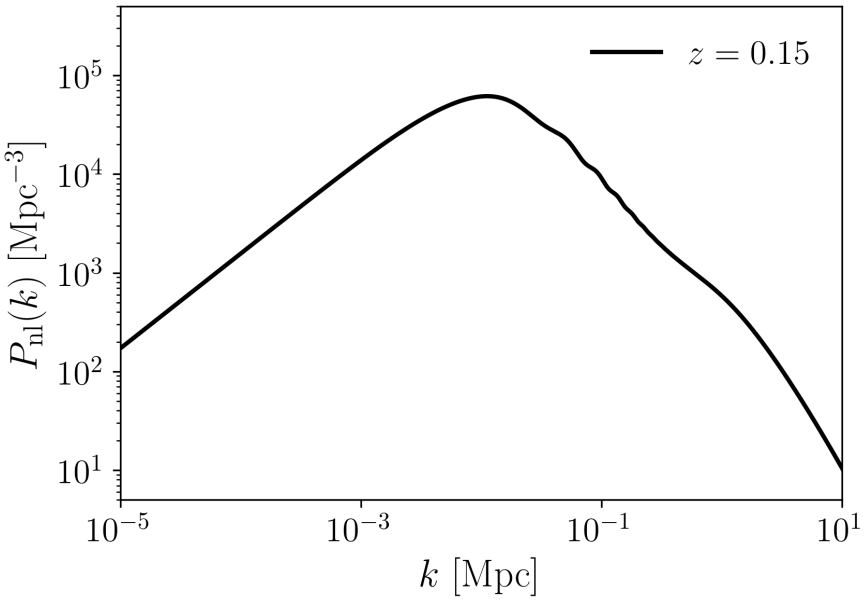

Figure .2. – The non-linear power spectrum prescribed by Takahashi, Sato, Nishimichi, et al. 2012 from the CAMB program at the redshift z = 0.15

C. CODEX cluster sample

A summary of the CODEX cluster sample information is given in Table .1 - .7.

Table .1. – Summary of the CODEX cluster samples.

ID	RA_{OPT}	DEC_{OPT}	λ_{OPT}	$z_{cluster}$
1	39.9036	-4.1339	20.0798	0.1383
2	166.3627	7.6433	20.0798	0.1664
3	182.6416	-0.4125	20.2171	0.1769
4	318.5008	8.3482	20.2171	0.1339
5	29.8784	-0.1047	20.3849	0.1585
6	250.1903	19.5492	20.4916	0.1908
7	334.2296	17.5495	20.5527	0.1772
8	9.7797	18.4956	20.6137	0.1355
9	144.9787	12.4631	20.6900	0.1785
10	138.7929	5.2346	20.7052	0.1309
11	328.5979	0.0844	20.7357	0.1611
12	136.3506	23.5579	20.9493	0.1683
13	344.1178	-0.5483	20.9645	0.1093
14	145.8733	0.0568	21.0103	0.1358
15	229.0662	2.5089	21.0256	0.1298
16	117.6935	14.7546	21.0561	0.1007
17	32.7621	-4.8939	21.0713	0.1345
18	242.1722	6.9087	21.1781	0.1643
19	24.2189	-6.4480	21.2391	0.1124
20	212.4978	-1.5397	21.2849	0.1043
21	25.5356	-6.6954	21.3307	0.1183
22	136.1682	19.2965	21.4222	0.1019
23	22.1551	-6.7693	21.4832	0.1823
24	15.3281	0.5974	21.5137	0.1849
25	250.0535	21.5603	21.5747	0.1597
26	180.1863	-0.1562	21.7578	0.1677
27	38.7999	-1.5132	21.8036	0.1676
28	23.1965	1.2627	21.9104	0.1280
29	29.6950	-0.6947	22.3833	0.1872
30	155.7676	-1.9480	22.3985	0.1272

Table .2. – Summary of the CODEX cluster samples.

ID	RA_{OPT}	DEC_{OPT}	λ_{OPT}	$z_{cluster}$
31	322.2536	6.2570	22.3985	0.1014
32	36.3012	-6.3832	22.5816	0.1959
33	138.5135	1.6451	22.6579	0.1646
34	135.2770	7.7963	22.9629	0.1534
35	246.8251	29.6583	22.9935	0.1698
36	148.5424	-1.1946	23.0545	0.1418
37	186.2092	-0.3169	23.1765	0.1614
38	170.5226	0.7843	23.2986	0.1081
39	151.7232	12.3935	23.3138	0.1716
40	258.5046	29.8081	23.3291	0.1989
41	191.0271	17.8088	23.4816	0.1667
42	136.3825	17.9479	23.5274	0.1328
43	173.1511	19.8349	23.6952	0.1522
44	143.7086	19.4442	23.9393	0.1875
45	179.0836	-0.2055	23.9850	0.1078
46	199.5981	-0.5295	24.0461	0.1116
47	0.8253	4.6276	24.1071	0.1034
48	254.8301	28.8830	24.1528	0.1474
49	160.9051	0.6126	24.1681	0.1188
50	213.9535	0.2604	24.2901	0.1233
51	119.8542	27.1302	24.3969	0.1004
52	11.6008	0.0024	24.4884	0.1220
53	126.1339	20.4573	24.7020	0.1123
54	202.1432	-1.3258	24.7173	0.1350
55	234.2644	14.7605	24.7630	0.1004
56	349.5909	18.1916	24.8546	0.1795
57	351.1756	15.8200	24.9461	0.1512
58	11.8711	18.9725	24.9919	0.1693
59	30.5437	-3.1875	25.1597	0.1615
60	3.2171	-6.1210	25.2817	0.1987
61	115.3895	25.9531	25.2817	0.1627
62	223.7596	4.2520	25.3122	0.1262
63	125.2636	7.9270	25.4495	0.1115
64	35.8676	-8.8654	25.5105	0.1670
65	16.2439	-2.7006	25.6783	0.1917
66	324.6290	2.2004	25.7699	0.1812
67	227.4975	3.0031	25.8156	0.1054
68	161.4521	4.3424	26.1817	0.1503
69	319.3287	7.4135	26.2275	0.1365
70	129.8100	8.3786	26.3648	0.1379
71	134.8065	3.2675	26.4106	0.1829
72	149.5514	23.7793	26.4868	0.1545

Table .3. – Summary of the CODEX cluster samples. (cont.)

ID	RA_{OPT}	DEC_{OPT}	λ_{OPT}	$z_{cluster}$
73	229.0057	2.0168	26.5631	0.1029
74	14.2418	-6.9974	26.6852	0.1815
75	165.3395	7.0741	26.8682	0.1611
76	153.3816	24.8353	27.0055	0.1927
77	167.1369	25.7769	27.2496	0.1951
78	206.3203	-1.9405	27.2954	0.1540
79	11.4576	-0.8504	27.3564	0.1057
80	29.2265	-4.4071	27.4479	0.1378
81	126.3047	0.0876	27.4479	0.1503
82	123.8429	22.7293	27.5242	0.1025
83	125.6076	29.1915	27.7683	0.1714
84	222.0766	3.5290	27.9056	0.1205
85	152.2696	14.0250	27.9361	0.1732
86	259.9828	26.3942	27.9971	0.1636
87	338.3199	16.5833	28.0581	0.1344
88	318.4745	-2.3894	28.0886	0.1706
89	167.7675	1.0904	28.1954	0.1017
90	229.1578	14.1159	28.2107	0.1755
91	167.0519	26.1761	28.3632	0.1819
92	182.4779	-0.5577	28.4547	0.1809
93	149.1169	18.5174	28.5615	0.1573
94	350.4461	15.0833	28.5615	0.1530
95	241.5574	20.1350	28.5920	0.1776
96	163.1793	20.1979	28.6836	0.1586
97	28.3730	-4.3608	28.7293	0.1359
98	150.9833	-2.0846	28.7598	0.1005
99	213.8083	-1.6177	28.8209	0.1518
100	144.7610	14.2316	29.0344	0.1336
101	245.9064	21.7403	29.0344	0.1617
102	118.4358	26.4977	29.0802	0.1954
103	213.7190	0.1962	29.0802	0.1240
104	246.2947	28.4957	29.1412	0.1512
105	164.2768	-2.2167	29.4311	0.1836
106	150.2775	10.4352	29.4463	0.1690
107	146.5499	2.3688	29.4921	0.1300
108	141.6776	17.6863	29.7362	0.1152
109	7.2312	17.7368	29.9955	0.1064
110	339.6178	15.7520	30.5142	0.1316
111	133.6525	0.6426	30.5599	0.1163
112	157.1089	9.6222	30.6362	0.1185
113	18.0169	-0.7311	30.6667	0.1824
114	246.9074	22.8159	30.6667	0.1979

Table .4. – Summary of the CODEX cluster samples. (cont.)

ID	RA_{OPT}	DEC_{OPT}	λ_{OPT}	$z_{cluster}$
115	251.9426	29.1693	30.6667	0.1362
116	151.3672	22.7830	30.7430	0.1886
117	190.5732	19.7667	30.8650	0.1676
118	251.9335	29.9420	31.0328	0.1047
119	197.4564	19.6467	31.2769	0.1429
120	259.3867	25.8515	31.4142	0.1867
121	36.3337	-8.7226	31.5362	0.1062
122	33.4072	-2.8997	31.7041	0.1546
123	141.4538	7.7515	32.2532	0.1298
124	158.5659	15.8955	32.2532	0.1839
125	206.0967	11.6491	32.2532	0.1034
126	217.9587	13.5347	32.2837	0.1607
127	261.5236	27.2796	32.3142	0.1048
128	160.9665	1.0617	32.5888	0.1087
129	148.7805	9.5878	32.7261	0.1396
130	8.9613	18.6542	32.9092	0.1443
131	21.0768	4.4597	32.9244	0.1268
132	121.6039	17.4177	33.1380	0.1125
133	132.5320	29.5491	33.1838	0.1019
134	28.7482	-6.2612	33.4279	0.1168
135	185.3848	0.2162	33.4889	0.1666
136	112.3659	24.6066	33.5194	0.1729
137	328.8743	8.7934	33.9770	0.1569
138	140.2195	11.4668	34.0686	0.1609
139	42.4068	-2.5190	34.0991	0.1992
140	36.4372	-3.2092	34.1754	0.1413
141	138.0637	-2.2942	34.2364	0.1557
142	33.4738	-1.5406	34.2821	0.1699
143	153.7195	21.8172	34.2974	0.1586
144	203.2440	19.9377	34.6635	0.1676
145	171.5068	25.4886	34.6940	0.1150
146	350.8364	6.5003	34.7398	0.1281
147	172.1050	23.8842	34.9381	0.1338
148	213.2407	14.7342	34.9991	0.1358
149	323.9429	0.1159	35.0144	0.1213
150	129.2310	2.9820	35.4110	0.1918
151	186.6870	-0.6216	35.5636	0.1621
152	15.6795	1.1363	36.0517	0.1386
153	177.5850	-0.5931	36.2958	0.1364
154	2.3613	3.9893	36.6924	0.1057
155	250.1569	27.9247	36.8755	0.1381
156	248.8394	20.3648	37.0738	0.1558

Table .5. – Summary of the CODEX cluster samples. (cont.)

ID	RA_{OPT}	DEC_{OPT}	λ_{OPT}	$z_{cluster}$
157	9.4786	18.3488	37.1196	0.1428
158	260.7931	26.8934	37.2569	0.1154
159	41.2557	-3.0982	37.4247	0.1616
160	30.4296	-2.1967	37.5162	0.1955
161	118.5606	12.8631	37.9433	0.1853
162	175.6329	25.4675	37.9433	0.1914
163	151.6674	21.6707	38.0196	0.1901
164	158.7023	4.4055	38.1264	0.1678
165	208.3774	6.9453	38.3400	0.1515
166	147.7220	28.8043	38.3552	0.1133
167	213.1012	21.2477	38.4315	0.1505
168	142.5001	11.3359	38.4925	0.1819
169	151.4612	10.9699	38.5230	0.1668
170	250.9525	17.2637	38.5688	0.1621
171	137.1036	6.0657	38.5993	0.1560
172	134.4004	10.0078	39.1180	0.1655
173	353.3446	-1.1486	39.1332	0.1014
174	229.0613	-0.8197	39.2400	0.1039
175	319.4521	7.5415	39.8350	0.1358
176	228.2191	-1.4742	40.3994	0.1304
177	131.2534	27.7891	40.4757	0.1008
178	247.3975	28.1821	40.9028	0.1452
179	151.6617	25.9125	41.4520	0.1157
180	332.6655	15.8109	41.5130	0.1763
181	0.9570	2.0665	41.6503	0.1036
182	213.1324	14.0114	41.9249	0.1407
183	214.2572	13.9110	42.0774	0.1627
184	222.7892	14.6120	42.1995	0.1510
185	41.7612	4.3889	42.2452	0.1390
186	153.7062	10.6564	42.4741	0.1989
187	31.5952	-1.3088	42.4893	0.1898
188	123.6741	6.9073	42.5198	0.1136
189	17.4552	5.2828	42.5503	0.1326
190	228.1447	16.4772	42.9927	0.1987
191	29.3368	-5.8564	43.2978	0.1364
192	250.8302	21.5226	43.3436	0.1624
193	38.9280	-5.4157	43.3741	0.1776
194	143.0949	8.1975	43.7555	0.1914
195	149.4972	3.4572	44.3352	0.1638
196	320.0268	1.4425	44.5487	0.1339
197	198.5821	-1.4572	44.6403	0.1740
198	175.1895	18.3440	45.0216	0.1830

Table .6. – Summary of the CODEX cluster samples. (cont.)

ID	RA_{OPT}	DEC_{OPT}	λ_{OPT}	$z_{cluster}$
199	345.1467	1.7530	45.4335	0.1868
200	244.6042	9.1791	46.1505	0.1483
201	166.8652	7.9944	46.2115	0.1627
202	16.7221	-2.4824	46.5166	0.1865
203	24.1481	-8.1018	46.9590	0.1450
204	34.2005	-2.1019	47.0200	0.1324
205	258.1489	24.8406	47.0506	0.1711
206	327.8934	10.7527	47.1116	0.1969
207	12.5253	-6.4395	47.2794	0.1995
208	150.2578	28.1670	47.8438	0.1964
209	115.9130	14.7267	48.6066	0.1419
210	139.1036	5.8873	48.6676	0.1289
211	155.5224	9.1571	48.6676	0.1856
212	139.4893	9.8532	48.7133	0.1872
213	162.6522	-2.6045	48.7591	0.1624
214	10.1525	18.1548	48.8201	0.1620
215	243.7126	8.9480	49.0032	0.1475
216	149.7457	-0.2061	49.0642	0.1674
217	243.6296	26.7306	49.1557	0.1845
218	5.7801	-0.0635	49.8422	0.1624
219	32.5313	2.9074	49.9185	0.1499
220	30.5095	3.7477	50.5439	0.1567
221	8.5968	0.8572	51.8101	0.1890
222	29.2846	-5.8729	52.2220	0.1310
223	117.8546	17.5142	52.2830	0.1915
224	134.8847	3.1447	52.2830	0.1862
225	132.0707	28.7058	52.3135	0.1987
226	24.8175	-3.6344	52.6034	0.1055
227	174.2320	26.5678	52.8017	0.1638
228	235.3604	4.7320	52.9085	0.1171
229	220.1561	13.0502	53.3051	0.1884
230	137.9769	10.9636	53.3356	0.1660
231	180.4320	-0.1845	53.6407	0.1622
232	351.2583	17.9082	53.6865	0.1543
233	250.6610	27.4437	53.7170	0.1091
234	229.2244	-1.0851	53.7933	0.1155
235	29.6080	-1.7776	53.9458	0.1563
236	41.4655	-0.7046	54.6323	0.1799
237	138.0467	13.6442	54.7848	0.1819
238	354.1564	-1.4645	55.5018	0.1846
239	153.4434	19.7638	55.7459	0.1098
240	144.3494	12.8868	56.2035	0.1744

Table .7. – Summary of the CODEX cluster samples. (cont.)

ID	RA_{OPT}	DEC_{OPT}	λ_{OPT}	$z_{cluster}$
241	253.3081	29.1650	56.4324	0.1451
242	33.6712	-4.5674	56.8137	0.1446
243	219.4327	-0.3160	57.5917	0.1346
244	149.3922	19.6371	57.7443	0.1717
245	115.8463	17.5616	57.8053	0.1013
246	16.3981	2.5162	58.3545	0.1968
247	222.6597	5.2958	58.6443	0.1547
248	136.3173	10.3307	59.4529	0.1835
249	167.7967	0.7522	59.7885	0.1888
250	140.5670	12.4317	60.4139	0.1926
251	20.5110	0.3345	61.0089	0.1801
252	210.6682	17.7563	62.6564	0.1820
253	213.7850	-0.4932	63.3734	0.1370
254	145.1024	2.4776	63.8768	0.1556
255	243.5414	26.6488	63.8768	0.1842
256	140.9428	8.6830	64.9599	0.1342
257	243.5041	26.6930	65.2040	0.1875
258	228.2248	14.3040	65.4938	0.1789
259	172.4435	23.8243	66.7142	0.1337
260	154.1519	24.8009	67.8278	0.1804
261	211.9437	14.0033	68.1939	0.1342
262	145.2923	12.5705	68.4533	0.1788
263	260.0402	27.6689	68.7736	0.1604
264	229.3411	-0.7156	68.8347	0.1138
265	260.0418	26.6256	69.9025	0.1653
266	132.6157	0.2504	69.9940	0.1977
267	136.6070	10.3637	70.5737	0.1403
268	187.2263	19.4318	74.6773	0.1626
269	320.2817	5.3289	76.2486	0.1464
270	42.0141	-3.5292	76.4469	0.1882
271	336.5330	17.3565	77.5758	0.1130
272	229.0747	0.0891	77.7741	0.1206
273	228.8088	4.3862	77.9724	0.1017
274	233.2648	-0.7713	79.7420	0.1520
275	125.8303	15.9627	81.8166	0.1562
276	37.9215	-4.8826	86.6525	0.1884
277	134.4751	3.1764	91.5035	0.1979
278	172.4773	20.4195	94.4020	0.1346
279	141.0642	14.1284	101.9532	0.1375

Résumé

A. Galaxy Cluster

Les amas de galaxies, les dernières structures formées dans l'univers, sont des objets très intéressants pour les études cosmologiques. Premièrement, ils ont une fonction de masse bien définie, dont la forme reflète la valeur des paramètres cosmologiques. Deuxièmement, les simulations numériques prédisent des profils de densité caractéristiques, la fonction de masse des sous-halo et leur triaxialité, quantités qui dépendent des propriétés des particules de matière noire, bien que les effets astrophysiques tendent à les masquer. Enfin, la fraction de gaz dans les amas reflète le contenu cosmologique.

La composition des amas de galaxies peut être séparée en trois composantes principales: Galaxies, milieu intra-amas (ICM) et matière noire. Les galaxies ne constituent qu'une petite fraction de la masse totale, avec moins de 5 à 10% de la masse totale. L'ICM est un plasma chaud avec une température de 10^7 – 10^8 Kelvins qui émet en rayons X, représentant environ 10-15% de la masse totale. Par conséquent, le budget de masse d'un amas de galaxies est fortement dominé par la matière noire (plus de 80 %), une composante insaisissable qui est parfois appelée "masse manquante" car nous ne la détectons pas directement mais indirectement, à travers ses effets gravitationnels.

Les amas de galaxies peuvent être observés du domaine radio aux rayons X, ce qui nous renseigne sur la distribution spatiale de leurs différentes composantes. Dans la figure 1.2, je montre la comparaison entre les images optiques et en rayons X de l'amas de galaxies Abell 2029. L'observation optique montre la lumière des galaxies tandis que l'observation aux rayons X révèle le gaz chaud de l'ICM.

B. Lentille gravitationnelle

L'optique gravitationnelle est le phénomène qui se produit lorsque la lumière provenant de sources d'arrière plan est déviée par des objets massifs situés le long de la ligne de visée. En effet, les objets massifs déforment localement l'espace-temps; par conséquent la lumière passant dans leur proximité se trouve déviée. La figure 2.2 illustre ce phénomène. Il existe deux principaux régimes de lentille gravitationnelle. Dans le régime de lentille forte, non linéaire, lorsque la lumière traverse le coeur de l'amas où la densité de masse est très élevée (supérieure à la

densité critique), on peut observer plusieurs images de la même source d'arrière plan, ainsi que des arcs géants. Lorsque la lumière passe dans la périphérie de l'amas, où la densité est moindre, on peut être sensible, statistiquement, à de faibles distorsions dans la forme des galaxies d'arrière plan. Il s'agit du régime de lentille faible, linéaire. Dans les deux cas, ces observations fournissent des informations sur la distribution de masse du déflecteur qui a donné naissance à ces "mirages gravitationnels".

B.1 Effet de lentille gravitationnelle faible dans les amas de galaxies

La force de l'effet dépend de la distribution de masse de la lentille, des distances impliquées dans le problème et de l'alignement entre l'amas et la source. Dans l'analyse de lentille gravitationnelle faible, nous approximons la forme d'une galaxie comme une ellipse. Cette ellipticité peut être exprimée comme

$$\gamma = \gamma_1 + i\gamma_2 = \frac{a-b}{a+b} e^{2i\phi} \tag{.9}$$

où ϕ est l'angle de position, a et b sont respectivement les axes semi-majeur et mineur. En pratique, il convient de définir le cisaillement réduit (g):

$$g(\vec{\theta}) \equiv \frac{\gamma(\vec{\theta})}{1-\kappa(\vec{\theta})} \,. \tag{.10}$$

L'ellipticité de l'image déformée (ϵ_I) est liée à l'ellipticité de la source (ϵ_S) par

$$\epsilon_I = \begin{cases} \frac{\epsilon_S + g}{1+g^*\epsilon_S} & \text{if } |g| \geq 1 \,, \\ \frac{1+g\epsilon_S^*}{\epsilon_S^*+g^*} & \text{if } |g| < 1 \,. \end{cases} \tag{.11}$$

Dans le régime de lentille faible, $\kappa \ll 1$ et $|g| \ll 1$, de sorte que la relation entre les ellipticités est donnée par

$$\epsilon_I \approx \epsilon_S + g \approx \epsilon_S + \gamma \,. \tag{.12}$$

En supposant que les galaxies d'arrière plan sont distribuées de manière aléatoire, et en faisant la moyenne de la relation ci-dessus sur un échantillon de galaxies, nous avons ($\epsilon_S \approx 0$). Par conséquent, les ellipticités des images lentillées deviennent

$$\epsilon_I \approx \gamma \,. \tag{.13}$$

Le signal de cisaillement ou de lentille faible est donc directement lié à l'ellipticité moyenne des images.

B.2 Profil de Masse

Dans ce travail, j'utilise le profil Navarro-Frenk-White (ci-après profil NFW) qui est largement utilisé pour décrire les distributions de masse des amas de galaxies. La distribution de masse totale sera décrite comme suit:

$$\Delta\Sigma(R) = \Sigma_{\rm 1h}^{\rm NFW}(R) + \Delta\Sigma_{\rm 2h}(R) \tag{.14}$$

où $\Delta\Sigma_{\rm 1h}^{\rm NFW}$ est la densité de masse surfacique excédentaire du profil NFW, et $\Delta\Sigma_{\rm 2h}$ est la composante du deuxième terme de halo.

B.2.1 Profil Navarro-Frenk-White

La simulation numérique est un outil important pour sonder la formation et l'évolution des structures à grande échelle. Navarro, Frenk, and White 1997 ont utilisé des simulations à N-corps dans le cadre théorique de la matière noire froide pour étudier le profil de densité des halos. Ils ont constaté que les halos sont bien décrits par un profil de masse "universel" sur plusieurs ordres de grandeur, en particulier à l'échelle des amas de galaxies. Le profil de densité de masse 3D est donné par:

$$\rho(r) = \frac{\delta_c \rho_c}{(r/r_s)(1 + r/r_s)^2}\,, \tag{.15}$$

où r est la distance tri-dimensionelle au centre de l'amas, r_s est le rayon de l'échelle, et δ_c est le seuil de surdensité linéaire auquel un halo s'effondre et est défini comme

$$\delta_c = \frac{200}{3}\frac{c^3}{[\ln(1+c) - c/(1+c)]}\,. \tag{.16}$$

Nous définissons généralement un paramètre sans dimension appelé paramètre de concentration, $c \equiv r_{200}/r_s$, où r_{200} est le rayon à l'intérieur duquel la densité de masse du halo est égale à 200 fois la densité critique de l'Univers, qui peut s'écrire

$$\rho_c = \frac{3}{800\pi}\frac{M_{200}}{r_{200}^3}, \tag{.17}$$

où M_{200} est la masse de l'amas calculée dans ce rayon. De plus, le cisaillement tangentiel subi par les sources d'arrière-plan à redshift z_s par le cluster à redshift z_l est donné par

$$\gamma_t(R) \equiv \frac{\overline{\Sigma}(< R) - \Sigma(R)}{\Sigma_{\rm cr}(z_l, z_s)} = \frac{\Delta\Sigma(R)}{\Sigma_{\rm cr}}\,, \tag{.18}$$

où $\overline{\Sigma}(< R)$ est la densité de surface moyenne à l'intérieur de ce rayon, et $\Sigma(R)$ est la densité de surface moyenne au rayon R.

B.2.2 Le terme du 2e halo

Les amas de galaxies constituent les nœuds de la toile cosmique, et sont nourris de matière venant le long des filaments reliant les amas de galaxies. Par conséquent, lors de l'étude d'un profil de masse d'amas de galaxies jusqu'à grande distance du centre (typiquement supérieure à 5 Mpc), on commence à être sensible aux amas voisins. Cela s'explique par le terme de 2e halo, dont la densité de masse surfacique excédentaire est donnée par:

$$\Delta\Sigma_{\rm 2h}(R) = \overline{\Sigma}_{\rm 2h}(< R) - \Sigma_{\rm 2h}(R)\,. \tag{.19}$$

L'excès de masse surfacique au rayon projeté (R) est défini par

$$\Sigma_{\rm 2h}(R) = 2\rho_{c,0}\Omega_{m,0}\int_0^\infty \xi_{\rm 2h}\left(\sqrt{R^2+\chi^2}\right)\mathrm{d}\chi\,, \tag{.20}$$

où $\xi_{\rm 2h}(r)$ est la fonction de corrélation croisée galaxie-matière, $\rho_{c,0}$ est la densité critique, et $\Omega_{m,0}$ est la densité de matière de l'univers à l'heure actuelle. Cette fonction est obtenue en multipliant la fonction de corrélation de matière non linéaire $\xi_{nl}(r)$ avec le biais de halo $b(M)$ donné par

$$\xi_{\rm 2h}(r) = b(M)\,\xi_{nl}(r)\,\zeta(r) \tag{.21}$$

où $\zeta(r)$ est la dépendance d'échelle du biais de halo.

B.2.3 La relation masse-concentration

Le profil NFW est décrit par deux paramètres; la concentration (c) et la masse totale (M200). Les résultats des simulations numériques montrent que la concentration et la masse totale (c-M) sont liées. La relation (c-M) a également été testée observationnellement (par exemple, N. Okabe, M. Takada, K. Umetsu, et al. 2010). La relation entre la concentration et la masse totale est un outil important pour tester le modèle cosmologique et les processus physiques dans les amas de galaxies. Dans mon analyse, puisque le rapport signal / bruit de la mesure est faible, j'ai utilisé la relation (c-M) de Dutton and Macciò 2014 pour réduire le nombre de paramètres libres dans notre modèle. Cette relation (c-M) est dérivée d'un ensemble complet d'amas de galaxies simulés qui peuvent différer de notre échantillon, surtout à faible masse où nous sommes susceptibles d'être incomplets. Néanmoins, l'étude précédente de Cibirka, Cypriano, Brimioulle, et al. 2017 sur les amas CODEX montre un excellent accord avec la simulation de Dutton and Macciò 2014.

C. Préparation des données

C.1 DECaLS Data Release 3

Dans ce travail, j'utilise la troisième version des données DECaLS (Dark Energy Camera Legacy Survey) pour l'analyse en lentilles faibles. Ce relevé fait partie du Legacy Imaging Survey de l'instrument DESI (Dark Energy Spectroscopic Instrument; Dey, D. J. Schlegel, D. Lang, et al. 2019). Il fournit l'imagerie optique pour le ciblage spectroscopique des 2/3 de l'empreinte DESI. DECaLS utilise la caméra pour l'énergie sombre (DECam) installée sur le télescope Blanco de 4 mètres, situé à l'observatoire interaméricain Cerro Tololo au Chili. Les données d'imagerie DECaLS DR3 couvrent 4300 deg^2 en bande g, 4600 deg^2 en bande r et 8100 deg^2 en bande z. Au total, 4200 deg^2 ont été observés dans les trois bandes optiques. La figure 3.2 montre la profondeur des objets DECaLS DR3 observés dans trois bandes optiques; g, r et z. Dans le catalogue DECaLS DR3, les objets du catalogue Tractor sont classés en cinq modèles morphologiques: Source ponctuelle (PSF), galaxie simple (SIMP), DeVaucouleurs (DEV), exponentiel (EXP) et modèle composite (COMP).

C.2 Catalogue de cisaillement DECaLS

Pour calibrer le catalogue de cisaillement DECaLS DR3, je fais une correspondance croisée entre les objets DECaLS et les objets du relevé Stripe 82 du télescope Canada France Hawaii (CFHT) et je calcule les paramètres de correction. Le CFHT Stripe 82 (CS82) est un relevé couvrant $\approx$ 170 degrés carrés du Sloan Digital Sky Survey (SDSS) Stripe 82 dans la région équatoriale du Cap Galactique Sud. Les données d'imagerie sont de haute qualité. Elles ont été prise dans d'excellentes conditions, avec un seeing compris entre 0,4 et 0,8 arcsec, avec une moyenne de 0,59 arcsec. La magnitude limite est $i_{AB} \approx 24$. Ce relevé a été entrepris pour l'analyse de lentilles (voir par exemple Shan, Jean-Paul Kneib, Comparat, et al. 2014; Liu, Pan, Li, et al. 2015)

C.3 Distribution en Redshift

Dans ce travail, j'estime la distance aux objets DECaLS en utilisant la distribution en redshift du catalogue de cisaillement DECaLS DR3, en suivant la procédure ci-dessous. Je considère d'abord la relation suivante entre le cisaillement tangentiel et la densité de masse surfacique excédentaire

$$\Delta\Sigma(R) = \gamma_t(R) \left\langle \Sigma_{\rm cr}^{-1}(z_l) \right\rangle^{-1} . \tag{.22}$$

En pratique, je peux calculer une densité surfacique critique efficace (T.McClintock, Varga, Gruen, et al., 2019; Nobuhiro Okabe, Futamase, Kajisawa, et al., 2014) en

intégrant sur la distribution source,

$$\left\langle \Sigma_{\rm cr}^{-1}(z_l) \right\rangle = \frac{\int P(z_{\rm s})\, \Sigma_{\rm cr}^{-1}(z_l, z_s)\, {\rm d}z_s}{\int P(z_{\rm s})\, {\rm d}z_s}\,, \tag{.23}$$

où $P(z_{\rm s})$ est la fonction de distribution de probabilité des galaxies sources. J'estime la fonction de distribution de probabilité du catalogue de cisaillement DECaLS en supposant que les sources du catalogue de cisaillement DECaLS sont bien adaptées à la fonction de distribution de probabilité en redshift donnée par

$$P(z_s) \propto A \left(\frac{z_s}{z_0}\right)^{B-1} \exp\left[-\frac{1}{2}\left(\frac{z_s}{z_0}\right)^2\right]\,, \tag{.24}$$

où A, B et z_0 sont des paramètres libres. Je fais correspondre le catalogue de cisaillement DECaLS DR3 avec le catalogue COSMOS 2015 en adoptant une seconde d'arc comme étant la séparation maximale des deux catalogues. Ensuite, je calcule la distribution de probabilité de redshift à partir du redshift photométrique des objets COSMOS 2015 appariés. J'ajuste la distribution de probabilité en redshift photométrique avec l'équation 3.7 et j'obtiens les meilleures valeurs d'ajustement suivantes: $A = 2,261 \pm 0,172$, $B = 1,801 \pm 0,173$ et $z_0 = 0,432 \pm 0.035$ comme le montre la figure 3.5. Je peux donc calculer la densité critique effective au lieu de calculer le redshift photométrique pour toutes les sources.

C.4 Catalogue d'amas CODEX

Le phénomène de lentille gravitationnelle est lié à la courbure de l'espace-temps induite par les objets d'avant plan massif, comme les galaxies ou les amas de galaxies. Dans ce travail, j'utilise le catalogue d'amas de galaxies CODEX (COnstrain Dark Energy with X-ray) comme échantillon d'objets d'avant plan. Le catalogue d'amas CODEX a été construit en identifiant les sources de rayons X dans les données ROSAT All-Sky Survey (Voges, Aschenbach, Boller, et al. 1999) à l'aide de l'algorithme redMaPPer (RRykoff, Rozo, Busha, et al. 2014). Le catalogue d'amas CODEX contient le redshift de l'amas, sa richesse ($\lambda_{\rm SDSS}$) et la position du centre optique déterminée par l'algorithme redMaPPer. La richesse est évaluée à deux positions, celle du pic en rayons X et la position optique. L'ensemble des paramètres redMaPPer identifiés au centre optique sont annotés avec le suffixe OPT ($z_{\lambda,{\rm OPT}}$, $\lambda_{\rm OPT}$, etc.). Un relevé d'IDentification SPectroscopique SDSS-IV dédié des sources eRosita (SPIDERS; Dawson, J.-P. Kneib, Percival, et al. 2016; Blanton, Bershady, Abolfathi, et al. 2017) a été réalisé au cours de la période 2014-2018 pour obtenir le décalage vers le rouge (redshift) des galaxies membres des amas CODEX. Ces observations ont permis de confirmer une fraction élevée d'amas à $z < 0,4$ (Clerc, Merloni, Zhang, et al. 2016). De plus, dans DES, Klein, Grandis, J. Mohr, et al. 2018 a constaté que l'échantillon d'amas redMaPPer compris dans la plage de redshift considérée dans ce travail ($0,1 < z < 0,2$), et avec la

richesse $\lambda > 20$ est propre à 99%. La figure 3.8 montre la comparaison entre les estimations de la richesse des amas CODEX situés dans l'empreinte DECaLS DR3, selon que l'on considère le centre en rayons X ou le centre optique.

C.5 Stacking d'amas de galaxies

L'analyse en lentille faible des amas de galaxies nécessite des données d'imagerie profondes et de haute qualité. Les données DECaLS DR3 ne sont pas suffisantes pour mesurer le signal de lentille faible (signal de cisaillement) sur les amas individuels, en raison de la faible densité numérique des sources; de la profondeur limitée des données d'imagerie et de l'algorithme de mesure de forme des galaxies d'arrière plan. En effet, comme discuté ci-dessus, je ne suis capable de calibrer que la forme des sources de type EXP, DEV et COMP, en laissant de côté une grande partie (> 50 %) des sources. J'applique donc la technique de "stacking" (empilement) pour améliorer le signal en lentille faible. C'est une méthode dans laquelle je regroupe les amas de galaxies en fonction d'une propriété observée (par exemple, la richesse optique ou la luminosité en rayons X), et mesure le signal de lentille moyen produit par ce groupe d'amas. La densité de masse surfacique superposée empilée peut être écrite comme une somme du cisaillement tangentiel sur les galaxies de fond N, qui se trouvent dans une région annulaire centrée au rayon R pour chaque amas. L'expression correspondante est

$$\Delta\Sigma(R) = C(R)\frac{\sum_{\mathrm{i}=1}^{N} w_{\mathrm{i}}\gamma_{\mathrm{t,i}}(R)\,\langle\Sigma_{\mathrm{cr}}^{-1}\rangle^{-1}}{\sum_{\mathrm{i}=1}^{N}(1+m)w_{\mathrm{i}}}, \tag{.25}$$

où $C(R)$ est un facteur de correction décrit ci-dessous, et w est un poids qui découle de l'erreur de mesure de la forme et minimise la variance de l'estimateur de cisaillement.

D. Résultats

D.1 Amas CODEX

Dans cette première approche, je sépare les amas CODEX en trois groupes de richesse et je stacke leur profil de densité de masse surfacique excédentaire ($\Delta\Sigma$); λ = 20 - 30, 30 - 50 et 50 - 110. Je mesure d'abord le profil de cisaillement tangentiel de chaque amas CODEX dans la plage radiale $1.0 \leq R < 30$ Mpc (12 bins). À partir de la procédure d'ajustement, j'utilise une méthode MCMC avec un prior plat pour la masse de l'amas M_{200c} = [13,0, 15,0]. J'obtiens la masse moyenne des amas pour chaque groupe. Néanmoins, je trouve de fortes fluctuations à grand rayon (par exemple, $R > 5$ Mpc). Pour vérifier la cohérence, je recalcule les masses des amas en mesurant le profil de staking dans la région

intérieure $1,0 \leq R < 5,5$ Mpc, et je n'ajuste qu'avec le premier terme de halo, c'est-à-dire le profil NFW. Les résultats de l'ajustement sont présentés dans le tableau 5.1 et la figure 5.1. Je note que les différences sur les masses d'amas entre les deux régions (intérieure et tout rayon) atteignent jusqu'à environ 15 - 25 %. Je suppose que cela est dû aux fortes incertitudes à grand rayon; Cependant, les résultats restent en accord avec le niveau de confiance à 2σ.

D.2 Relation d'échelle

Pour déterminer la relation d'échelle, je suppose que la relation de richesse en masse des amas CODEX est bien définie par une relation de loi de puissance donnée par

$$\langle M_{200c}|\lambda\rangle = M_0 \left(\frac{\lambda}{\lambda_0}\right)^{F_\lambda}, \tag{.26}$$

où M_0 est la masse moyenne de l'amas à la richesse $\lambda = 40$, et F_λ est l'indice de mise à l'échelle de la richesse. J'utilise la même méthode MCMC que ci-dessus et définit les priors suivants sur les paramètres de la relation d'échelle: $\log_{10}M_0$ = [13,0, 15,0] et F_λ = [-10,0 , 10,0]. J'ai également défini les paramètres initiaux suivants: $\log_{10}M_0$ = 14,0 et F_λ = 0,1. Dans la figure 5.2, je présente les fonctions de distribution postérieure des paramètres de la relation masse-richesse.

À partir de ces fonctions, je peux estimer la masse moyenne des amas de l'échantillon CODEX

$$M_0 = 3,24^{+0,29}_{-0,27} \times 10^{14}\,\mathrm{M}_\odot\,, \tag{.27}$$

et l'indice de mise à l'échelle de la richesse,

$$F_\lambda = 1,00^{+0,22}_{-0,22}\,. \tag{.28}$$

Enfin, j'ai comparé mon analyse de lentille faible avec l'analyse dynamique obtenue par Capasso, J. J. Mohr, Saro, et al. 2019. La comparaison entre les deux analyses montre qu'elles sont en parfait accord, ce qui pourrait suggérer que l'hypothèse d'équilibre dynamique convient en moyenne.